



Norwegian University of  
Science and Technology

# Concentrated Solar Power Gas Turbine Hybrid with Thermal Storage

**Bård Sve Wallentinsen**

Master of Science in Mechanical Engineering

Submission date: August 2016

Supervisor: Lars Olof Nord, EPT

Norwegian University of Science and Technology  
Department of Energy and Process Engineering



EPT-M-2016-160

**MASTER THESIS**

for

student Bård Sve Wallentinsen

Spring 2016

**Concentrated solar power gas turbine hybrid with thermal storage****Background and objective**

Solar radiation can be concentrated with a large number of mirrors reflecting the radiation towards a large solar tower where a fluid can be heated up. This fluid can subsequently be used in a power plant. One idea is to use it in a gas turbine plant as a hybrid solution. To achieve a high efficiency of the gas turbine, the solar energy may not be enough but the GT can be co-fired with natural gas to get a higher turbine inlet temperature and to easier follow the electrical demand.

The overall objective of the Master's thesis is to make detailed process models of a solar gas turbine hybrid system and subsequently simulate the processes and generate results both at the design point and at off-design conditions including quasi-dynamic scenarios (time series). The overall performance of the plant should be evaluated as well as the CO<sub>2</sub> emitted. The software to be used is Ebsilon Professional.

**The following tasks are to be considered:**

1. Literature study on solar gas turbine hybrid systems including thermal storage and bottoming cycles such as steam cycles and Organic Rankine Cycles (ORC).
2. Evaluation and decision of cycle configuration(s) to be studied.
3. Build-up of steady-state process models of the selected cycle(s) including reference cases based on a solar-only system and a natural gas only system.
4. Design point process simulation of the cycle(s) including model validation.
5. Quasi-dynamic simulations for different operating scenarios.
6. Sensitivity analysis to investigate which input parameters effect the results the most.

Within 14 days of receiving the written text on the master thesis, the candidate shall submit a research plan for his project to the department.

When the thesis is evaluated, emphasis is put on processing of the results, and that they are presented in tabular and/or graphic form in a clear manner, and that they are analyzed carefully.

The thesis should be formulated as a research report in English with summary, conclusion, literature references, table of contents etc. During the preparation of the text, the candidate should make an effort to produce a well-structured and easily readable report. In order to ease the evaluation of the thesis, it is important that the cross-references are correct. In the making of the report, strong emphasis should be placed on both a thorough discussion of the results and an orderly presentation.

The candidate is requested to initiate and keep close contact with his/her academic supervisor(s) throughout the working period. The candidate must follow the rules and regulations of NTNU as well as passive directions given by the Department of Energy and Process Engineering.


Risk assessment of the candidate's work shall be carried out according to the department's procedures. The risk assessment must be documented and included as part of the final report. Events related to the candidate's work adversely affecting the health, safety or security, must be documented and included as part of the final report. If the documentation on risk assessment represents a large number of pages, the full version is to be submitted electronically to the supervisor and an excerpt is included in the report.

Pursuant to "Regulations concerning the supplementary provisions to the technology study program/Master of Science" at NTNU §20, the Department reserves the permission to utilize all the results and data for teaching and research purposes as well as in future publications.

The final report is to be submitted digitally in DAIM. Based on an agreement with the supervisor, the final report and other material and documents may be given to the supervisor in digital format.

- Work to be done in lab (Water power lab, Fluids engineering lab, Thermal engineering lab)  
 Field work

Department of Energy and Process Engineering, 13. January 2016



Olav Bolland  
Department Head



Lars Nord  
Academic Supervisor

## Abstract

Concentrated Solar Power (CSP) technology and shows promise for large-scale renewable electric power generation. CSP is suitable for development in conjunction with other technologies, and this thesis examines the combination of CSP technology with natural gas turbines in order to boost operating temperatures and efficiencies in a resulting solar hybrid gas turbine (SHGT) power plant. Thermal energy storage and a bottoming cycle are included in the design to increase both performance and renewable energy share. A literature study has been carried out on solar hybrid gas turbine technology, including thermal energy storage and bottoming cycles. A site with suitable solar resources in Europe was located, and design criteria for a candidate utility-scale power plant were selected. A SHGT power plant was designed and modelled in the process simulation software EBSILON® Professional, along with reference power plants for comparison. Quasi-steady state process simulation of the process models was carried out to find annual performance for different operating scenarios. While the candidate SHGT power plant was found to have limited potential as a base load power plant, an operation strategy to maximize solar share resulted in significant fuel savings and moderate emission cuts. The SHGT plant shows promise for further study for dispatchable power generation and load shifting.



## Sammendrag

Konsentrert termisk solkraft (CSP) er en lovende teknologi for fornybar elektrisk kraftproduksjon i stor skala. CSP er godt egnet for integrering med andre teknologier, og denne oppgaven tar for seg kombinasjon av CSP-teknologi med gassturbiner fyrt med naturgass. Hensikten med en slik kombinasjon er å øke trykk og temperatur i kraftsyklusen i det resulterende hybride sol-gasskraftverket. Termisk lagring av energi og en bunnsyklus er inkludert i designet av et slikt kraftverk for å øke både ytelsen og den fornybare andelen av generert elektrisk kraft. En litteraturstudie har blitt gjennomført om termiske solkraftverk og hybride sol-gasskraftverk, inklusive om termisk energilagring og bunnsykluser. En potensiell beliggenhet i Europa med passende solare ressurser for hybridkraftverket har blitt stadfestet, og designkriteria for et fullskala kraftverk etablert. Et hybridkraftverk har blitt designet og modellert i prosessimuleringsprogrammet EBSILON® Professional, sammen med referansemodeller for sammenligning. Simuleringer ved stabile tilstander og kvasi-stabile prosessimuleringer har blitt utført på modellene for å finne årlig ytelse under forskjellige operasjonelle situasjoner. Mens det valgte hybridkraftverket viste seg å ha begrenset potensial som grunnbelastningskraftverk, ble det for det samme kraftverket med en strategi som maksimerer solfraksjonen i kraftgenerasjonen påvist mulighet for betydelig reduksjon i bruk av brensel, og moderate reduksjoner i utslipp. Hybridkraftverket modellert er i oppgaven vist interessant for videre utredning for fleksibel kraftproduksjon.





## Acknowledgements

I would like to thank my supervisor Lars Olof Nord, for his advice and guidance in the course of both this thesis and previous project work.

I am also deeply grateful to Myselie Nguyen for all her support and kindness these past years.



# Contents

<b>List of Figures</b>	<b>x</b>
<b>List of Tables</b>	<b>xiv</b>
<b>1 Introduction</b>	<b>1</b>
1.1 Background . . . . .	1
1.2 Structure of this thesis . . . . .	1
1.3 Risk Assessment . . . . .	2
<b>2 Concentrated Solar Power - CSP</b>	<b>3</b>
2.1 Focusing Sunlight . . . . .	4
2.2 CSP Technologies . . . . .	5
2.2.1 Parabolic Trough Technology . . . . .	7
2.2.2 Sentral Receiver Systems . . . . .	10
2.2.3 Fresnel and Parabolic Dish Technologies . . . . .	15
2.3 Solar Concentration . . . . .	17
<b>3 The Solar Hybrid Gas Turbine</b>	<b>21</b>
3.1 The Brayton Cycle . . . . .	22
3.2 Conventional Gas Turbine Components . . . . .	23
3.2.1 Compressors . . . . .	23
3.2.2 Combustion chambers . . . . .	24
3.2.3 Turbines . . . . .	25
3.3 Solar Thermal Hybridization . . . . .	29
3.3.1 Component integration . . . . .	30
3.3.2 Performance indicators . . . . .	35
3.3.3 Operational strategy . . . . .	37
<b>4 Thermal Energy Storage</b>	<b>41</b>
4.1 Sensible Heat Storage . . . . .	44
4.1.1 Liquid sensible storage media . . . . .	45
4.1.2 Solid sensible storage media . . . . .	46
4.2 Latent Heat Storage . . . . .	48

4.3	Thermochemical Energy Storage . . . . .	51
<b>5</b>	<b>Bottoming Cycles</b>	<b>55</b>
5.1	The Steam Rankine Cycle . . . . .	56
5.2	The Organic Rankine Cycle . . . . .	58
5.3	Air-Cooled Dual-Pressure Rankine Cycle . . . . .	60
5.4	Air-Based Bottoming Cycle . . . . .	62
<b>6</b>	<b>Simulation Background and Assumptions</b>	<b>65</b>
6.1	Localization . . . . .	66
6.2	Ambient Conditions . . . . .	69
6.3	Power Plant Design Decisions . . . . .	70
6.4	General and Component Assumptions . . . . .	71
6.4.1	Conventional Gas Turbine Components . . . . .	71
6.4.2	Heliostat Field . . . . .	73
6.4.3	Solar Tower and Receiver . . . . .	73
6.4.4	Thermal Energy Storage . . . . .	74
6.4.5	Bottoming Cycle . . . . .	76
<b>7</b>	<b>Process Simulations</b>	<b>79</b>
7.1	The Air-Bottoming Solar Hybrid Gas Turbine Power Plant . . . . .	79
7.2	Reference Cycles . . . . .	85
7.2.1	Natural Gas Power Plant . . . . .	85
7.2.2	Solar Only Power Plant . . . . .	85
7.3	Steady State Design Point Results . . . . .	90
7.4	Annual Performance Results . . . . .	95
7.5	Sensitivity Analysis . . . . .	97
7.6	Validation . . . . .	98
<b>8</b>	<b>Conclusions and Further Work</b>	<b>101</b>
8.1	Conclusions . . . . .	101
8.2	Further Work . . . . .	102
	<b>References</b>	<b>105</b>
	<b>Appendices</b>	
<b>A</b>	<b>Process Simulation Control EbsScript</b>	<b>113</b>
<b>B</b>	<b>Kernel Scripted Heat Exchange Component</b>	<b>117</b>
<b>C</b>	<b>Basic Thermodynamic Background</b>	<b>119</b>
C.1	The First Law of Thermodynamics . . . . .	119
C.2	The Second Law of Thermodynamics . . . . .	120

C.3 Reversibility and Entropy . . . . .	120
<b>D Annual Irradiance Values</b>	<b>123</b>

# List of Figures

2.1	Recent development in world total CSP capacity, adapted from [10]	4
2.2	The attenuation of solar radiation as it passes through the atmosphere[22].	6
2.3	The air mass ratio at different solar angles[17].	7
2.4	A map of world annual average DNI, Courtesy of SolarGIS[23], DNI Solar Map © 2016 GeoModel Solar	8
2.5	Flow chart for a general CSP power plant including thermal storage and (fossil) fuel for backup and co-firing[17]	9
2.6	The operation strategy of a CSP plant with both thermal energy storage and (fossil) fuel as an energy back-up, as a base load plant[25].	9
2.7	Principles of the four main CSP technology types: (a) parabolic troughs; (b) linear fresnel collectors; (c) central receiver system / power tower and (d) parabolic dish[26].	10
2.8	A schematic of a parabolic trough system[20].	11
2.9	A cut-away of the trough configuration as seen from its side[29].	11
2.10	Front view of heliostats[30].	11
2.11	Rear view of a heliostat[31].	11
2.12	A presentation of the heat transfer principle in a volumetric receiver[14].	12
2.13	Diferent receiver types; from top left and clockwise: external tubular cylindrical; cavity tubular; billboard tubular and volumetric atmospheric[24].	13
2.14	The reduction in effective surface area due to receiver angle[17].	14
2.15	An illustration of the total efficiencies of a heliostat field[24].	14
2.16	Two different heliostat fields located close to the equator (top) and at higher latitudes[24].	15
2.17	A dish sterling CSP system[34].	16
2.18	A linear fresnel CSP system[35].	16
2.19	An illustration of the maximum possible theoretical receiver efficiency for different concentration ratios[17].	18
2.20	Different optimal receiver efficiencies plotted against the carnot efficiency[24].	18
2.21	The combined optimal system efficiency of a receiver and the carnot cycle[24].	19

2.22	An illustration of the incremental increase in power available by increasing the solar multiple[17]. . . . .	20
3.1	An illustration of the components of a gas turbine by Siemens[39]. . . .	21
3.2	A block diagram of a gas turbine connected to a generator for power generation[42]. . . . .	22
3.3	A temperature-entropy diagram of the Bratyon cycle including pressure losses[39]. . . . .	22
3.4	Performance characteristics of an axial compressor[45]. . . . .	25
3.5	An example of a compressor map for a axial compressor[39]. . . . .	26
3.6	A gas turbine with side-mounted silo-type combustors[39]. . . . .	27
3.7	Emissions from a gas turbine depending on the fuel-air ratio (and temperature of combustion)[44]. . . . .	27
3.8	An example of the flame stability region in an annular combustion chamber[44]. . . . .	27
3.9	Performance characteristics of a natural gas turbine[44]. . . . .	28
3.10	The integration of a solar heat source in series with a fuel heat source[17].	30
3.11	The integration of a solar heat source in parallel with a fuel heat source[17].	30
3.12	The basic layout of a solar hybrid gas turbine system[48]. . . . .	31
3.13	The temperature-entropy diagram of a solar hybrid gas turbine[48]. . . .	31
3.14	The layout of a pressurized volumetric receiver with a secondary concentrator, and a sub-assembly of such receivers[6]. . . . .	31
3.15	A solution for the piping between the power block and the solar receiver[17].	32
3.16	The Solar Turbines Mercury 50 recuperated gas turbine[54]. . . . .	34
3.17	The recuperated Brayton cycle[55]. . . . .	34
3.18	Recuperation in a SHGT system[56]. . . . .	34
3.19	A gas turbine with air extraction for silo-type combustors[17]. . . . .	35
3.20	The operation strategy of a SHGT plant without storage as a base load power plant[17]. . . . .	38
3.21	The operation strategy of a solar thermal power plant with a high solar multiple and thermal storage[61]. . . . .	39
3.22	[17]. . . . .	40
4.1	A schematic representation of the transfer of heat in a TES system. Adapted from [63]. . . . .	41
4.2	An overview of the different types of thermal storage available for solar energy. Adapted from [64]. . . . .	42
4.3	Shifting power generation until later in the day by way of thermal storage[65]. . . . .	42
4.4	Different classifications of thermal energy storage. Adapted from [66]. .	43
4.5	A schematic diagram of a CSP plant with integrated thermal storage[20].	44

4.6	A two tank thermal storage system using molten salt as both the HTF and storage medium[70]. . . . .	45
4.7	A container of rocks for thermal energy storage[73]. . . . .	46
4.8	A packed bed of material with a flow distributor[63]. . . . .	46
4.9	An illustration of a) highly stratified and b) moderately stratified thermal storage tanks, compared to c) uniform temperature, and their equivalent stored sensible energy[63]. . . . .	47
4.10	A model of a perfect thermocline. Adapted from[76]. . . . .	47
4.11	A pressurised vessel for regenerative high-temperature heat storage[25].	48
4.12	The process of storing and releasing heat with a phase change material[66].	49
4.13	A simplified schematic of the integration of both sensible and latent heat storage in a steam generating plant[28]. . . . .	49
4.14	The T-s diagram for the power plant pictured[28]. . . . .	49
4.15	Classification of families of latent heat storage materials[66]. . . . .	50
5.1	Thermodynamic cycles and applicable approximate respective temperature ranges[83]. . . . .	55
5.2	Integration of the steam Rankine bottoming cycle at the exhaust of a gas turbine[43]. . . . .	57
5.3	The T-s-Diagram of an ideal steam Rankine cycle[43]. . . . .	57
5.4	The integration of the steam Rankine bottoming cycle in a SHGT power plant[56]. . . . .	58
5.5	The T-s-Diagram of a topping Brayton and bottoming Rankine cycle[85].	59
5.6	Energy transfer between the topping and bottoming cycles[39]. . . . .	59
5.7	The integration of an organic Rankine cycle in a SHGT power plant[61].	59
5.8	T-s-diagrams of different working fluids for the ORC[87]. . . . .	60
5.9	An air-cooled dual pressure steam Rankine bottoming cycle[58]. . . . .	61
5.10	The T-s-diagram of the dual pressure bottoming cycle[17]. . . . .	61
5.11	The indirect air cooler needed to avoid cooling water[17]. . . . .	62
5.12	The integration of an air-based bottoming cycle in a SHGT power plant[88].	63
5.13	A T-s-diagram of the air-bottoming SHGT plant proposed[88]. . . . .	64
6.1	A map of average annual DNI in Europe, Courtesy of SolarGIS[91], ©2015 GeoModel Solar . . . . .	67
6.2	DNI map of Spain with plant location. Map courtesy of SolarGIS[91], ©2015 GeoModel Solar . . . . .	68
6.3	The heliostat field layout used in the process simulation[90]. . . . .	74
6.4	The simplified simulation of the indirect thermal energy storage. . . . .	76
6.5	The simulation model of the bottoming cycle. . . . .	77



7.1	An illustration of the layout of a hybrid solar gas turbine power plant with a tower central receiver system and the power block and thermal energy storage located at ground level. . . . .	80
7.2	The process simulation model of the AB SHGT. . . . .	82
7.3	TES storage level on days of high irradiance (top) and low irradiance (bottom). . . . .	83
7.4	TES storage level (top) and fuel mass flow rate (bottom) for days of variable irradiance. . . . .	84
7.5	The process simulation model of the CCGT power plant. . . . .	87
7.6	The process simulation model of the solar reference SHGT power plant. . . . .	89
7.7	The T-s-diagram of the AB SHGT topping cycle . . . . .	91
7.8	The T-s-diagram of the AB SHGT bottoming cycle . . . . .	92
7.9	The T-s-diagram of the solar reference topping cycle . . . . .	92
7.10	The T-s-diagram of the solar reference bottoming cycle . . . . .	93
7.11	The T-s-diagram of the combined cycle gas turbine reference bottoming cycle . . . . .	93
7.12	A graphical comparison of performance aspects of the simulated cycles. . . . .	95
7.13	Relative change in total power plant efficiency compared to deviations from design parameters. . . . .	98
7.14	A graphical comparison of performance aspects of the simulated cycles. . . . .	100
D.1	An overview of the daily DNI values for the first half year of the simulation . . . . .	124
D.2	An overview of the daily DNI values for the second half year of the simulation . . . . .	125

# List of Tables

2.1	A comparison of the four main CSP technology types. Adapted from [20, 26, 27, 28]. . . . .	7
4.1	An overview of liquid thermal storage media. Adapted from [22, 66, 28]	52
4.2	An overview of solid thermal storage media. Adapted from [22, 66, 28, 72].	53
4.3	A selection of latent heat storage materials and their applicable temperature ranges. Adapted from [80] . . . . .	54
4.4	A selection of thermochemical storage media, adapted from[28, 66] . . .	54
6.1	Boundary conditions used in the process models . . . . .	69
6.2	Ambient conditions of the design point in the process models . . . . .	70
6.3	Assumptions used in the process simulation . . . . .	72
7.1	Performance characteristics of the AB SHGT power plant at design point.	81
7.2	Performance characteristics of the reference CCGT power plant at design point. . . . .	86
7.3	Performance characteristics of the solar reference power plant at design point. . . . .	88
7.4	A comparison of the steady state simulation results for the process models at design point. . . . .	94
7.5	A comparison of the performance results of the four scenarios simulated over a year. . . . .	96
7.6	Assumptions used in the process simulation . . . . .	99
7.7	The results of the validation simulation . . . . .	100



# Chapter 1

## Introduction

### 1.1 Background

Climate change driven by greenhouse gas emissions such as CO<sub>2</sub> represents a major challenge for countries all over the world in the coming decades[1, 2]. In part because of this, there is a steadily growing demand for, and rapid development within, renewable power generation. One highly promising source of renewable energy is concentrated solar power (CSP). By concentrating sunlight using large mirrors, it is possible to create temperature rises of hundreds and even thousands of degrees. This energy can then be used to power heat engines and generate electric power. In the past few years, CSP has gotten significant attention, and large-scale projects are currently under way in many regions to harness the potential of this technology. At the same time, CSP suffers to a large extent from the same drawbacks as other renewables: intermittent access to the natural resource, and a need for environmentally suitable locations, often far from where the electric power is needed the most.

This thesis aims to investigate the possibility to meet these challenges by integrating a concentrated solar power plant with a natural gas turbine, including thermal energy storage and a bottoming cycle. The objective of such hybridization is to increase the efficiency of the renewable resource utilization and to reduce carbon emissions. To do this, a process model of such a power plant has been designed and built in the process simulation software EBSILON® Professional.

### 1.2 Structure of this thesis

In order to simulate such a hybrid power plant, a literature study was carried out on relevant technologies. Design criteria were then established, and based on the boundary conditions found, a power plant simulation model was built. This model was simulated for various operating conditions in order to find power plant annual performance. The content of the thesis chapters is as follows:

## 2 1. INTRODUCTION

- Chapter 2 reviews the state of current concentrated solar power technologies, and establishes relevant definitions necessary to describe the simulation model used in this thesis.
- Chapter 3 consists of literature study of conventional natural gas turbines, and on the hybridization of these in a solar hybrid gas turbine (SHGT) power plant, including component integration, performance indicators and the operational strategy of such a plant.
- Chapter 4 consists of a literature study on thermal energy storage, with emphasis on storage technologies relevant for CSP.
- Chapter 5 contains consists of a literature study of bottoming cycles, with four bottoming cycles selected as especially relevant for the SHGT.
- Chapter 6 presents the background for the process simulation methodology, by deciding on a location for the candidate power plant, allowing for establishment of its boundary conditions, as well as finding assumptions and design criteria necessary for the process simulations, and details the simulation of the various parts of the plant.
- Chapter 7 presents the process simulation models created, along with their performance characteristics, and presents and compares the results of the simulations, along with sensitivity studies and model validation.
- Chapter 8 provides conclusions on the result of the thesis as well as suggestions for further work related to the topic.

### 1.3 Risk Assessment

No work with the potential to adversely affect health, safety or security of any persons involved has been carried out in the course of this thesis work. For this reason, further risk assessment has not been performed.

# Chapter 2

## Concentrated Solar Power - CSP

CSP technology uses giant mirrors or lenses to harness large amounts of sunlight for power generation. After photovoltaic (PV) systems, CSP is currently the major technology for solar electricity production[3]. Unlike PV however, CSP concentrates and collects solar thermal radiation, which is converted through a thermodynamic cycle to power a generator.

Concentrated thermal solar power has been harnessed for heat, and in some cases for mechanical work through steam engines, for centuries[4]. The concentration of solar thermal radiation for commercial electric power generation was first performed in the Mojave desert of California in the 1980s[5]. Since then, research and development in the field has been steadily increasing, and the global electric power capacity from solar thermal power plants has seen rapid development in recent years, as shown in Figure 2.1. In fact, the annual electric energy generated from CSP exceeded 3 TWh already in 2013[6], and current CSP capacity is currently nearly 4.8  $GW_e$ . This growth is expected to continue in the coming years, as there are currently plans under way for large projects all over the world[7, 8, 9]; such as in Morocco, where 160 $MW_e$  of CSP power was brought online in 2015 and a total capacity of 580 $MW_e$  is planned by 2020[10, 11, 12]. Major projects are also underway in the China, Chile, Egypt, The United Arab Emirates, India, South Africa, Israel and Saudi Arabia[13, 10, 14, 6]. In the Saudi case, a deployment of a total of 25  $GW_e$  capacity, more than five times the entire global total of 2014, is underway, with completion currently expected in 2040[15]. Power output from solar thermal power plants is expected by the International Energy Agency to exceed that of photovoltaics by 2030[16, 17].

A major benefit of CSP is its reliance on simple technology that is already commercially available, such as mirrors, piping, insulated storage elements, and steam or gas turbine power generation systems. Because of this - and because there are still many related fields with potential for technological development - CSP is a highly promising technology for large scale renewable power generation at relatively

low levelized cost of electricity (LCOE) if mass-produced in areas with sufficient solar resources and infrastructure[18, 19]. The high temperatures generated in CSP plants are also expected to enable the production of so-called solar fuels, primarily hydrogen,  $H_2$ , through thermochemical processes at competitive costs in the future[9].

## 2.1 Focusing Sunlight

CSP relies on raising the temperature at a focal point by focusing light in much the same way as with a magnifying glass on a sunny day. Concave mirrors collect and focus a large amount of light with the focal point at a receiver, and this receiver can be heated to a high temperature. The received functions as a heat exchanger, which is filled with a fluid, usually thermal oil, molten salt, water/steam or pressurized air. In CSP technology, this aptly named heat transfer fluid (HTF) absorbs energy from the receiver and carries away the heat to enable work to be done in a turbine operating according to a thermodynamic power cycle[20, 6].

In order for the sunlight, or *irradiance*, in question to be used in CSP, it must be focused and concentrated. CSP technology cannot utilize diffuse sunlight coming from various directions - for example that which has been scattered through the atmosphere. For this reason, only the direct beam irradiance, which has a direction normal to a plane pointed toward the sun, is considered. This is the light available

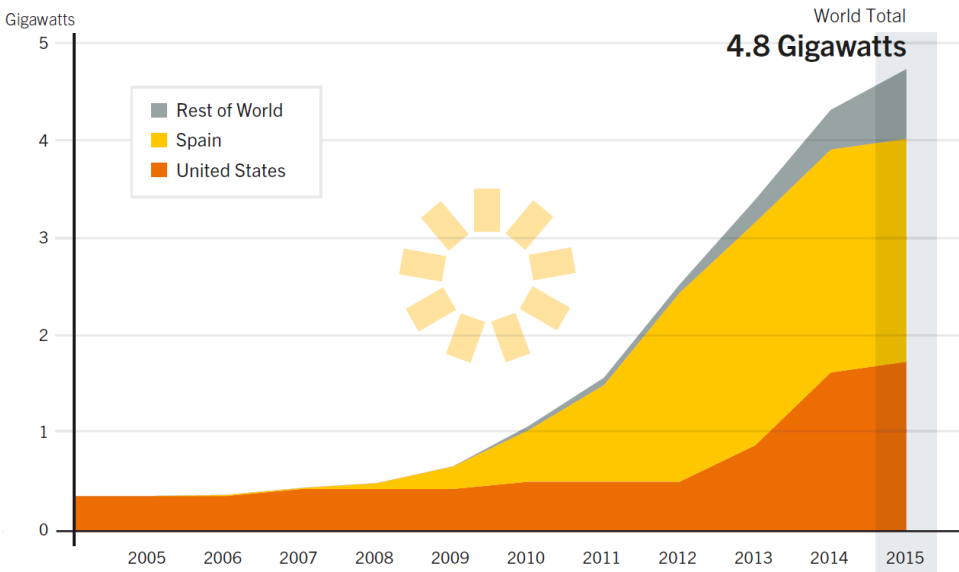


**Figure 2.1:** Recent development in world total CSP capacity, adapted from [10]

for focusing, and is known as direct normal irradiance (DNI), or alternatively as direct insolation. This is a vital difference between CSP and PV technology, as PV can utilize also a significant part of the diffuse irradiance.

In total, CSP technology is of little use at higher latitudes[19, 21] or in areas with frequent inclement weather - an overcast sky will reduce the available DNI to effectively zero. Figure 2.2 shows the process of attenuation of light through the atmosphere at the solar equator. DNI is further reduced at latitudes further from the equator because the sunlight must travel through a longer distance in the atmosphere. The ratio of the distance traveled to the minimum is known as the air mass ratio, and the basic principle is shown in Figure 2.3. Figure 2.4 shows the world effective average annual DNI at ground level.

Because the sun appears to move across the sky, the solar collectors generally must be able to track it in order to maintain a focal point at the desired location. A distinction is made between *irradiance*, which is the instantaneous solar energy flux on an area per unit of time - usually given in  $\text{W}/\text{m}^2$  - and *irradiation*, which is the total solar energy falling on an area over a given time - usually given in  $\text{kWh}/\text{m}^2$  - in the course of for example a year. In literature, these terms are often used interchangeably, but it should be clear from the context or units which is meant[19].

## 2.2 CSP Technologies

A typical CSP system chiefly consists of three subsystems: a solar receiver, a solar collector/concentrator, and a power conversion system that generates electric power from the thermal energy in the HTF. The majority of CSP plants being built today also integrate some form of thermal energy storage systems[10]. In addition, it is common to include a fossil fuel back-up power system for system start up, transient operation during variations in solar irradiance or increased efficiency. The basic flow diagram for a CSP plant is shown in Figure 2.5. By co-firing with fossil fuels, the power output of the plant can be maintained at a constant level, or more easily varied to meet demand at different times of the day. Firing or co-firing with fuel is also necessary for plant start up if the HTF used is molten salts, as these will need to be melted in the pipes if the plant has been shut down for an extended period[3, 24].

Figure 2.6 shows the operation of a CSP plant employing both thermal energy storage and a backup source of heat from fuel. Such a configuration allows the plant to function as a base load power plant for 24 hours a day. The hybridization of a CSP system with a gas turbine co-fired with natural gas is examined in greater detail in chapter 3.

The geometric concentration ratio,  $C_{onc}$ , defined as the ratio between the



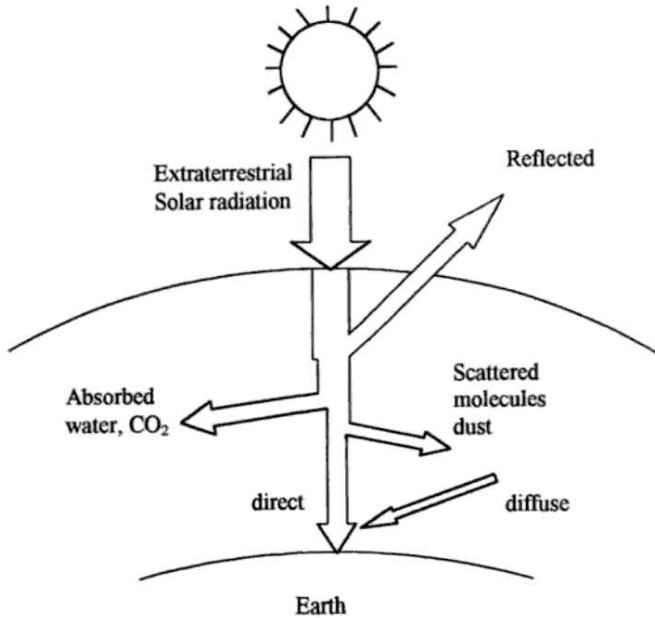


**Figure 2.2:** The attenuation of solar radiation as it passes through the atmosphere[22].

reflective surface of the concentrator and the illuminated surface of the receiver. This ratio has a vital impact on CSP system performance, and higher ratios are generally necessary for higher temperatures and, in turn, higher solar multiples and/or efficiencies, and will be detailed further in section 2.3.

In principle, the CSP technologies in use depend on, and can be classified by, two major subsystems: the solar collector and the solar receiver. The collector can focus light either at a single fixed point, which requires tracking the sun - physically rotating the collector along two axes. Alternatively, the concentrator can focus light along a fixed line, which only requires tracking on one axis. In either case, light is focused by use of highly reflective mirrors to generate high temperatures. The other major subsystem, the solar receiver, can either move along with the motion of the mirrors, or be mounted at a fixed structure which does not move. Fixing the position of the solar receiver limits the maximum possible concentration factor of the mirrors, because they must be subdivided due to practical size restrictions and no longer have a perfectly paraboloid shape. Nevertheless, such a configuration allows for a far greater total collector surface area, and therefore higher operating temperatures in the receiver. Concentration ratios are in any case limited by practical and cost

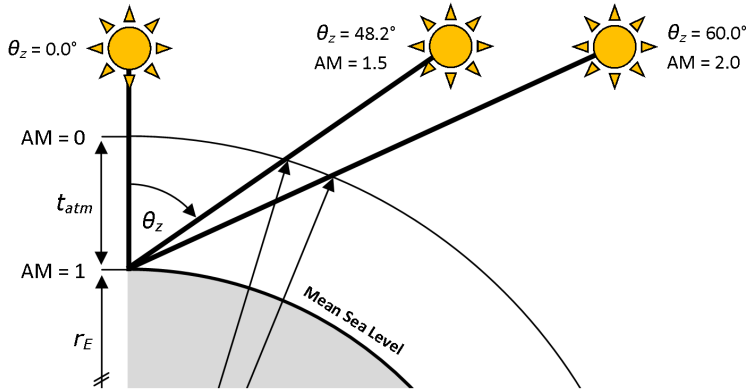


**Figure 2.3:** The air mass ratio at different solar angles[17].

considerations related to the size of the collector. Based on the two collector and the two receiver configurations, a total of four major categories of CSP technology is possible, and the basic principle of these is illustrated in Figure 2.7. A comparison of their typical main characteristics based on current technology is summarized in Table 2.1.

Collector Type	Focus type	Typical capacity	Solar Concentration Ratio	Operating Temperature	Maturity of technology
		[ $MW_e$ ]		[ $^{\circ}C$ ]	
Parabolic Trough	Linear	10 - 250	70-80	50-400	Advanced - commercially proven
Central Receiver	Point	10 - 150	300-1000	300-1200	Moderate - commercial projects under construction
Linear Fresnel	Linear	10 - 200	25-100	50-300	Recent development - pilot projects
Parabolic Dish	Point	0.01 - 0.4	1000-3000	150-1500	Very recent development - demonstration projects

**Table 2.1:** A comparison of the four main CSP technology types. Adapted from [20, 26, 27, 28].

### 2.2.1 Parabolic Trough Technology

The parabolic trough system represents the highest technological maturity, and is by far the most commonly used and commercially available, of the available CSP technologies. This concentrator consists of a silvered mirror in the shape of a parabolic trough, which focuses light along a linear receiver fixed to the collector.

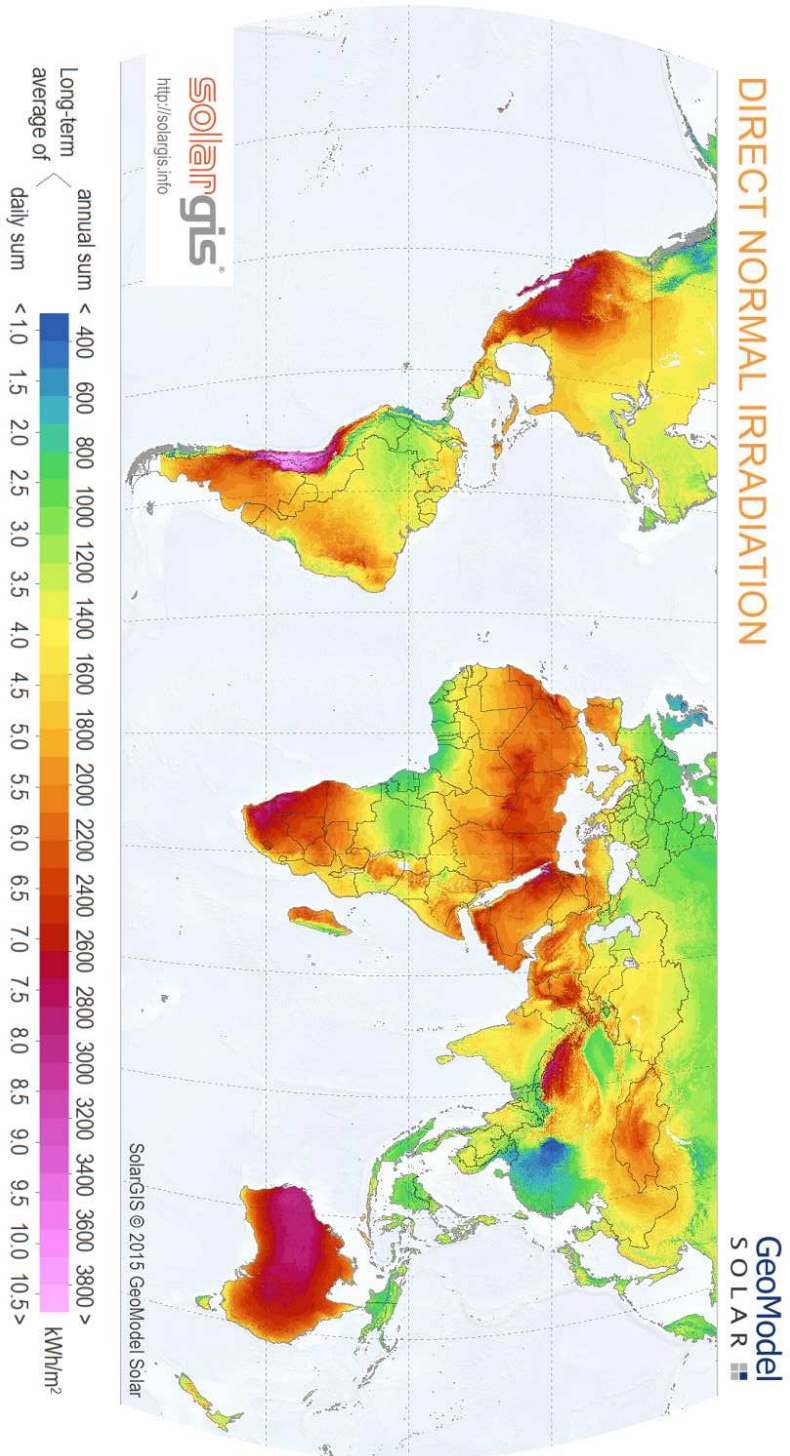
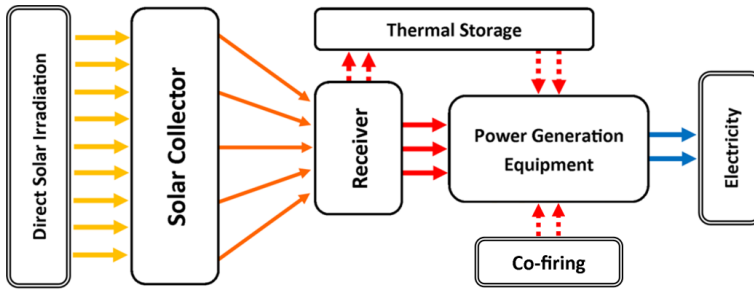
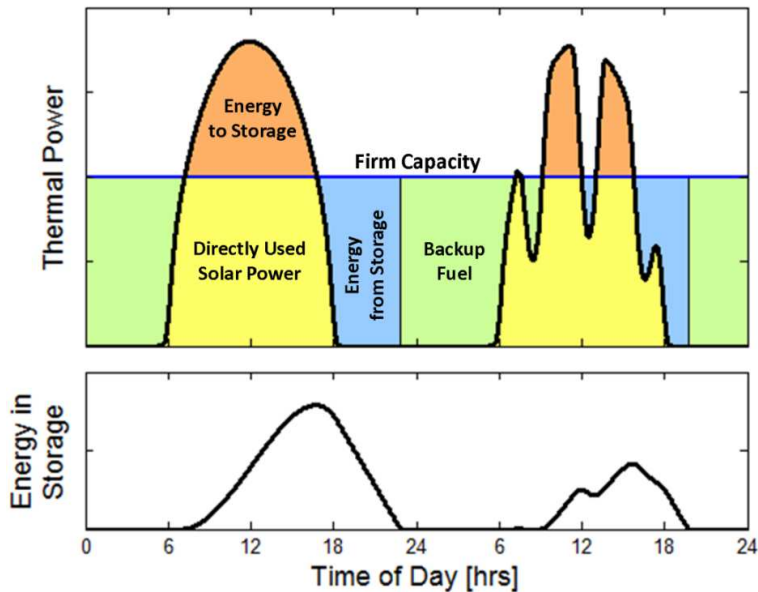


Figure 2.4: A map of world annual average DNI, Courtesy of SolarGIS[23], DNI Solar Map © 2016 GeoModel Solar



**Figure 2.5:** Flow chart for a general CSP power plant including thermal storage and (fossil) fuel for backup and co-firing[17]



**Figure 2.6:** The operation strategy of a CSP plant with both thermal energy storage and (fossil) fuel as an energy back-up, as a base load plant[25].

The HTF flows through the receiver - usually a thin pipe of high-absorbitivity steel, insulated with an evacuated transparent glass pipe on the outside[24] - as shown in Figure 2.9, and the receiver moves along with the collector as it tracks the sun along a single axis[20], as in Figure 2.8. While it is theoretically possible to focus sunlight up to 215-fold in such a mirror trough, practical considerations usually limit the actual concentration in operation to less than 100-fold[6, 26]. This can still raise the temperature to several hundred degrees, which is sufficient to power a steam turbine operating according to the Rankine Cycle[22]. Most of these CSP systems

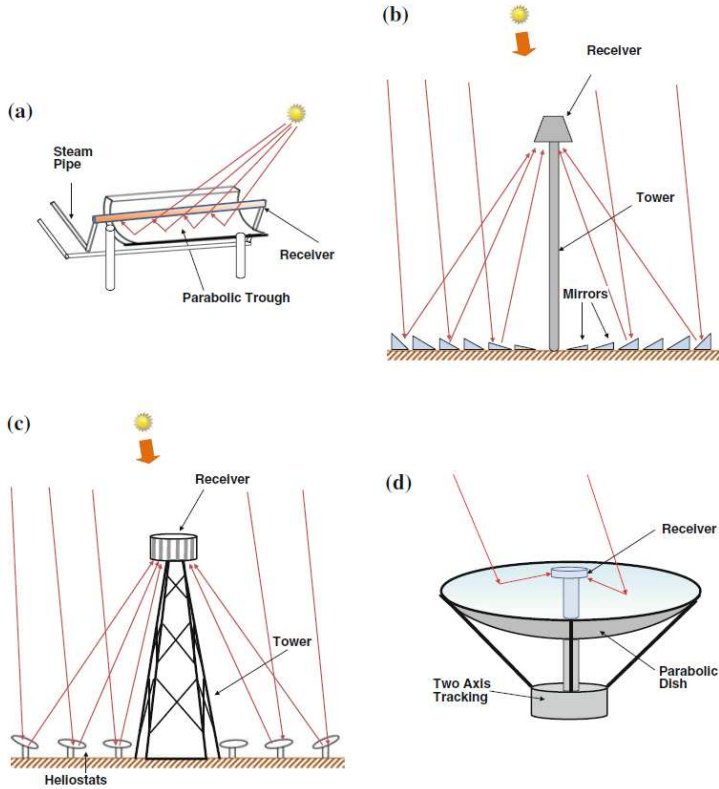


**Figure 2.7:** Principles of the four main CSP technology types: (a) parabolic troughs; (b) linear fresnel collectors; (c) central receiver system / power tower and (d) parabolic dish[26].

use a synthetic thermal oil as their HTF[6].

### 2.2.2 Sentral Receiver Systems

The central receiver system (CRS), or solar power tower, technology is the second most mature of the CSP technologies, and is the focus of this thesis. These power plants consist of a central tower at a high elevation and hundreds or thousands of giant flat mirrors. These mirrors, known as heliostats, are tracked along two axes and reflect sunlight constantly at a fixed point on the central receiver at the top of the tower. The heliostats can be weight-balanced, to ensure low power consumption during tracking, as well as self-powered with a small PV-panel and battery on each unit[32]. The total reflecting surface in such systems can have reflecting areas of hundreds of thousands of square meters. Because of this, the receiver part of the tower, which

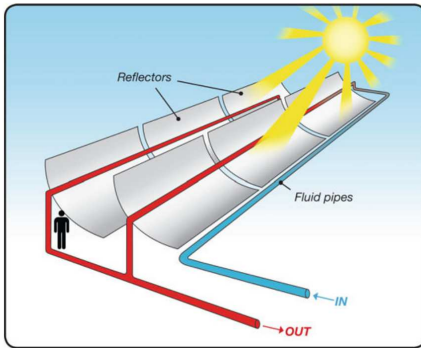


**Figure 2.8:** A schematic of a parabolic trough system[20].

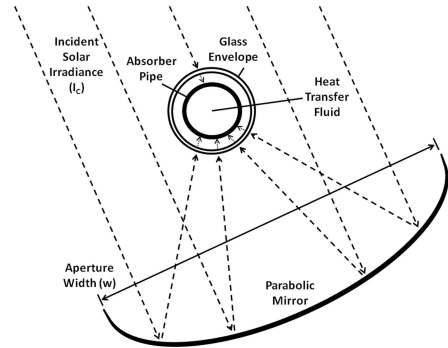


**Figure 2.9:** A cut-away of the trough configuration as seen from its side[29].



**Figure 2.10:** Front view of heliostats[30].

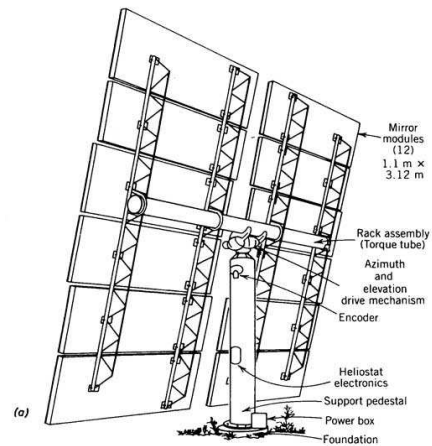
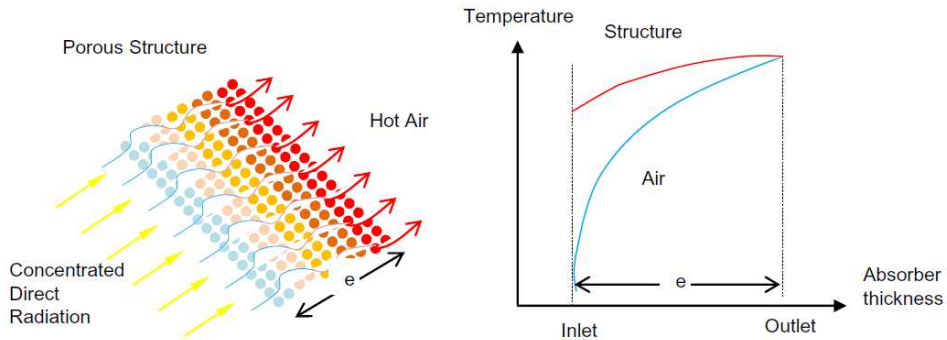


**Figure 2.11:** Rear view of a heliostat[31].

functions as a heat exchanger to the HTF, can easily reach temperatures well in excess of  $1,000^{\circ}\text{C}$ [18, 14]. The heliostats are can be individually controlled, allowing for partial defocusing of the field. This is necessary for part-load operation of the plant, in emergency shut-down situations or when the incident solar radiation exceeds the nominal plant conditions. The heliostat fields require continuous maintenance in the form of cleaning, as CRS plants are located in arid, dusty conditions, which leads to additional water usage at the plant.

While using steam and molten salts as HTFs in the central receiver is widespread,

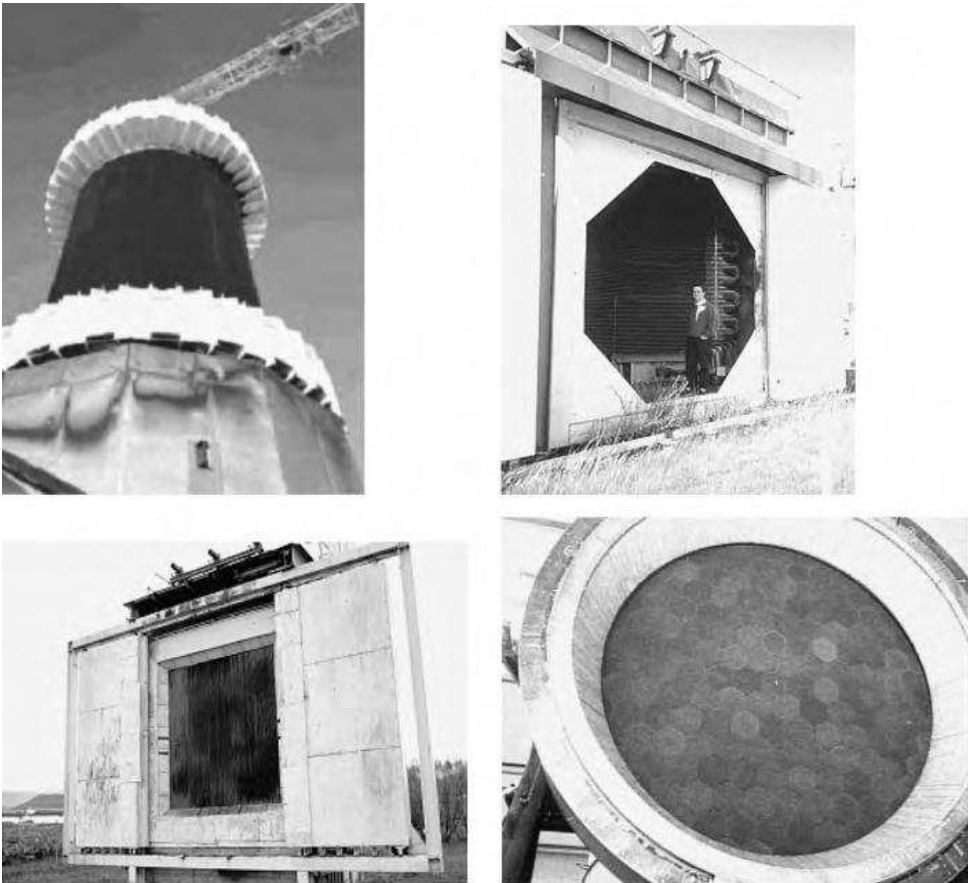
they are also considered, respectively, relatively impractical and dangerous[6]. The heat exchanger for these fluids is a basic tubular receiver, with the HTF flowing through the tubes, mounted externally or internally in an enclosure. Compressed air shows promise as a HTF in CRS systems, especially considering its utility if preheated in the CRS for use in gas turbines, as is the topic of this thesis and explained in further detail in chapter 3. CRS using air as the HTF utilize volumetric receivers, which may either be atmospheric or pressurized. Atmospheric receivers function both as the solar receiver and as the fresh air intake, in cases where the air as HTF does not need to be significantly pressurized. The heated air can be used to generate steam for a steam turbine, and exhausted at a location directly adjacent to the receiver. This recycles some of the heat released, as up to approximately 60% of the exhaust air can be re-admitted into the system[18]. The volumetric receiver relies on using a porous heat absorber material to capture heat from the incoming light as pictured in Figure 2.12. This provides a drastically larger total heat transfer surface area compared to tubular receivers[14, 6].



**Figure 2.12:** A presentation of the heat transfer principle in a volumetric receiver[14].

The heliostat field of the CRS is of vital importance to plant cost and performance. While the field makes up the largest investment of a CRS plant, each of the hundreds or thousands of heliostats is relatively simple to make, and mass-production is therefore expected to drastically reduce their cost[18]. The layout of the heliostat field also requires large land areas, and each heliostat has relatively low optical efficiency. There are five major losses related to the heliostats that impact their optical efficiency[33]:

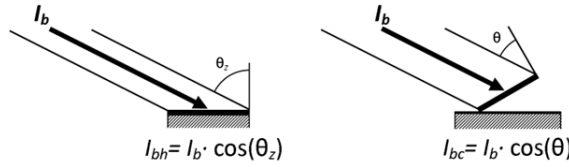
- The cosine effect, caused by the angle of the impacting solar radiation compared to that of the reflecting surface as shown in Figure 2.14.



**Figure 2.13:** Different receiver types; from top left and clockwise: external tubular cylindrical; cavity tubular; billboard tubular and volumetric atmospheric[24].

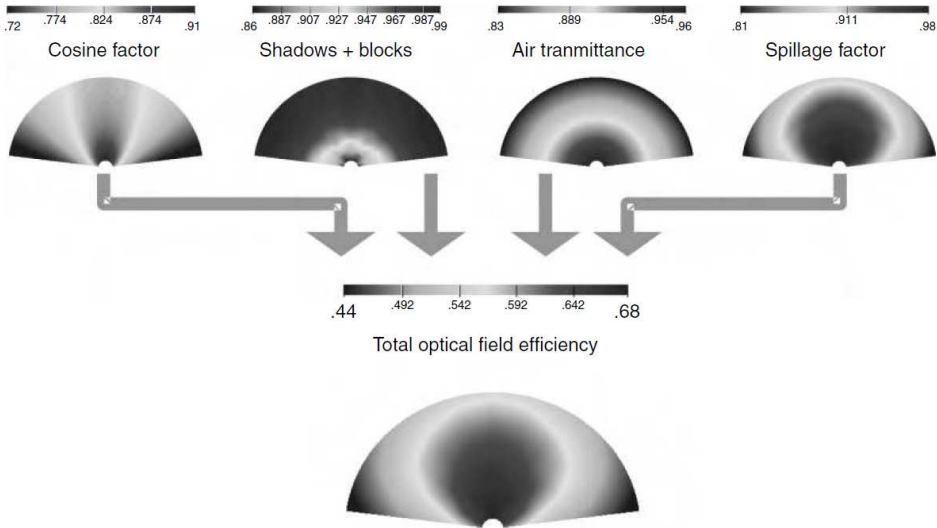
- Shadowing and blocking, as the heliostats get in the way of either the incident or reflected radiation of neighboring heliostats.
- Mirror reflectivity, which is constant for all heliostats, but is reduced by soiling from for example dust.
- Atmospheric attenuation, which decreases if there is water vapor or other aerosols in the air.
- Receiver spillage, as each flat heliostat reflector does not focus the beam of light well, and some fraction of the reflected light does not impact the receiver.





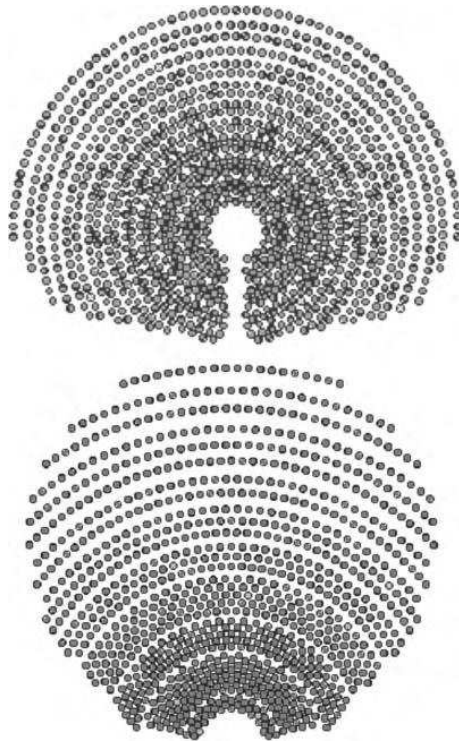
**Figure 2.14:** The reduction in effective surface area due to receiver angle[17].

Figure 2.15 shows the effects of the different loss factors for a heliostat field, which is calculated for different locations in a grid and combined to form a total optical efficiency for each point. Based on this total efficiency, a solar field is then designed. The location of the power plant also directly effects the efficiency of the field, as plants closer to the equator will have the sun more directly overhead for larger fractions of the day. Figure 2.16 shows two different fields of equal thermal power at different latitudes. The bottom field shows a field facing North or South (depending on the hemisphere), and is suitable for higher (or lower) latitudes, while the upper field is designed for a location closer to the equator. The heliostat field should be specifically designed for each solar thermal power plant to take into account the abovementioned effects[24].



**Figure 2.15:** An illustration of the total efficiencies of a heliostat field[24].

While the parabolic trough currently accounts for the majority of CSP plants in operation, the CRS is viewed as the most promising for future development on a



**Figure 2.16:** Two different heliostat fields located close to the equator (top) and at higher latitudes[24].

global scale - especially in power ranges exceeding  $100 MW_e$ . In addition to allowing for higher temperatures and efficiencies, perhaps the biggest benefit related to this technology is the simplicity of the heliostats which make up the largest cost of the power plant. Mass production of these is expected to lead to major cost reductions in the deployment of CRS power plants [14, 18, 19].

### 2.2.3 Fresnel and Parabolic Dish Technologies

The linear fresnel collector is composed of narrow mirrors arranged side to side like vanes in venetian blinds as an approximation to the concave lenses of the trough configuration[6]. This lets the collector lie closer to the ground, offering less wind resistance and making it possible to construct very large collector surface areas. The main benefit of the fresnel linear collector is its simplified and cost-effective construction compared to the parabolic trough technology, as well as the benefit of having a fixed solar receiver tube. This system achieves the lowest temperatures of the CSP technologies due to its low achievable concentration ratios. Although the

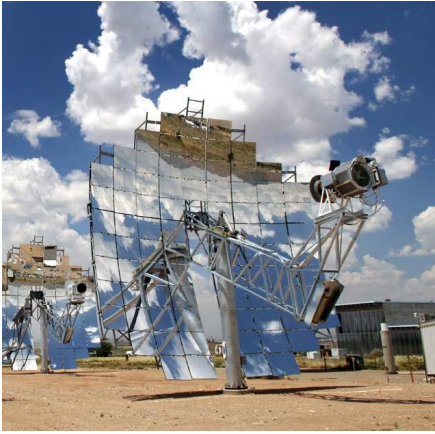


**Figure 2.17:** A dish sterling CSP system[34].



**Figure 2.18:** A linear fresnel CSP system[35].

electric conversion ratio of this system is the lowest of the CSP technologies, it is associated with significantly lower construction costs but requires more land area per kW than the CRS and trough systems[19]. This technology is currently still in an early state of development, and not in widespread use[18].

The parabolic dish system consists of a mirror in the shape of parabola, as pictured in Figure 2.17, and requires tracking on two axes to always point toward the sun. It is the most efficient of the solar collection methods, and can in theory concentrate sunlight to a concentration of 10,000 suns intensity, which would allow for extremely high temperatures[19]. With current technology however, the parabolic dish usually achieves a concentration ratio of about 2,000. Use of these systems is not widespread, and each dish system in use today usually generates 5 - 25  $kW_e$  of power[20]. Due to its very high concentration ratio, the dish system can reach a very high solar-to-grid conversion efficiency of more than 31%[34]. In theory, it should be possible to increase power production from the related CSP power plant up to 300  $MW_e$  by use of advanced Stirling engines and a large amount of collectors[27]. It must be noted that while this parabolic dish stirling technology shows large promise, it is highly reliant on future technological advances[36]. It would also require thousands of stirling engines or microturbines compared to a single large turbogenerator in a CRS concept of equivalent power output[18].

## 2.3 Solar Concentration

In this section, the efficiency of the solar concentrators and receiver will be explained. All the solar power that passes through a CSP plant does so through the solar receiver, and the concentration of incident sunlight is therefore clearly vital for plant performance. Especially important is the relationship between increasing temperature and increasing concentration ratios. All of the following equations are collected from (Romero-Alvarez, 2007) [24].

In CSP technologies a system is employed to redirect solar radiation onto a receiver surface. The total area of the solar concentrators,  $A_c$  can be compared with the total area of the solar receiver,  $A_{abs}$  to find the CSP plant's geometric concentration ratio:

$$CR_g = \frac{A_{abs}}{A_c}. \quad (2.1)$$

A theoretical solar receiver performing like a blackbody would have only emissive heat loss, without radiation loss. Due to their geometry, cavity and geometric receivers do approach this condition[24]. The efficiency of the solar receiver will then rely on  $\alpha$ ,  $\tau$  and  $\varepsilon$ [24]. These are, respectively, the absorbance, transmittance and emittance of the absorber. As increasing levels of thermal radiation heat the absorber, the cooling provided by the HTF combined with increasing infrared radiation losses will lead to a steady state:

$$\frac{Q_{gain}}{A} = \alpha C\phi - \sigma\varepsilon(t_{abs}^4 - t_{amb}^4). \quad (2.2)$$

Here,  $Q_{gain}$ , is the useful power outlet or the power gain from the solar receiver,  $A$  is the aperture area of the absorber,  $\sigma$  is the Stefan Boltzmann constant, [5.67e-08  $W/m^2K^4$ ],  $\phi$  is the direct normal irradiance, and  $T_{abs}$  and  $T_{amb}$ , are respectively the temperature of the absorber and the ambient temperature which the absorber radiates to. Solar receiver efficiency is defined as

$$\eta_{rec} = \frac{Q_{gain}/A}{C\phi}. \quad (2.3)$$

Equation 2.2 is then substituted into Equation 2.3, to find[24]

$$\eta_{rec} = \alpha - \sigma\varepsilon \frac{(t_{abs}^4 - t_{amb}^4)}{C\phi}. \quad (2.4)$$

Equation 2.4 is plotted in Figure 2.19 for different concentration ratios, and shows that there is a maximum theoretical receiver efficiency for relatively low temperatures[24].

Because the solar thermal power is to be used in a heat engine, it can be useful to consider the Carnot efficiency,

$$\eta_{max} = 1 - \frac{T_C}{T_H} \tag{2.5}$$

which is the maximum possible efficiency of a heat engine operating with a reversible process between a hot temperature  $T_H$  and a cold temperature  $T_C$ . Equation 2.5 is overlaid Equation 2.4 is Figure 2.20. From this figure, it is clear that there is a conflicting maximum possible receiver optical efficiency at low temperatures, and a maximum carnot efficiency at higher temperatures. By multiplying these efficiencies, we can find that for each concentration ratio, there is an optimal temperature for a combined optical and Carnot efficiency, limiting the maximum possible efficiency of a CSP plant. The graph shown in Figure 2.21 is valid for a receiver of specific emissivity and absorbance, but for each geometric concentration ratio, it is clear that there exists a theoretical optimum operating temperature for use in a carnot cycle[24].

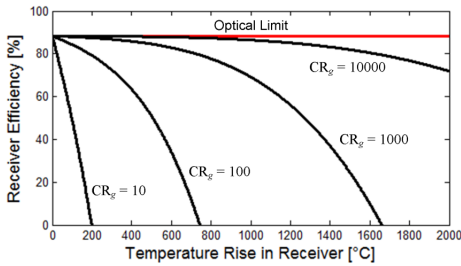


**Figure 2.19:** An illustration of the maximum possible theoretical receiver efficiency for different concentration ratios[17].

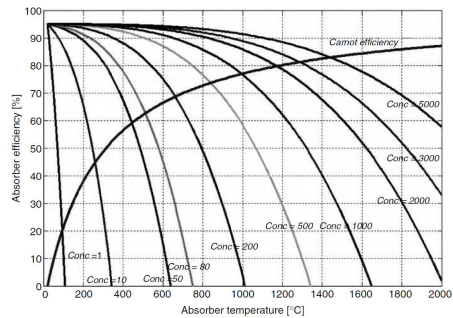


**Figure 2.20:** Different optimal receiver efficiencies plotted against the carnot efficiency[24].

Another factor with relevance for a CSP plant is the solar multiple, SM. This is defined as the ratio of the nominal thermal power delivered by the solar concentrator,

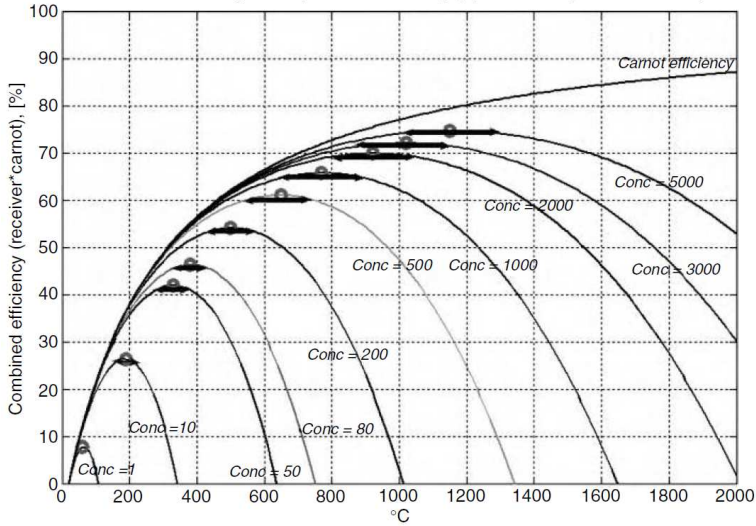


**Figure 2.21:** The combined optimal system efficiency of a receiver and the carnot cycle[24].

$\dot{Q}_{conc,nom}^*$ , compared to the nominal power required by the solar receiver,  $\dot{Q}_{conc,nom}^*$ , [17]:

$$SM = \frac{\dot{Q}_{conc,nom}^*}{\dot{Q}_{rec,nom}^*} \quad (2.6)$$

The nominal power from the collector field can be defined as that which is collected during the design condition, typically with a DNI availability of  $850 \text{ W/m}^2$  at solar noon at the spring or fall equinox. For a plant with  $SM=1$ , the thermal power delivered by the collector field is then equal to the nominal required power at at this design condition[17, 37]. Because a plant with  $SM=1$  would deliver less than nominal power at all less favourable conditions than the design one, it is common to slightly oversize the solar collector area. Figure 2.22 shows the incremental increase in thermal energy provided by increasing the solar multiple. In instances where the solar heat provided is greater than the nominal, part of the collector area must generally be defocused in order to avoid damage to the receiver, unless thermal storage is integrated in the plant, and the excess energy is lost. From the figure, it is clear that beyond a certain solar multiple, it is not economically feasible to increase the field size further, and a  $SM$  value of 1.1 to 1.5 is typically used. For conventional CSP plants utilizing storage, a the solar multiple may be between 3 to 5[38].

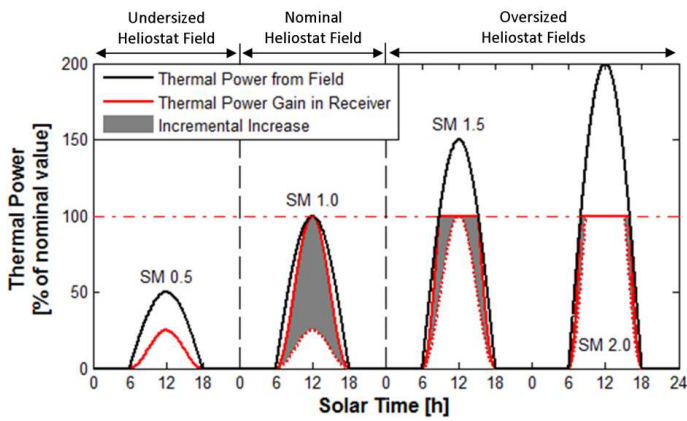


**Figure 2.22:** An illustration of the incremental increase in power available by increasing the solar multiple[17].

# Chapter 3

## The Solar Hybrid Gas Turbine

Natural gas-powered power plants using gas turbines represent a less polluting alternative to coal, both in terms of carbon emissions and local pollution. They also have the added benefit of large power flexibility, making them especially useful for dispatchable power generation. An illustration of the cross section a gas turbine for power generation is shown in Figure 3.1. In the first half of this chapter, gas turbine power plant technology relevant for the thesis is outlined. In the second half of the chapter, the potential for, and challenges associated with, combining these with a central receiver system is discussed as background to chapter 6 on process simulation.

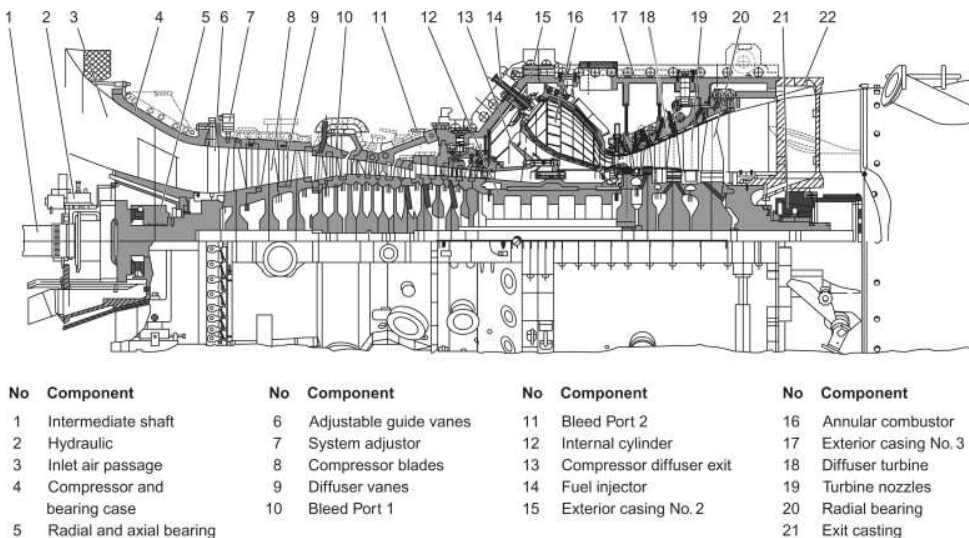


**Figure 3.1:** An illustration of the components of a gas turbine by Siemens[39].

With recent advances in material technology, the solar receiver in a CRS solar thermal power plant can currently reach temperatures of up to 1000 °C to 1200 °C,



and temperatures as high as 1500 °C and above may be possible in the future[40]. Such temperatures are high enough to make utilizing a air brayton cycle in a gas turbine in a CSP plant feasible. The brayton cycle is closer in efficiency than most other power plant technologies to the carnot cycle, which is the theoretical maximum for any heat engine, and so a power plant based on a solar hybrid gas turbine (SHGT) can be expected to reach higher efficiencies than the currently existing solar technologies[41]. The principles related to the solar part of the plant have largely been discussed in chapter 2, and so this chapter will focus on the unique features of a SHGT power plant.

### 3.1 The Brayton Cycle

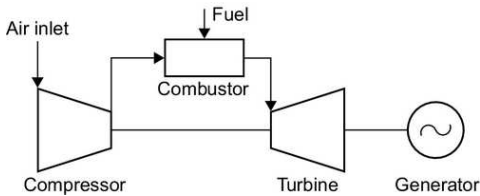


**Figure 3.2:** A block diagram of a gas turbine connected to a generator for power generation[42].

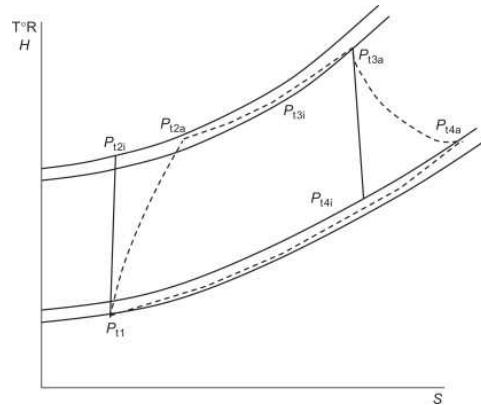


**Figure 3.3:** A temperature-entropy diagram of the Bratyon cycle including pressure losses[39].

In this thesis, a simple cycle gas turbine, a block diagram of which is shown in Figure 3.2, is integrated with a central receiver CSP system. A basic gas turbine operates according to the thermodynamic Brayton cycle, shown in a temperature-entropy (T-s)-diagram in Figure 3.3. In the diagram the move from point 1 to point 2 represents the air passing through the compressor. As it does, friction causes irreversible losses, here represented in the graph by a move to the right on the entropy axis, as opposed to an isentropic process, which would have led to point 2i. After passing through the combustion chamber, shown as in the figure as the distance between points 2 and 3 along a constant pressure curve with rising temperature, the burnt air is passed through the turbine. As it does, energy is converted from the hot gases into mechanical power, which drives both the compressor and an electric generator. Irreversibilities also lead to losses that drive the end state of point 4 to a

point of higher entropy. While it is possible to recycle the flue gas from point four to point 1 in the T-s-diagram, this requires some form of heat exchange or cooling. In a simple-cycle gas turbine, it is simply vented from the system, leading to a loss of thermal energy. For power generation, the turbine produces mechanical work by turning a shaft, and this mechanical power is converted into electric power by a generator. The electric power output from this system is written as follows[43]:

$$\dot{W} = \dot{W}_{shaft} \cdot \eta_{generator}, \quad (3.1)$$

where  $\dot{W}_{shaft}$  denotes the power provided by the shaft to an electric generator with efficiency  $\eta_{generator}$ .

## 3.2 Conventional Gas Turbine Components

### 3.2.1 Compressors

Modern turbocompressors are generally divided into two major categories: radial and axial. While air enters in the axial direction of both configurations, it exits in the axial direction from the axial compressors, and from the radial direction of the radial compressor. For this thesis, an axial turbocompressor is the most relevant, as these can maintain the large mass flows needed for a power plant of medium to large sizes. In order to describe the performance of a compressor, the stagnation pressure ratios and temperature ratios are plotted against the non-dimensional mass flow for various operating conditions at various non-dimensional rotational speeds. By using the relation described in Equation 3.2, the compressor isentropic performance characteristics can be plotted [44, 39].

$$\eta_{c,is} = \frac{\text{Actual work}}{\text{Isentropic work}} = \frac{(-\dot{W}_{cv}/\dot{m})_{is}}{-\dot{W}_{cv}/\dot{m}} = \frac{T_{02,is}T_{01}}{T_{02}T_{01}} = \frac{\frac{p_{01}}{p_{02}}^{\frac{k-1}{k}} - 1}{\frac{T_{02}}{T_{01}} - 1}. \quad (3.2)$$

Figure 3.4 shows the performance characteristics of an axial compressor. The lines of constant speed in the top graph correspond to the lines in the bottom graph, and by combining these two figures, it is possible to draw what is known as the compressor map, shown in Figure 3.5. The compressor map is a powerful tool for predicting compressor performance during both on- and off-design conditions, and are a vital part of the design of a compressor for use in a gas turbine. It is important to note that if the back pressure in front of a compressor increases to such an extent that it can no longer force gas from the outlet, the flow through the compressor will reverse itself in what is known as a compressor surge. The performance area where

this will occur is to the left of the so-called surge line or surge limit in the figures [44].

The polytropic efficiency of the compressor, which is the real aerodynamic efficiency is:

$$\eta_{c,p} = \frac{\left[1 + \frac{dP_{T2}}{P_{T1}}\right]^{\frac{\gamma-1}{\gamma}} - 1}{\left[1 + \frac{dP_{T2}}{P_{T1}}\right]^{\frac{n-1}{n}} - 1}, \quad (3.3)$$

which can be shown[39] to be equivalent to

$$\eta_{c,p} = \frac{\frac{\gamma-1}{\gamma}}{\frac{n-1}{n}}, \quad (3.4)$$

where  $\gamma$  is the ratio between the specific heats between inlet and outlet and  $n$  is a polytropic exponent describing the adiabatic process.

### 3.2.2 Combustion chambers

The combustion chamber of a gas turbine is complex, and will not be dealt with in detail in this thesis. Of special relevance however for gas turbine integration in a solar thermal power plant is the combustion chamber technology chosen. Gas turbine combustion chambers are categorized as annular, can-annular or silo-type, and most modern gas turbines utilize annular or can-annular combustors[39]. However, as will be discussed in section 3.3, annular and can-annular combustors are generally not practically implementable in a hybrid solar gas turbine plant, and can combustors can mostly only be used if they are mounted externally on the turbine. The most relevant combustors for solar integration are can combustors and the older silo-type, mounted externally on the gas turbine. An example of such a combustor is shown in Figure 3.6.

The emissions generated by a gas turbine power plant depend largely on the combustion temperature, as shown in figure Figure 3.7, as well as the time the gas is exposed to the combustion temperature. In addition, maintaining stable combustion in the combustion chamber depends on the fuel-air ratio and velocities and mass flows involved. This depends on the individual combustor, but an example is given in Figure 3.8.

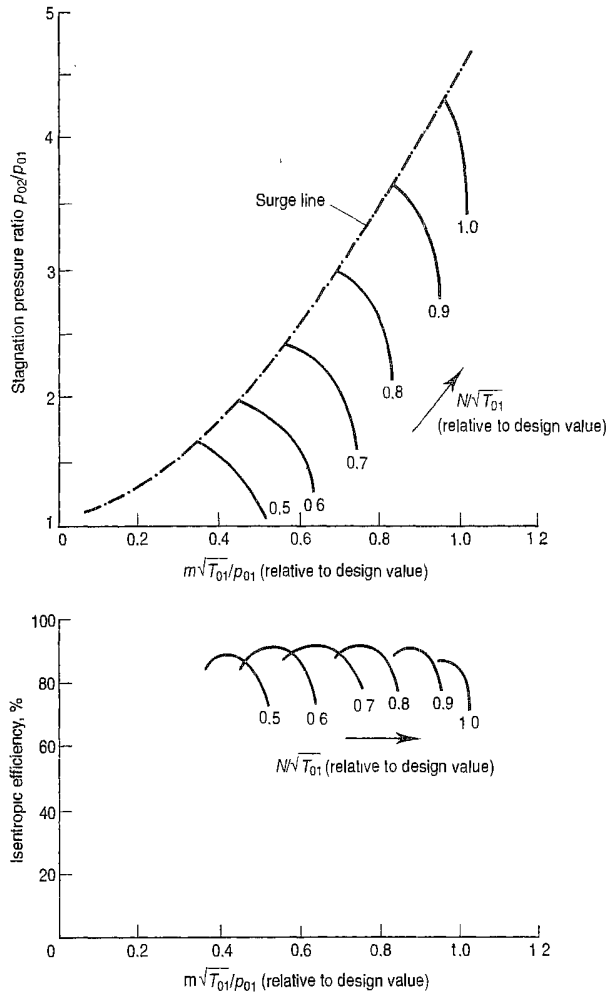
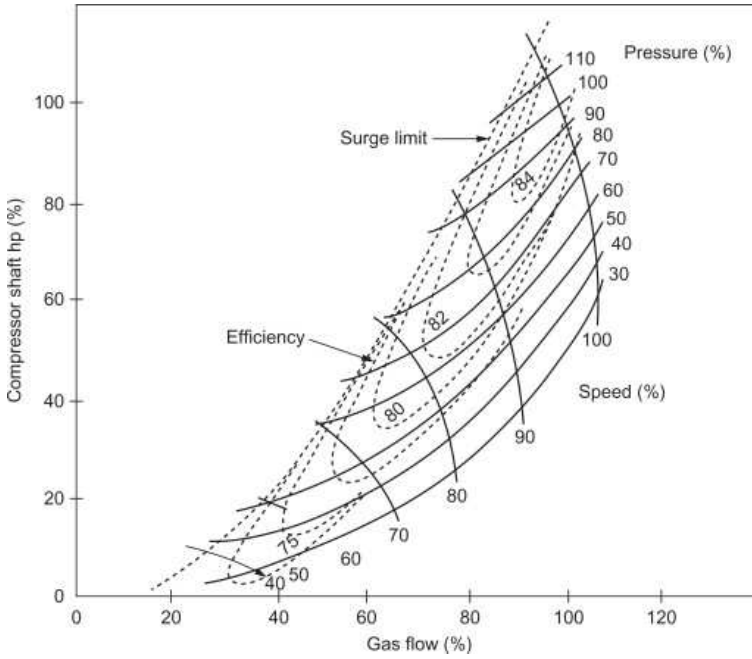


Figure 3.4: Performance characteristics of an axial compressor[45].

### 3.2.3 Turbines

Like with compressors, turbines are generally denoted as either axial or radial, and as with compressors, axial turbines are better suited for the greater mass flow rates involved in medium- to large-scale power generation. Figure 3.9 shows the performance characteristic of a typical axial gas turbine, developed in the same way as for a compressor in subsection 3.2.1. Each of the lines in the two graphs correspond to dimensionless speed lined in the turbine. In the top graph, the efficiency of the turbine is shown for different non-dimensional speed numbers as related to the pressure ratio of the turbine. The bottom graph shows the non-dimensional mass



**Figure 3.5:** An example of a compressor map for an axial compressor[39].

flow rate as a function of the same pressure ratio. As the pressure ratio increases, and the speed of the fluid entering the compressor approaches the speed of sound, the turbine becomes what is known as choked, and the dimensionless mass flow cannot increase further. This is clearly seen in the flat mass flow rate line in the graph.

The principles of energy transfer in a turbine are complex, but are chiefly governed by the equation of state, the conservation of energy, the momentum equation and the energy equation[39]. It can be shown[44] that the polytropic efficiency of the turbine can be written:

$$\eta_{t,p} = \frac{n-1}{n} \frac{\gamma}{\gamma-1}. \quad (3.5)$$

The relation between the real and isentropic efficiencies is analogous with the compressor, and written

$$\eta_{t,is} = \frac{\text{Isentropic work}}{\text{Actual work}} = \frac{\dot{W}_{cv}/\dot{m}}{(\dot{W}_{cv}/\dot{m})_{is}}. \quad (3.6)$$

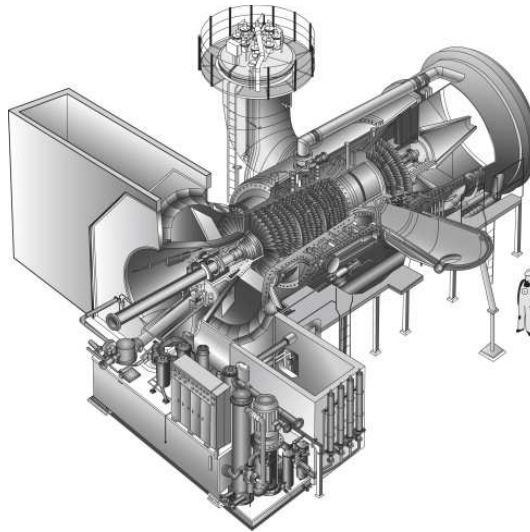


**Figure 3.6:** A gas turbine with side-mounted silo-type combustors[39].

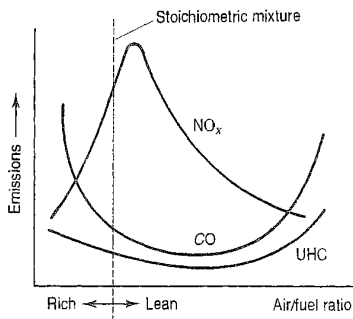


**Figure 3.7:** Emissions from a gas turbine depending on the fuel-air ratio (and temperature of combustion)[44].

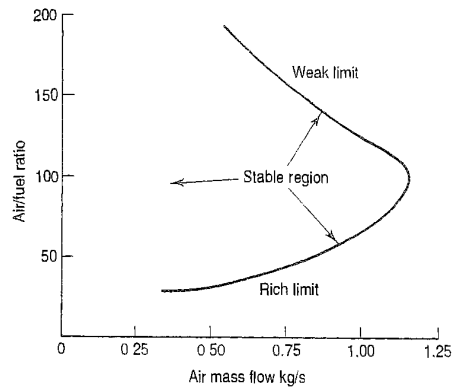


**Figure 3.8:** An example of the flame stability region in an annular combustion chamber[44].

As mentioned in section 2.3 in relation the Carnot efficiency, higher temperatures in heat engines allow for higher efficiencies, and it is therefore desirable to maximize firing temperatures in gas turbine systems. The limiting factor for temperatures in a gas turbine is the material limitations of the the gas turbine blades. In order to increase the firing temperature beyond the maximum temperature of the turbine blades, these may be cooled by a layer of air released through pores in the blade

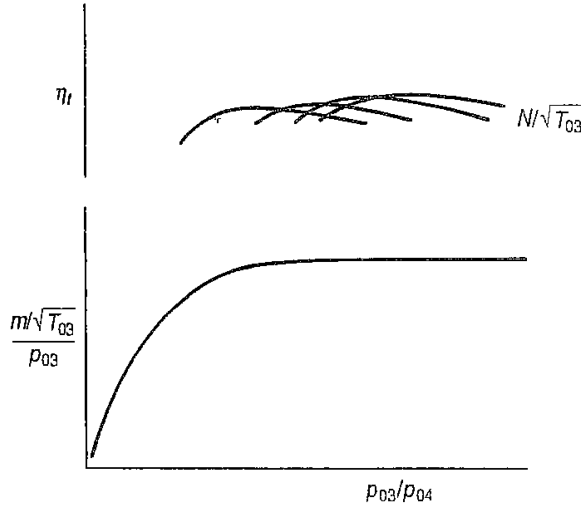


**Figure 3.9:** Performance characteristics of a natural gas turbine[44].

surface. A fraction of the compressor outlet air is diverted past the combustion chamber for this purpose, and allow for higher overall inlet temperatures into the gas turbine, without destroying the blades. In order to ensure a maximum turbine blade temperature of  $T_b$  by cooling the combustion chamber outlet gas of temperature  $T_{comb}$  using compressor air of temperature  $T_2$ , a the required fraction of air that must be diverted from the compressor,  $M_{cool}$  can be described by the following equation[17]:

$$M_{cool} = \frac{\dot{m}_{cool}}{\dot{m}_{comb}} = b \cdot \frac{c_{p,c}}{c_{p,g}} \left( \frac{T_{comb} - T_b}{T_b - T_2} \right), \quad (3.7)$$

where  $b$  is a proportionality constant, in this thesis taken to be 0.154 based on [17],  $c_{p,a}$  and  $c_{p,g}$  are the specific heats of the gases at the compressor exit and combustor outlet.

The efficiency of the gas turbine depends heavily on the turbine inlet temperature (TIT), which can be described as the mixing temperature of the hot gas from the combustor and the cooling air from the compressor. While this mixing temperature does not physically exist in the turbine, it can be used to describe the energy contained in the gas entering the expansion stage[46]. The temperature of the gas leaving the

combustor can be described by the following equation[39]:

$$T_{comb} = \frac{\dot{m}_a c_{p,a} T_a + \eta_{comb} \dot{m}_f LHV_f}{c_{p,g}(\dot{m}_f + \dot{m}_a)}, \quad (3.8)$$

where  $\dot{m}_a$  and  $\dot{m}_f$  are the mass flow rates of air and fuel into the compressor,  $c_{p,a}$  is the specific heat of the gas at the combustor inlet,  $T_a$  is the combustor air inlet temperature,  $\eta_{comb}$  is the combustion chamber efficiency and  $LHV_f$  is the lower heating value of the gas fuel - taking into account the latent heat of vaporization of the water in the gas, which is not recovered.

### 3.3 Solar Thermal Hybridization

The most obvious challenge for CSP power plants is the inconsistent access to solar irradiance throughout the day and the year. The stability and dispatchability that is derived from a combination with the higher efficiencies of a natural gas turbine therefore make a SHGT especially interesting for further study. In order to maintain stable high-temperature operation of a gas turbine, a combustion chamber can be added either in serial or in parallel with the solar thermal resource, as shown in Figure 3.11 and Figure 3.10. If the solar thermal resource is found to be sufficient to reach an appropriate turbine inlet temperature at design point, the combustion chamber can be integrated in parallel with the combustion chamber. Including a combustion chamber allows the plant to operate at 100% load around the clock, utilizing variable fractions of solar thermal power. Various strategies can be found for the integration of natural gas co-firing, including varying the load of the gas turbine to match the load of the power grid. A benefit with using the air Brayton cycle over the Rankine steam cycle usually favoured in CSP plants is a significant reduction in use of cooling water[41]. Due to the large temperatures in the exhaust of the gas turbine, it seems unlikely to construct a SHGT power plant without also considering integrating a bottoming cycle, although this may limit the plant's use as a dispatchable resource and reduce the savings in cooling water[47].

The principle of operation for a solar hybrid gas turbine is seemingly straightforward. Simply put, a simple Brayton cycle gas turbine power plant is integrated with a pre-heater between the compressor and the combustion chamber, in the form of the CRS CSP plant. Alternately, the combustion chamber can be replaced with heating from a solar receiver, but this is not currently practical with existing technology[40]. In order to reach higher efficiency in the plant, the system can be permanently co-fired with natural gas to reach an appropriate turbine inlet temperature at design point. In practice, the actual implementation of this design is not entirely as straightforward, as will be shown. Two important considerations that must also be taken in a design



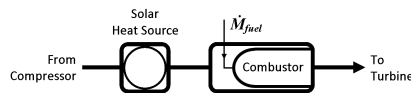
phase are the contradicting design parameters of a high solar share - the fraction of the energy generated that comes from sunlight - and the higher thermodynamic efficiency related to burning natural gas in all operational states, lessening the environmental gains[24].

Figure 3.12 shows the basic layout of a SHGT and Figure 3.13 shows the associated temperature-entropy diagram of the modified Brayton cycle. The gas turbine may either be co-located with the solar receiver in the tower, or, for larger systems, be located at ground level[48]. If the power block is not co-located with the receiver, some heat exchange between the cold compressor air and the heated return air will take place in the tower piping, and this effect is exaggerated and shown in Figure 3.13.

### 3.3.1 Component integration

Because of the relatively poor heat-transfer properties of air, both the tubular receiver - the simplest and most readily available receiver for a CRS system - or the atmospheric volumetric receivers described in chapter 2 would be poorly suited for this application. The system for absorbing the heat in the pressurized air case instead consists of pressurized volumetric receivers, as pictured in Figure 3.14. The pressurized volumetric receiver still relies on using a porous heat absorber material to capture heat from the incoming light as described previously, and shown in Figure 2.12, but must also withstand pressurization[14, 6].

In a pressurized receiver, the air is still passed through the solar heat absorbing material, which is now irradiated through a transparent window. Usually - as



**Figure 3.10:** The integration of a solar heat source in series with a fuel heat source[17].

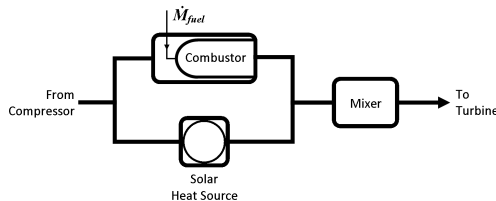


**Figure 3.11:** The integration of a solar heat source in parallel with a fuel heat source[17].

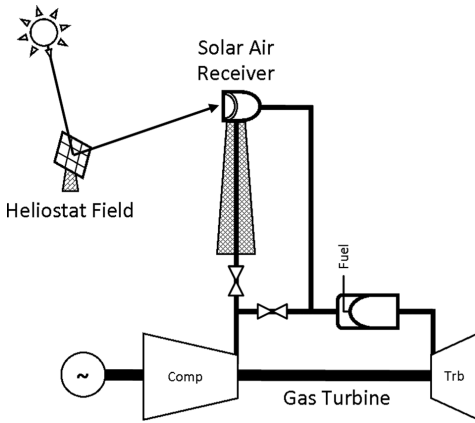


**Figure 3.12:** The basic layout of a solar hybrid gas turbine system[48].

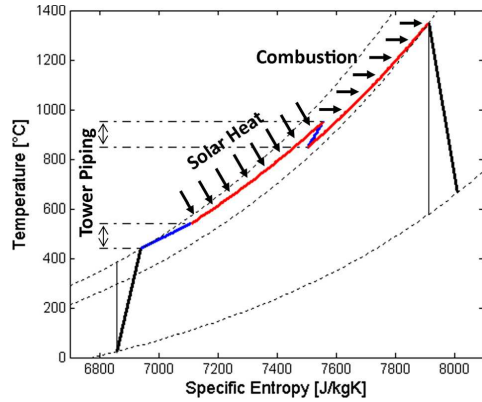


**Figure 3.13:** The temperature-entropy diagram of a solar hybrid gas turbine[48].

in the configuration pictured in Figure 3.14 - light is focused by a secondary concentrator as it is admitted into the receiver; in this case through a quartz dome window. The secondary concentrator can somewhat increase the receiver temperature, but also functions to reduce heat loss because of re-radiation is kept to a minimum. A silicon-silicon carbide ceramic foam, which is well suited to high temperature heat transfer application, can be used as the porous heat absorber material. This configuration of HTF and receiver is comparatively safe for operators and environmentally sound if seen in comparison to contemporary molten salt systems[40].

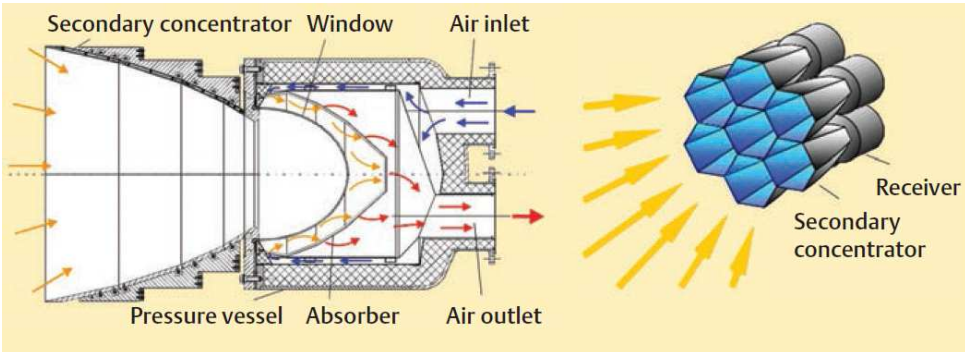


**Figure 3.14:** The layout of a pressurized volumetric receiver with a secondary concentrator, and a sub-assembly of such receivers[6].

Although temperatures up to 1200 °C are achievable in similar configurations[24], previous experience with cracking due to material defects in the quartz window currently limit the air outlet temperature of this receiver. Air exhaust temperatures up to 1000 °C with an operating pressure of 15 bar have been successfully demonstrated in such a receiver with a pressure drop of only 40 mbar in sustained operation[49, 40].

In a small-scale SHGT, the power block is usually co-located at the top of the solar receiver tower, and the air is ducted directly from the solar receiver to the combustion chamber with little intermediate piping[50]. In any larger, utility-scale SHGT plant however, it would be impractical to co-locate large gas turbines at the top of the central receiver, and the power block consisting of the compressor, combustion chamber, turbine and generator must be located at ground level. In such cases, the piping from the central receiver tower actually represents a larger temperature limitation than the receiver itself, as material limitations for uncooled metal piping and currently limit operating temperatures to 950 °C.[17]. The flow of pressurized air up and down the tower piping also represents a challenge and additional pressure losses. Figure 3.15 shows a solution for ducting of air between the gas turbine and the solar receiver. The heated air from the receiver is ducted inside the piping for the colder compressor air. The tower piping thus functions in practice like a heat exchanger between the compressor and combustion chamber pre-heated before entering the solar receiver. This is undesirable as it leads to lower efficiencies because the heat exchange leads to lower inlet temperatures to the combustion chamber, leading to higher fuel consumption. For this reason, the piping should be insulated, as shown. The alternative to this solution would be to pipe the hot and cold streams separately, but this would only lead to higher heat losses for the same amount of insulation[17].

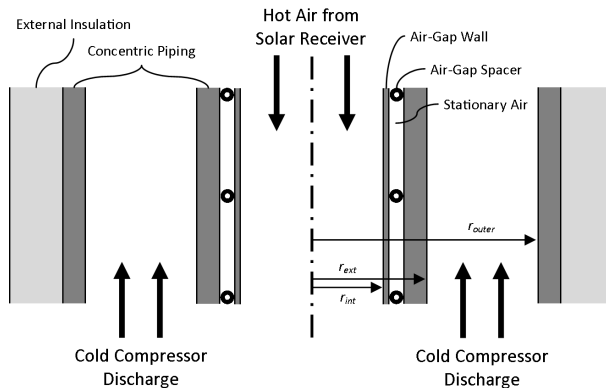


**Figure 3.15:** A solution for the piping between the power block and the solar receiver[17].

The integration of most currently available commercial gas turbines into a CRS plant as described in the previous subsection is currently not possible without extensive modifications. This relates to two major limitations. First, the high-pressure air that leaves the compressor must be extracted completely from the gas turbine in order for it to be heated in the solar receiver, and so only turbines which already has external ducting can be used without extensive modifications to the turbine casing, ducting and control systems[51]. Second, as the high-pressure and now high-temperature air returns to the gas turbine casing, its combustion chamber must be able to operate at a wide range of operating conditions. On the one hand it must be able to burn as in a conventional gas turbine when there is no solar resource available and for start-up of the system, but on the other hand will also potentially experience very lean fuel-air mixtures, and all the varying conditions inbetween. For these reasons, there are few commercial gas turbines currently available for direct integration into a SHGT power plant without major retrofits[52, 53].

In order to find suitable candidate turbines, recuperated gas turbines make good candidates, as they already have external ducting that can withstand high pressure and temperature, in order to extract all or most of the air leaving the compressor. An example of the layout of a recuperated gas turbine is given in Figure 3.16. The basic principle of recuperation is to utilize the waste heat that would otherwise be lost in an open Brayton cycle, by way of a gas-gas heat exchange to the air leaving the compressor. Recuperation is especially relevant for gas turbines operating with a low pressure ratio. For a SHGT the compressor outlet air must in any case be extracted from the casing, and recuperated turbines therefore are of interest[17]. In cases where the compression ratio may be limited by the solar receiver design, recuperation may also be of special relevance due to the lower possible energy extraction in the turbine, and therefore higher exhaust temperatures. The principle of recuperation is given in Figure 3.17, and its integration in a SHGT is shown in Figure 3.18.

As mentioned in subsection 3.2.2, the older, silo-type combustor technology may be most suitable for a SHGT, because there is a well-defined airflow from outside the gas turbine. An example of a turbine with air extraction from the compressor stage leading to an external silo-type combustor is shown in Figure 3.19. Turbines with externally mounted can-type combustors may also be relevant for the same reason. A benefit of having multiple can-type combustors is that they may be operated independently of each other, and so it is possible to operate the turbine using fewer combustors when the solar thermal energy available is high. The low fuel-air ratios in both of these cases, and the long residence time of the silo-type combustion chamber, represent additional challenges in terms of emissions. The principal mechanism for  $\text{NO}_x$  formation is the oxidation of nitrogen in air when exposed to high temperatures in the combustion process. The amount of  $\text{NO}_x$  is thus dependent on the temperature of the combustion gases and, to a lesser amount, on the time the nitrogen is exposed

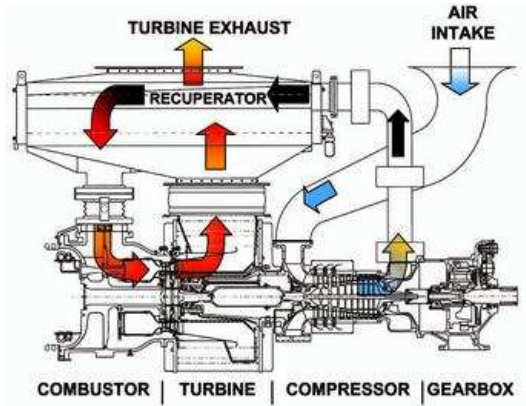


**Figure 3.16:** The Solar Turbines Mercury 50 recuperated gas turbine[54].

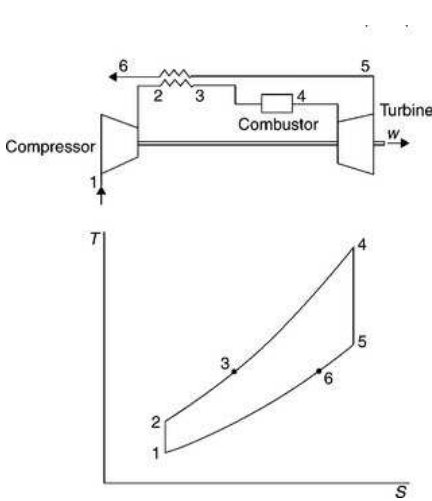


**Figure 3.17:** The recuperated Brayton cycle[55].

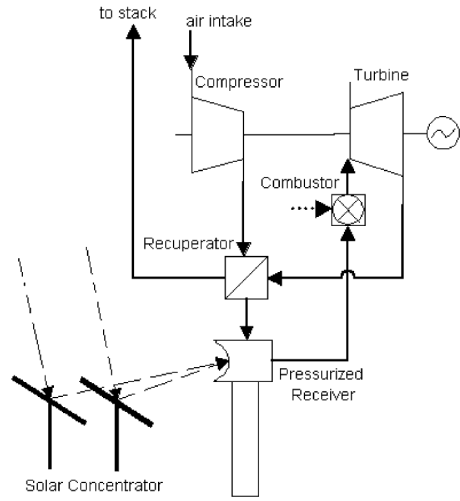


**Figure 3.18:** Recuperation in a SHGT system[56].

to these high temperatures - which is especially high in the silo type. In all cases, the challenges mentioned in subsection 3.2.2 associated with maintaining a stable flame in the combustion chamber for a wide range of operating conditions are also relevant[57, 58, 59].

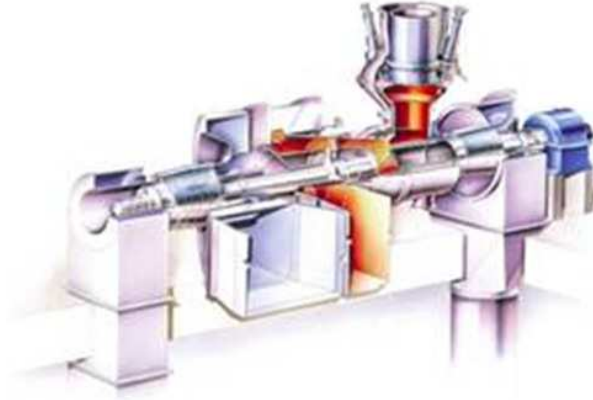


**Figure 3.19:** A gas turbine with air extraction for silo-type combustors[17].

### 3.3.2 Performance indicators

In order to study the performance of a SHGT plant and to compare it with other relevant technology, it is necessary to introduce a number of performance indicators, which are given in this section. These are compiled primarily from Spelling [17], as well as from Romero-Alvarez [24] and Olivenza-León [60].

The net electrical output,  $E_{net}$  of the plant is the total electrical power generated,  $E_{gen}$ , less the parasitic consumption of plant components,  $E_{par}$ , such as cooling fans, the additional compressor associated with charging of a thermal storage unit, and heliostat actuators if applicable:

$$E_{net} = \int_{year} (\dot{E}_{gen} - \dot{E}_{par}) dt. \quad (3.9)$$

The capacity factor,  $f_{cap}$  of the plant is the ratio of annual net electrical output to that which would be generated if the plant was operated at nameplate capacity (the nominal power output),  $E_{nom}$  continuously for an entire year,  $t_{year}$ :

$$f_{cap} = \frac{E_{net}}{\dot{E}_{nom} \cdot t_{year}}. \quad (3.10)$$

The thermodynamic efficiency,  $\eta_{th}$  of a power plant is defined as its net power output divided by the energy provided to it. In a SHGT plant, the provided energy is the sum of the lower heating value,  $LHV_f$ , of a mass flow  $M_f$  of fuel and the

instantaneous amount of direct solar radiation,  $I_b$  that is available for collection by a number  $N_H$  of heliostats with reflective area  $A_H$ :

$$\eta_{thermodynamic} = \frac{E_{net}}{\int_{year} (\dot{M}_f LHV_f + N_H A_H) dt}. \quad (3.11)$$

This definition of efficiency treats the two different sources of heat equally while summing them together. While this is not incorrect as a definition of efficiency, as it accounts for all losses, the two heat sources are different from each other: the sunlight must be collected, focused and converted to heat in the heat transfer fluid in order to be useful in this process, while the fuel heating value may be converted to heat directly with little losses, not accounting for its previous extraction, refining, processing and transportation losses. The energy provided by sunlight is also free of cost once the plant is built, and so while the thermodynamic efficiency of the plant would be increased by decreasing instantaneous direct solar radiation, such an increase would not be beneficial to operation of the plant due to both an increase in cost and emissions. Because of the cost of the fuel, Spelling [17] and others suggest considering only the fuel-electric efficiency of the plant, neglecting the solar input:

$$\eta_{fuel} = \frac{E_{net}}{\int_{year} \dot{M}_f LHV_f dt}. \quad (3.12)$$

The fuel-electric efficiency of the plant may be well above 100% when solar irradiance is high. Another common way to describe the efficiency of gas turbine power plants is the heat rate,  $HR$  - the heat added to the process from the fuel in order to generate one kilowatt-hour of electrical power - generally given in  $\text{kJ}_{th}/\text{kWh}_e$ :

$$HR = \frac{3600}{\eta_{fuel}}. \quad (3.13)$$

The two above formulae more accurately reflect the efficiency of the plant than the thermodynamic efficiency when considering the operating costs and carbon emissions of the plant and can as such aid in comparison to other plants. However, by neglecting the solar power input, an important part of the process is ignored. In order to more accurately compare the performance of the SHGT power plant to that of other plants, a useful way to describe its performance is to define the thermal efficiency specifically

as the net electrical output divided by the total heat which is added to the working fluid of the cycle in the solar receiver and combustion chamber:

$$\eta = \frac{E_{net}}{\int_{year} (\dot{M}_f LHV_f + \dot{Q}_{rec,eff}) dt}, \quad (3.14)$$

where  $\dot{Q}_{rec,eff}$  is the energy transferred to the heat transfer fluid in the central receiver. This thermal efficiency as defined will be used in chapter 7 to review and compare plant performance, and is as such simply denoted  $\eta$ . In this way, the heat added to the cycle from the sun is placed on "equal footing" with the heat added from the fuel, and the efficiency is also easier to relate to the solar share defined above. It should still be noted that this definition of efficiency does neglect the losses in the heliostat field and the receiver. These losses - being based on more recent technology than the rest of the gas turbine system - are worth study as they are expected to be the most cost-effective for improving performance in order to improve the thermodynamic efficiency of the plant[18]. For a more complete analysis of the losses in the plant described, an exergy analysis should be carried out, but this is considered to be outside the scope of this thesis.

Finally, an essential factor to consider utilizing renewable energy how much power actually comes from a renewable source. In a solar plant, this is the solar fraction,  $f_{solar}$  and is the amount of heat added to the working fluid from the solar source divided by the total amount of heat added to the working fluid:

$$f_{solar} = \frac{\int_{year} \dot{Q}_{rec,eff} dt}{\int_{year} (\dot{M}_f LHV_f + \dot{Q}_{rec,eff}) dt}. \quad (3.15)$$

### 3.3.3 Operational strategy

An immediately apparent strategy for a SHGT plant, with a gas turbine having an optimal efficiency at its design point, is to run the SHGT in base load configuration. An illustration of such an operating strategy is shown in Figure 3.20 for a plant co-fired with natural gas to reach higher efficiencies. The plant may be operated in this condition only when the solar resource is available to minimize fuel use and emissions, or its operation may be extended by running in gas-only mode when no solar thermal energy is available, reducing the total fraction of power generated from solar power annually. Figure 3.20 demonstrates quite clearly that 24-hour base load operation of such a plant requires a larger heat input from the fuel than that which is available from solar thermal power.



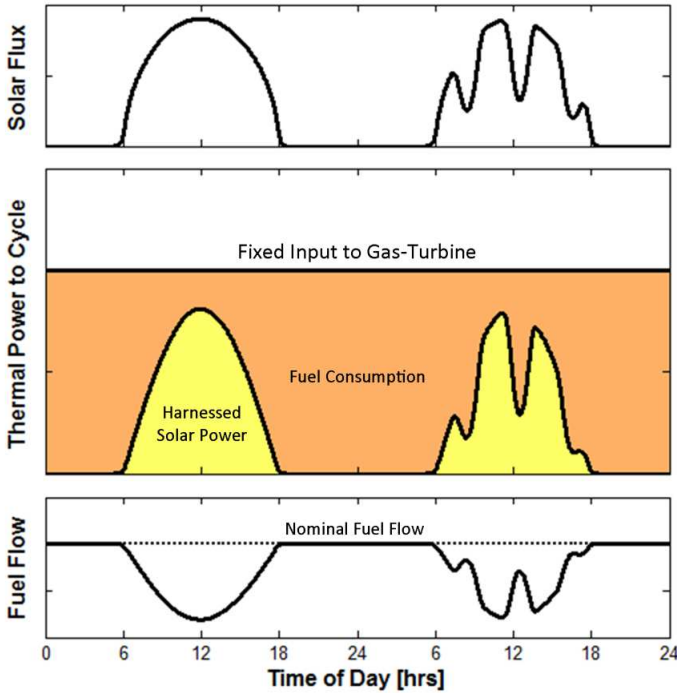


**Figure 3.20:** The operation strategy of a SHGT plant without storage as a base load power plant[17].

It is evident then that the benefit in terms of emissions reduction of such a plant is far less than for a solar-only plant of the same power generation capacity. Because of this, thermal energy storage is especially relevant for inclusion in SHGT plants, greatly extending solar operation. The base load operation of a plant with thermal storage is shown in Figure 3.21. In this figure, the SHGT plant has thermal storage and sufficient solar thermal heating to reach design point turbine inlet temperature at nominal conditions, and is therefore not co-fired when the solar resource is fully available. Once the storage is fully discharged, the combustion chamber may be operated to extend base load availability into 24-hour operation.

For plants with thermal storage, the solar multiple is normally also increased. In such cases, situations may occur on days with sustained high DNI where the storage is filled to capacity and there is an excess of solar thermal energy available. When this occurs, the heliostat field must be partially defocused by pointing some fraction of the heliostats away from central receiver. An amount of thermal power is thereby lost, shown as the grey area in the figure. Because of the high temperatures involved, both emergency blow-off valves in the system and fast-acting actuators on

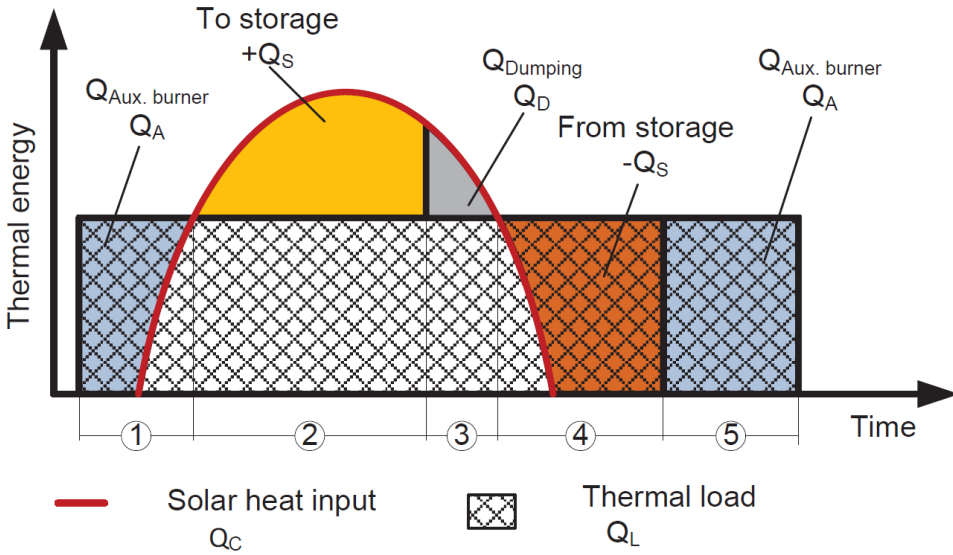


**Figure 3.21:** The operation strategy of a solar thermal power plant with a high solar multiple and thermal storage[61].

the heliostats for emergency defocusing are important in the SHGT plant[17].

In order to maximize both the thermal efficiency and solar fraction of a SHGT plant, the plant may be both permanently co-fired in order to reach higher turbine inlet temperatures, and integrating thermal storage in order to reduce the amount of fuel required. A plant combining these designs would be suitable as a less polluting base load plant, and also shows promising versatility in terms of operating at part load and following the load demand curve in the power grid as dispatchable power[18, 17].

Another option that is available for a SHGT is to act as a spinning reserve[17]. Renewables such as wind and solar are subject to large power fluctuations throughout the day, and all power plants in any case occasionally experience sudden outages. If power input is suddenly removed from the grid for one of these reasons or if a transmission line fails, the frequency of the grid will begin to fall. The remaining power plants have rotational inertia and are operating at synchronous speeds with the grid, so the drop in frequency is thus not instantaneous. Figure 3.22 shows the response required to deal with such a drop in frequency. Power plants that are able will immediately and automatically increase their power output to ensure that the frequency does not drop below acceptable limits. The frequency of the grid should however be stabilized within minutes by increasing the power production, and a

fast-acting power reserve must therefore be available until the slower base load plants in the grid can substantially ramp up production. Hydro power plants are the best suited for such fast-acting reserve duty. If hydro power is not available, an option is to maintain simple cycle gas turbines operational at full speed but without load. Another option is to operate flexible combined cycle power plants at below their rated capacity.

Clearly, both these options lead to substantial emissions in return for little or no power production. In fact, the emissions of operating spinning reserves may in large part offset those reduced by having a substantial amount of variable renewables in the grid[62]. A SHGT plant is important in this respect in two ways. First, by integrating a gas turbine to stabilize load, the variability in power output is greatly reduced, reducing the need for a spinning reserve. Second, a SHGT may be operated at little or no load using only solar thermal power, to be run at full load with the gas turbine when necessary. This maintains the rapid response times of a simple cycle gas turbine, but without the associated costs and emissions at no load[17]. The integration of thermal storage in the plant can extend such availability of the plant to around the clock.

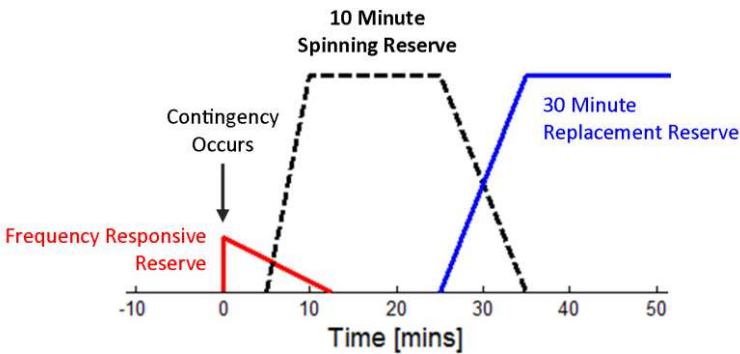
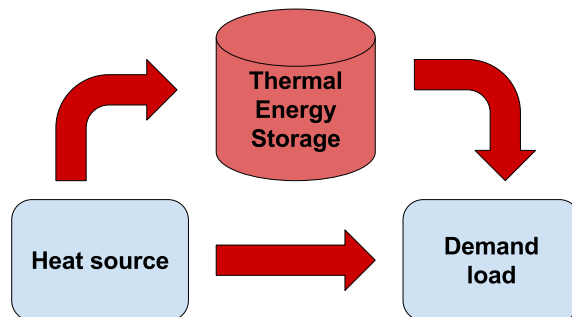


Figure 3.22: [17].

# Chapter 4

## Thermal Energy Storage

In cases where a system has a surplus or deficit of thermal energy available, it can be useful to store thermal energy in a way that allows this energy to be utilized later or in a more useful manner. The basic operating principle of thermal energy storage (TES) is illustrated in Figure 4.1: some fraction of the energy from a heat source is directed to storage, to be available for use in the demand load at a later time. This principle is also applicable for cooling applications, such as storing cold water or ice from winter in insulated container, in order to cool a building during summer. Different types of TES sorted by manner of operation are listed in Figure 4.2, and will be described in this chapter.



**Figure 4.1:** A schematic representation of the transfer of heat in a TES system. Adapted from [63].

Energy storage is especially relevant for CSP due to the highly variable nature of solar energy availability. The benefit of thermal storage in a CSP plant is the capacity to continue generating power after the sun has set and in cases of intermittent drops in DNI due to inclement weather or atmospheric effects, as well as affording flexibility for the plant to provide dispatchable power. This can be especially beneficial in cases where the power grid is more heavily loaded after sunset, or to compensate

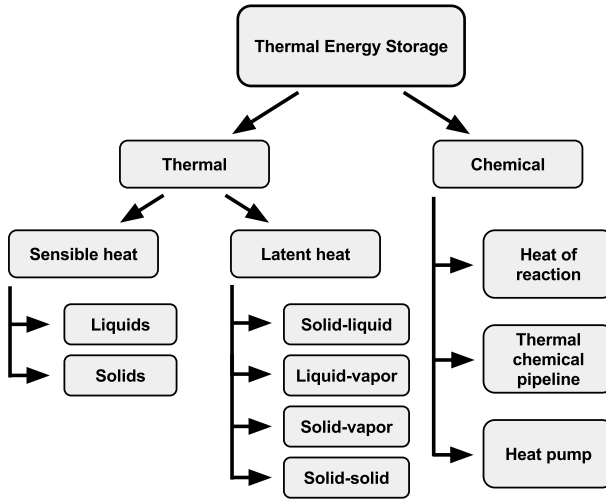


**Figure 4.2:** An overview of the different types of thermal storage available for solar energy. Adapted from [64].

for drop in power generation by other renewables which also have variable outputs. Figure 4.3 shows the power generation from a CSP plant where thermal energy is stored for an amount of time before power generation begins, in order to better match the demand from the power grid.

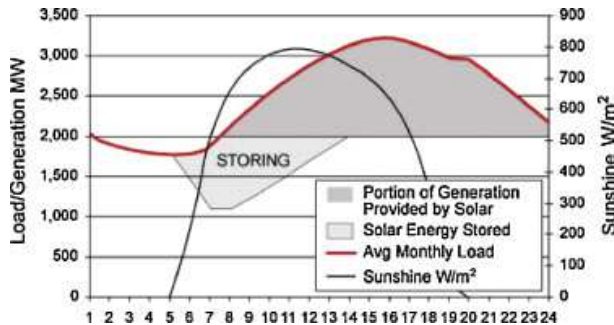


**Figure 4.3:** Shifting power generation until later in the day by way of thermal storage[65].

In a configuration with TES, the solar field collector area is generally increased beyond the design value of 1.10-1.15 mentioned in chapter 2, increasing the solar multiple of the plant. By doing this, it is possible to collect a surplus of heat in addition to generating power while the irradiance is high during the day. Increasing the solar multiple is not necessary, however, if the objective of integrating TES is

only to shift the electric power generation to later in the same 24-hour period. In CSP TES applications, the heat generated is most commonly stored in molten salts or mineral oils[22, 66]. While only around 40% of CSP plants built by 2011 had incorporated storage[67], nearly all CSP plants in planning or being built today integrate some form of TES systems[10].

Thermal storage can generally be categorized as either active or passive[63]. In active storage systems, the transfer of heat to and from storage is actively controlled by forced convection of heat into the storage medium, which is circulated to release heat to the demand load. The storage material is generally stored in one or more insulated tanks[66]. An example of a passive system can be the walls of a building retaining heat and gradually releasing that heat as the ambient temperature decreases, or the walls of a pipe retaining heat as a liquid passing through it cools. A further distinction is made between direct and indirect storage. Thermal energy can be stored directly in the relevant fluid of the system, in the case of CSP generally the HTF, or indirectly in another storage medium, which absorbs and releases heat from the working fluid through a heat exchanger. In CSP applications, an example of active indirect storage can be using solid storage media. Here the HTF passes through and charges/discharges a solid material, for example rock, concrete, castable materials or phase change materials. The storage material itself then does not circulate, but is charged when the HTF transports energy collected from the heat source into the storage medium, and vice versa discharged when colder HTF flows through it. Figure 4.4 summarizes the classifications of storage concepts, and Figure 4.5 gives an example of a power plant with active thermal storage.

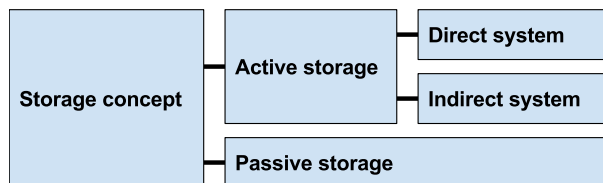


**Figure 4.4:** Different classifications of thermal energy storage. Adapted from [66].

When utilizing TES systems, important factors to account for in design are: energy density, the achievable duration of storage and characteristics of charging and discharging the storage [22]. Herrmann and Kearney[68] and Kuravi[28] have summarized the requirements for a TES system as such:

1. High energy density in the storage material
2. Good heat transfer between the heat transfer fluid (HTF) and the storage medium

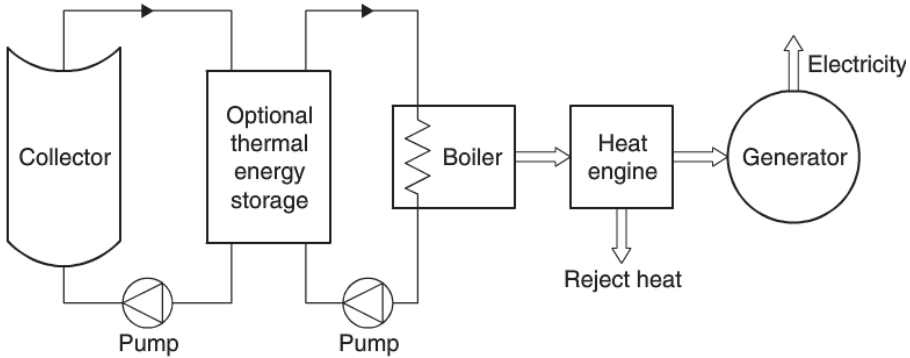


**Figure 4.5:** A schematic diagram of a CSP plant with integrated thermal storage[20].

3. Mechanical and chemical stability of the storage material
4. Chemical compatibility between HTF, heat exchanger, and storage medium
5. Complete reversibility for a large number of charging/discharging cycles
6. Low thermal losses
7. Low cost
8. Low environmental impact

#### 4.1 Sensible Heat Storage

It is apparent that by raising the temperature of a medium which does not undergo a phase change or chemical reaction, the amount of thermal energy in that medium will be increased. For a storage medium of mass  $m$ , with corresponding volume and density  $V$  and  $\rho$ , respectively, and with a specific heat  $c_p$ , an amount of energy,  $Q$ , can be stored in this mass as heat by raising its temperature from  $T_1$  to  $T_2$ [22]:

$$Q = \int_{T_1}^{T_2} \rho V c_p dT. \quad (4.1)$$

By insulating the container of the storage medium, energy is then stored and available for later release by lowering the temperature accordingly. Sensible heat can be stored in liquids such as water, mineral oils and synthetic oils, as well as molten

salts and in solids, such as rock beds, gravel or other packed material, as well as blocks, plates or otherwise solid materials.

#### 4.1.1 Liquid sensible storage media

Water is the most readily available and broadly used storage medium for low-temperature heat storage. In addition to being cheap and safe, it is well-suited as a thermal storage medium due to its high specific heat, but has less use in CSP applications due to its low boiling point. In CSP conditions, where higher temperatures are generally required, molten salts (most commonly in a binary mixture of  $\text{KNO}_3$  and  $\text{NaNO}_3$ ) are currently the most common and technologically mature storage medium[66]. The benefits of molten salts include favourable heat transfer and storage behaviour, and they are generally liquid at atmospheric pressure. Many molten salts are also available at low cost. Disadvantages of molten salts are the high cost of the surrounding system, large space requirements, as well as the need to maintain a thermal input or heat reserve in order to keep the salts from freezing in the pipes[69, 28].

Liquid storage media have the benefit of providing a thermal stratification naturally because of the differences in density between the hot and cold fluid, so long as the hot fluid is extracted from the upper part of storage, and the cold fluid is supplied to the lower part of the storage[28]. Stratification of the storage medium is desirable because it allows for extraction of higher temperatures, leading to better efficiencies in the power cycle of the plant. An example of a two-tank active direct thermal storage system is given in Figure 4.6. Here, the molten salt functions as the heat transfer medium, and is stored in a relatively cold tank, maintained at temperatures in excess of  $200\text{ }^\circ\text{C}$ , at the beginning of the day. It is then passed through the solar receiver, and stored in a hot tank. When power is required, it is then pumped to a heat exchanger, providing heat to the thermodynamic power cycle, before being pumped back into the cold tank. An overview of sensible liquid heat storage media is given in Table 4.1.

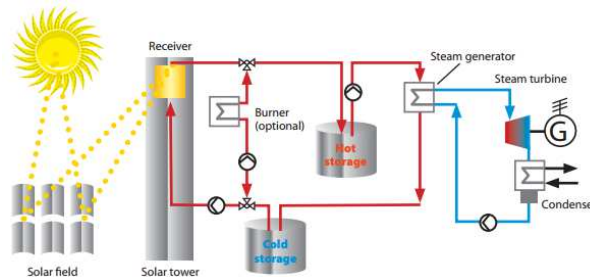


**Figure 4.6:** A two tank thermal storage system using molten salt as both the HTF and storage medium[70].



### 4.1.2 Solid sensible storage media

Storage of sensible thermal energy in solid media is normally done with indirect thermal storage. Common thermal storage materials are sand, rock, concrete - which may be mixed with other materials to improve its conductivity and heat capacity - and castable ceramics[22]. The material can for example be stored as a solid mass, a honeycomb structure or in a packed bed, depending on the application. A selection of solid thermal storage media with relevance for CSP application are listed in Table 4.2. Some advantages of solid storage are the lack of need for freeze protection, normally low cost, and high degrees of stratification, as well as the option of circulating air through the storage container[71]. Figure 4.7 shows an example of a packed bed of rocks, for example dug into the ground, and Figure 4.8 shows packed material with evenly distributed flow.

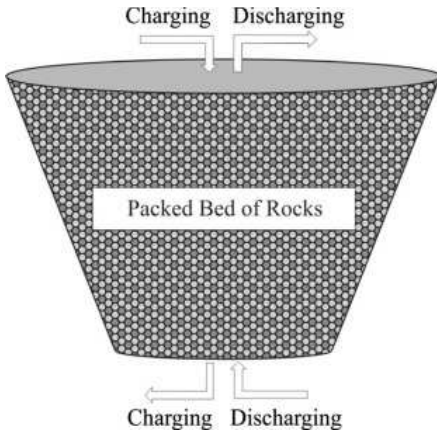


**Figure 4.7:** A container of rocks for thermal energy storage[73].

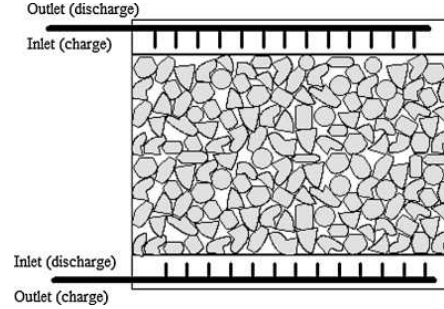


**Figure 4.8:** A packed bed of material with a flow distributor[63].

As shown in Equation 4.1, the amount of energy stored in sensible storage depends on the temperature range between the hot inlet temperature while charging and the cold inlet temperature while discharging. In a packed bed, the storage material is not solid throughout the storage tank, represented by a void factor  $\xi$ , equal to the fraction of the void volume in the container to the total container volume. For a nominal solar receiver output  $\dot{Q}_{rec}^{nom}$ , the volume of a solid packed bed thermal storage container then depends on desired storage duration  $t_{stor}$  as follows[17]:

$$V_{stor} = \frac{\dot{Q}_{rec}^{nom} \cdot t_{stor}}{(1 - \xi)\rho_s c_s (T_2 - T_1)}, \quad (4.2)$$

with  $\rho_s$  being the density and  $c_s$  being the specific heat capacity of the solid.

Unlike in liquid storage, where stratification occurs due to natural buoyancy because of temperature gradients, stratification occurs in solid storage due to the movement of the HTF through packed materials. Stratification is of key importance for CSP TES applications, as it allows the extraction of high temperature energy even when the storage is nearly empty[74]. Thermal radiation is low in packed material, as the media is non-transparent, and the packed material has small contact surfaces with neighbouring material. For such conditions, heat transfer can be treated as occurring only through convection in packed beds, and a well-defined heat differential develops, known as a thermocline[75]. The level of stratification thus depends heavily on the heat transfer coefficient of the storage medium, and in the abovementioned conditions, the thermocline remains well-defined even when the storage is neither being charged nor discharged. High levels of heat transfer mean that as the HTF flows from one side of the storage tank to the other, heat is deposited quickly, and a thermocline starts to form. Figure 4.9 shows different sizes of thermocline depending on the stratification in the medium. If stratification is strong enough that the thermocline is small compared to the size of the storage tank, it can be modelled as shown in Figure 4.10. Here, a thin level of perfect thermal insulation is imagined to move down the storage container, as if floating on a cold fluid, as hot fluid fills its upper part. Conversely, when being discharged, the insulation level moves up. This is analogous to the temperatures in a solid storage container with a well-defined thermocline.

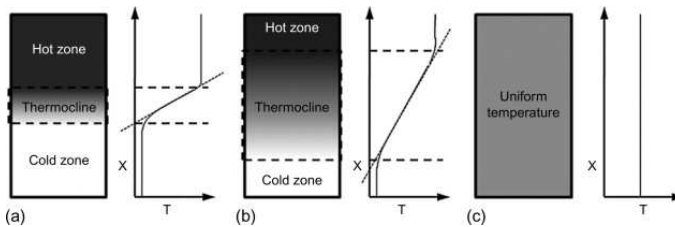


**Figure 4.9:** An illustration of a) highly stratified and b) moderately stratified thermal storage tanks, compared to c) uniform temperature, and their equivalent stored sensible energy[63].

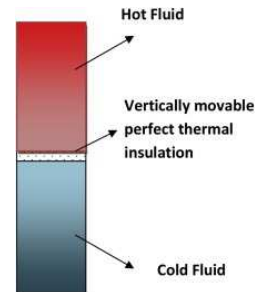


**Figure 4.10:** A model of a perfect thermocline. Adapted from[76].

Solid storage is less common in CSP plants utilizing molten salts as the HTF, but applicable for those utilizing oil or gas. For plants using air as the HTF, a packed bed of solid material shows the most promise as a regenerative pressurized high-temperature heat storage[77]. Figure 4.11 shows a pressurized vessel utilizing

this design, suitable for integration into a CSP plant. Magnesia fire bricks are a known material for high this purpose, and Klein et. al. [72] have found that alumina and zirconia are also suited as TES materials for temperatures up to 1000 °C. Of these two materials, the same authors found that alumina both has a higher storage capacity is therefore is better-suited as a storage material, and that it is approximately 40 times less expensive for such application than zirconia, although experience with either material is limited. Thermal wool or fibers can withstand temperatures of up to 980 °C, and are therefore the preferred material for high-temperature insulation of such a pressurized thermal storage vessel [17, 78].

Research is currently also being conducted into fluidized-bed technology, which shows promise for storing thermal energy in temperatures in excess of 800 °C[79]. In such a system, sand can be used as the HTF, and is transported into a hopper above the solar receiver, passed through the solar receiver as the HTF. It is then stored in an insulated container, to later provide energy to the power cycle through a heat exchanger. This method combines packed bed benefits with the benefits of active direct storage. Such storage methods are very low cost, environmentally friendly and safe, especially in comparison to molten salt technology, but require further research before being put into large-scale operation[66].

## 4.2 Latent Heat Storage

Because phase transformations in materials is an isothermal or nearly isothermal process, thermal energy may be stored at the temperature of the phase change, known as the transition temperature. The phase change may be solid-liquid, liquid-vapor, solid-vapor and solid-solid. Figure 4.12 shows the three stages involved when charging a phase change material (PCM). It is immediately apparent from this figure that for an equivalent temperature range, inclusion of latent storage allows for storage of a greater amount of thermal energy than with sensible energy storage alone. Conversely,

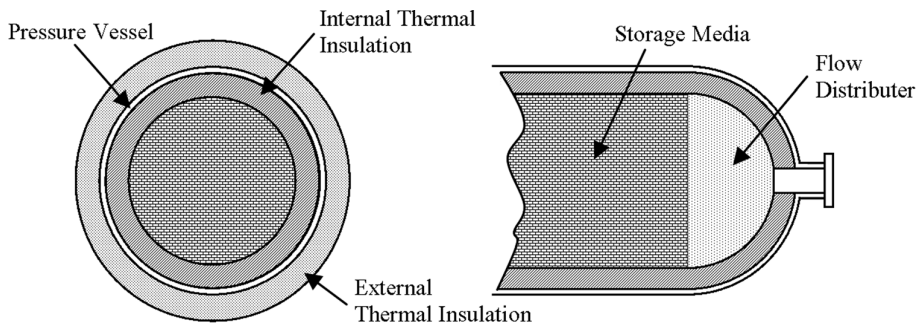


**Figure 4.11:** A pressurised vessel for regenerative high-temperature heat storage[25].

an equivalent amount of energy as in a sensible-only system may be stored with a smaller temperature range and higher energy density. With the exception of water/steam systems, PCMs have not yet been utilized in solar thermal applications, but the technology shows large potential for the field[28]. Figure 4.13 and Figure 4.14 show the integration of a PCM TES in a CSP plant for direct steam generation, and the associated T-s diagram for steam production. Heat exchangers placed before and after the storage block maximize heat transfer to the power block.

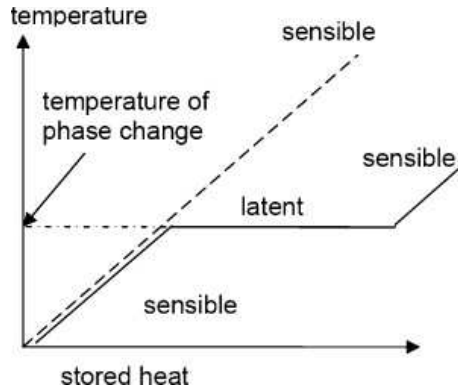


**Figure 4.12:** The process of storing and releasing heat with a phase change material[66].

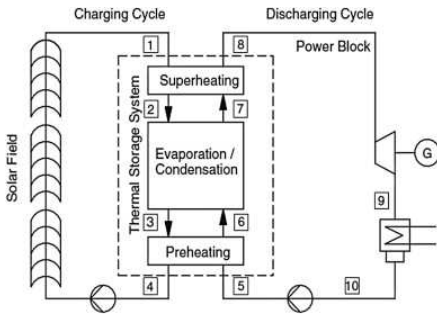


**Figure 4.13:** A simplified schematic of the integration of both sensible and latent heat storage in a steam generating plant[28].

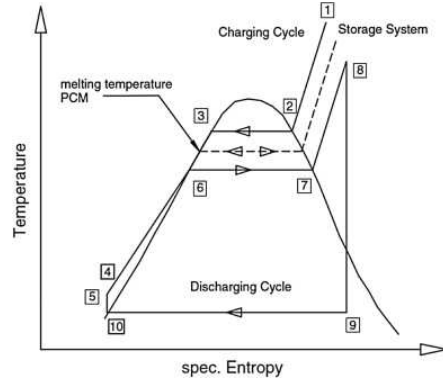


**Figure 4.14:** The T-s diagram for the power plant pictured[28].

The energy stored in a PCM, with  $T_m$  being the temperature at which the material undergoes phase transformation, and  $\lambda$  being the heat of the phase change, can be

written as[22]:

$$Q = \int_{T_1}^{T_m} mc_p dT + m\lambda + \int_{T_m}^{T_2} mc_p dT. \tag{4.3}$$

In addition to water/steam, which as previously mentioned has strictly limited temperature ranges, the most relevant PCMs for solar thermal applications undergo solid-liquid transformation. In such cases, Equation 4.3 can be simplified as[22]:

$$Q = m[\bar{c}_{p_s}(T_m - T_1) + \lambda + \bar{c}_{p_l}(T_2 - T_m)], \tag{4.4}$$

where  $\bar{c}_{p_s}$  and  $\bar{c}_{p_l}$  are the average specific heats of the material when solid and liquid, respectively. As shown in Figure 4.15, there are a wide range of families of PCMs. Many of these are commercially available, and a large amount of research is being conducted into investigating their properties[66]. One of many challenges related to these materials is the difficulty to maintain effective heat transfer regardless of material phase. One possible solution that is currently being researched for this is to encapsulate small castables of PCM in high-conductivity solid material, which allows the thermal storage material to be packed in a indirect storage unit as with solid sensible heat systems[64]. A small selection of solid-liquid PCMs are shown in Table 4.3. Because the technology is not currently considered mature for large-scale CSP application[28], latent heat storage will not be treated further in this thesis.

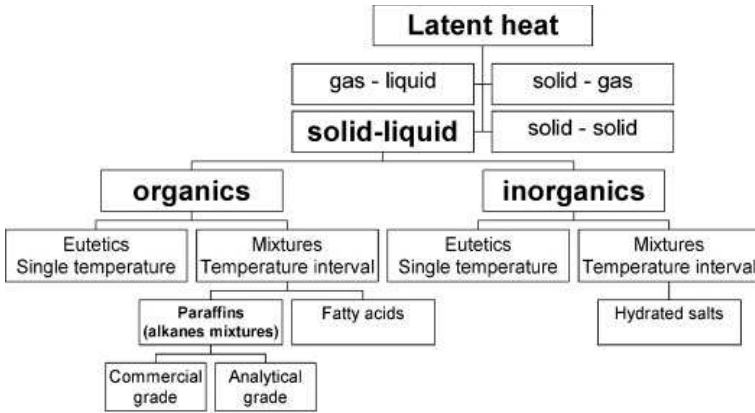


**Figure 4.15:** Classification of families of latent heat storage materials[66].

### 4.3 Thermochemical Energy Storage

Thermochemical storage systems denote a thermal storage system where a reversible chemical reaction is used to capture and store thermal energy. The storage of heat occurs during the endothermic part of the reaction, and energy is released exothermically. For a medium that fully dissociates in the temperature range of the solar receiver, this may store substantially more energy than with sensible or latent storage[81, 82]. For a general chemical equation[22]:



where a fraction  $a_r$  of the material has reacted, with a heat of reaction per unit mass  $\Delta H$ , then the energy stored in the material will be[22]:

$$Q = a_r m \Delta H. \quad (4.6)$$

Because some chemical reactions are so energetic, a very large amount of energy may be stored in a relatively small amount of material. Compared to this energy, the sensible thermal energy of the storage medium is small, and the energy may therefore be stored at room temperature for long periods with small losses, eliminating the need for insulation in the storage[22]. Challenges include reaction stability and completeness and reversibility, as well as integration into the solar thermal circuit. Despite its potential, thermochemical storage system technology is currently the least studied TES technology[28, 81]. While current technology levels theoretically make it possible to make use of thermochemical storage options in CSP plants, such use is currently rare[24, 3], and therefore will not be described further in this thesis.

Storage medium	Temperature range [°C]	Average density ( $\rho$ ) [kg/m <sup>3</sup> ]	Average thermal conductivity ( $k$ ) [W/m K]	Average specific heat ( $c$ ) [kJ/kg K]	Volumetric specific heat capacity ( $c\rho$ ) [kWh/m <sup>3</sup> ]	Media costs per mass (US\$/kg)	Media costs per energy stored (US\$/kWh)
Water	0 - 100	1000	0.63(at 38 °C)	4.19	116	-	-
Water (10 bar)	0 - 180	881	-	4.19	103	-	-
Mineral oil	200 - 300	770	0.12	2.6	55	0.3	4.2
Synthetic oil	250 - 350	900	0.11	2.3	57	3	43
Silicone oil	300 - 400	900	0.1	2.1	52	5	80
Nitrite salts	250 - 450	1825	0.57	1.5	152	1	12
Nitrate salts	265 - 565	1870	0.52	1.6	250	0.5	3.7
Carbonate salts	450 - 850	2100	2	1.8	430	2.4	11
Liquid sodium	270 - 530	850	71	1.3	80	2	21
Lithium liquid salt	180 - 1300	510	38.1	4.19	665		
Dowtherm A	15 - 400	867	0.1171 (at 155 °C)	2.2	204		
Therminol 66	0 - 345	750		2.1	151		

**Table 4.1:** An overview of liquid thermal storage media. Adapted from [22, 66, 28]

Storage medium	Temperature range [°C]	Average density ( $\rho$ ) [kg/m <sup>3</sup> ]	Average thermal conductivity $k$ [W/m K]	Average specific heat ( $c$ ) [kJ/kg K]	Volume specific heat capacity ( $c\rho$ ) [kWh/m <sup>3</sup> ]	Media costs per mass (US\$/kg)	Media costs per energy stored (US\$/kWh)
Sand-rock-mineral oil	200-300	1700	1	1.3	60	0.15	4.2
Reinforced concrete	200-400	2200	1.5	0.85	100	0.05	1
NaCl (solid)	200-500	2160	7	0.85	150	0.15	1.5
Cast iron	200-400	7200	37	0.56	160	1	32
Cast steel	200-700	7800	40	0.6	450	5	60
Silica fire bricks	200-700	1820	1.5	1	150	1	7
Magnesia fire bricks	200-1200	3000	5	1.15	600	2	6
Rock		1600	variable	0.88	390		
Alumina		3600	2.5	1.23	258		
Zirconia		5400	2.5	0.62	195		

**Table 4.2:** An overview of solid thermal storage media. Adapted from [22, 66, 28, 28, 72].



Temperature Range	Material	Transition Temperature	Heat of fusion
[°C]		[°C]	[kJ/kg]
0–100	Water	0	335
	Paraffin	20–60	140–280
	Salt hydrate	30–50	170–270
100–400	AlCl <sub>3</sub>	192	280
	LiNO <sub>3</sub>	250	370
	Na <sub>2</sub> O <sub>2</sub>	360	314
400–800	50LiOH/50LiF	427	512
	KClO <sub>4</sub>	527	1253
	LiH	699	2678
800–1500	LiF	868	932
	NaF	993	750
	MgF <sub>2</sub>	1271	936
	Si	1415	1654

**Table 4.3:** A selection of latent heat storage materials and their applicable temperature ranges. Adapted from [80]

Compound	Temperature	Reaction	$\Delta H$	$\Delta H$
	°C		[kJ/mol]	[GJ/m <sup>3</sup> ]
Manganese oxide	530 (at 1 bar of reactant)	$\text{MnO}_2 + \Delta H \longleftrightarrow 0.5\text{Mn}_2\text{O}_3 + 0.25\text{O}_2$	42	
Calcium hydroxide	505 (at 1 bar of reactant)	$\text{Ca(OH)}_2 + \Delta H \longleftrightarrow \text{CaO} + \text{H}_2\text{O}$	112	
Calcium carbonate	896 (at 1 bar of reactant)	$\text{CaCO}_3 + \Delta H \longleftrightarrow \text{CaO} + \text{CO}_2$	167	4.4
Magnesium hydride	250–500	$\text{MgH}_2 + \Delta H \longleftrightarrow \text{Mg} + \text{H}_2$	75	
Ammonia	400–500	$\text{NH}_3 + \Delta H \longleftrightarrow 1/2\text{N}_2 + 3/2\text{H}_2$	67	
Methane/Water	500–1000	$\text{CH}_4 + \text{H}_2\text{O} \longleftrightarrow \text{CO} + 3\text{H}_2$	n.a.	
Magnesium oxide	250–400	$\text{MgO} + \text{H}_2\text{O} \longleftrightarrow \text{Mg(OH)}_2$	81	3.3
Iron carbonate	180	$\text{FeCO}_3 \longleftrightarrow \text{FeO} + \text{CO}_2$		2.6
Metal hydride	200–300	$\text{Metal } x\text{H}_2 \longleftrightarrow \text{metal } y\text{H}_2 + (x - y)\text{H}_2$		4
Methanolation–demethanolation	200–250	$\text{CH}_3\text{OH} \longleftrightarrow \text{CO} + 2\text{H}_2$	n.a.	
Metal oxides (Zn and Fe)	2000–2500	e.g. 2-step water splitting using Fe <sub>3</sub> O <sub>4</sub> /FeO redox system	n.a.	
Aluminium ore alumina	2100–2300	n.a.	n.a.	

**Table 4.4:** A selection of thermochemical storage media, adapted from [28, 66]

# Chapter 5

## Bottoming Cycles

Thermodynamic cycles with applicability for power generation operate across known temperature ranges, limited by practical considerations such as material limitations. A selection of thermodynamic cycles is presented in Figure 5.1, showing the applicable practical temperature ranges the cycles are commonly operated across.

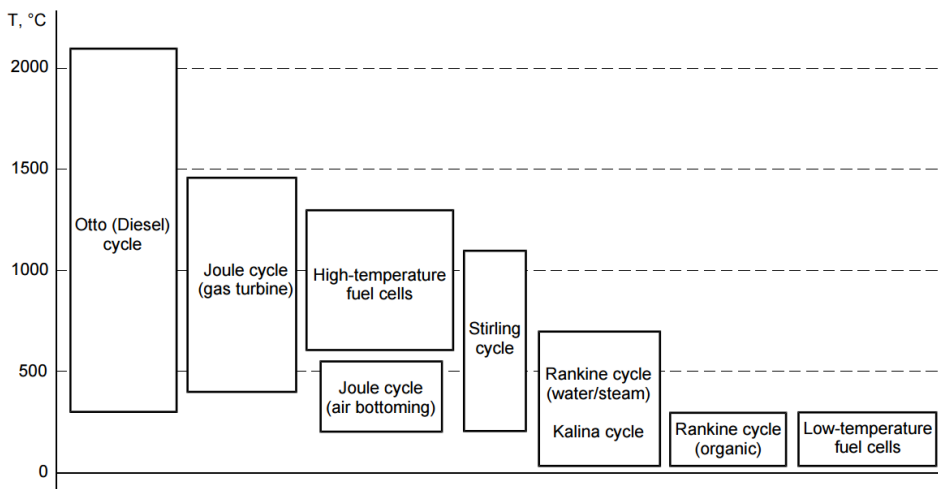


**Figure 5.1:** Thermodynamic cycles and applicable approximate respective temperature ranges[83].

In a gas turbine power plant, as is common with open thermodynamic cycles, the working fluid remains at a relatively high temperature as compared to the ambient conditions upon exiting the heat engine. By utilizing this temperature in another thermodynamic power cycle, the large energy contained in the exhaust may be utilized for additional power generation. This requires additional investment in equipment and maintenance, but is necessary in order to maximize the total

efficiency of the power plant. To differentiate between the two power cycles in such a combined-cycle power plant, the higher-temperature primary cycle is denoted the topping cycle, and the lower-temperature cycle is known as the bottoming cycle. The most common bottoming cycle in utility-scale gas turbine power plants is the Rankine steam cycle[59].

This chapter will outline four alternative bottoming cycles with applicability for improving power output from and efficiency of SHGT power plants. First, the steam Rankine and organic Rankine cycles are presented, as they are commonly available. Then, two cycles with special applicability for a SHGT plant are presented. It may also be noted that conventional steam CSP plants themselves show potential as a heat source the bottoming cycles of gas turbine power plants. This is known as the integrated solar combined cycle (ISCC)[84], but is considered outside the scope of this thesis.

## 5.1 The Steam Rankine Cycle

The steam Rankine cycle is the most commonly used cycle for utility-scale electric power generation in the world, as it is applicable for nearly any heat engine plants, for example those burning the fossil fuels coal or oil, as well as for nuclear fission plants. It is used as the primary or topping cycle in such plants, but is also the most commonly used cycle in combined-cycle gas turbine power plants[59]. The inclusion of the steam Rankine cycle as the bottoming cycle for a Brayton gas turbine topping cycle is shown in Figure 5.2, and the corresponding temperature-entropy diagram for an ideal steam Rankine cycle is shown in Figure 5.3. The cycle uses easily available water as a working fluid, which is heated, evaporated and optionally superheated by the plant's heat source, shown as the path 6-7 or 6-7' in the figure, and then expanded through a steam turbine to generate power. The steam is then passed through a condenser before being pumped back to the heat exchanger. The integration of a steam Rankine bottoming cycle in a SHGT plant, shown in Figure 5.4, is similar to as with a normal gas turbine.

A temperature-entropy diagram of a topping Brayton cycle and a bottoming Rankine cycle is shown in Figure 5.5. In order to utilize the energy in the gas turbine exhaust, it is passed through a heat recovery steam generator (HRSG), consisting of an economizer, evaporator and superheater. Because a high steam temperature is desirable, a water preheater may also be included before the economizer to optimize performance[59]. The temperature drop in the exhaust is shown as the path 4-1 in Figure 5.5, and the corresponding temperature increase and evaporation in the HRSG is shown as the path a-b-c-d. The temperatures of the two fluids through the HRSG is shown in Figure 5.6. The temperature difference between the exhaust gas as it leaves the evaporator and the saturation temperature of the steam is known

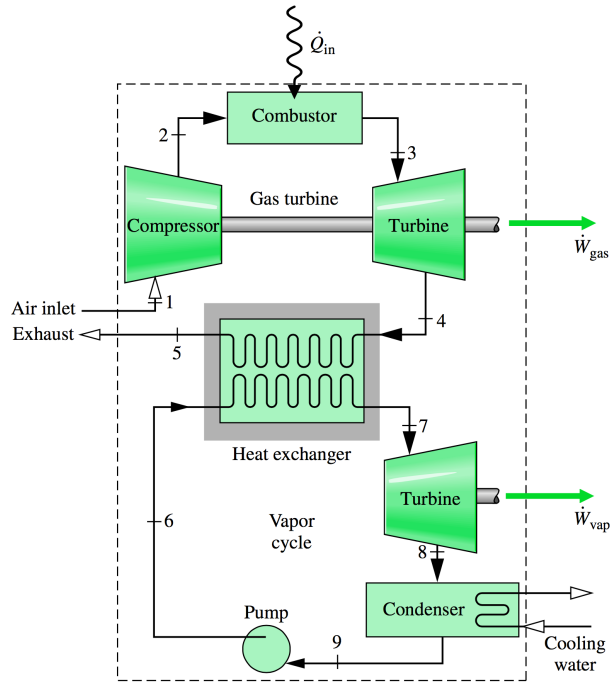


**Figure 5.2:** Integration of the steam Rankine bottoming cycle at the exhaust of a gas turbine[43].

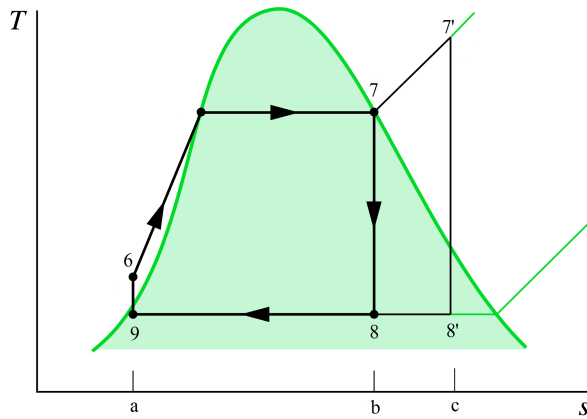


**Figure 5.3:** The T-s-Diagram of an ideal steam Rankine cycle[43].

as the pinch point in a HRSG. This is a limiting factor for heat recovery, as the temperature of the exhaust gas may not be lowered beyond the temperature of the

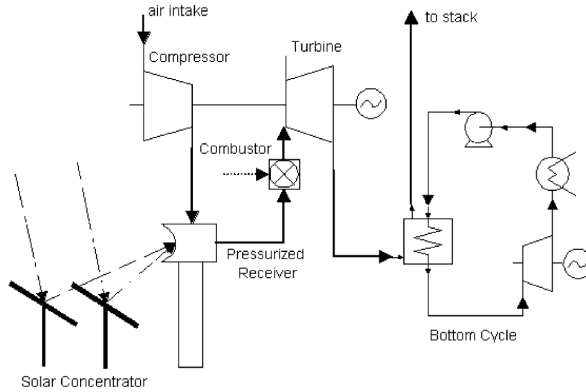


**Figure 5.4:** The integration of the steam Rankine bottoming cycle in a SHGT power plant[56].

steam saturation temperature in the evaporator. A small pinch point is desirable to maximize energy recovery, but reducing the pinch point requires larger heat exchanger surface areas, increasing both cost and backpressure on the topping cycle. In combined cycle power plants, the pinch point is commonly in the order of 10-20 °C, depending on economic considerations[39]. The temperature difference between the steam saturation temperature and the water entering the evaporator is known as the approach temperature. Some temperature difference is necessary to avoid evaporation in the economizer, but increasing the approach temperature leads to a larger required heat exchanger surface area, as with the pinch point. Approach temperatures are commonly in the order of 5-12 °C[39].

## 5.2 The Organic Rankine Cycle

Instead of water/steam, organic fluids with low boiling points are used as the working fluid in the organic Rankine Cycle (ORC). A variety of working fluids are available for use in the ORC, mostly as pure organic compounds, but also as mixtures. The cycle is well-developed for relatively low exhaust temperatures when compared to the steam cycle[86]. As shown in Figure 5.7, the principle of integrating the ORC components in a SHGT plant is analogue as with steam. Likewise the temperature-entropy diagram is similar to that for the steam Rankine cycle, but with some differences depending on the working fluid, as shown in Figure 5.8, classified by dry, wet and isentropic working fluids, depending on the slope of the saturation vapor curve in the T-s-diagram. A wet fluid shows a negative saturation curve, and will enter a two-phase state during expansion if not superheated significantly beforehand. Isentropic fluids have a vertical saturation curve, and dry fluids show a positive curve, and will be in a

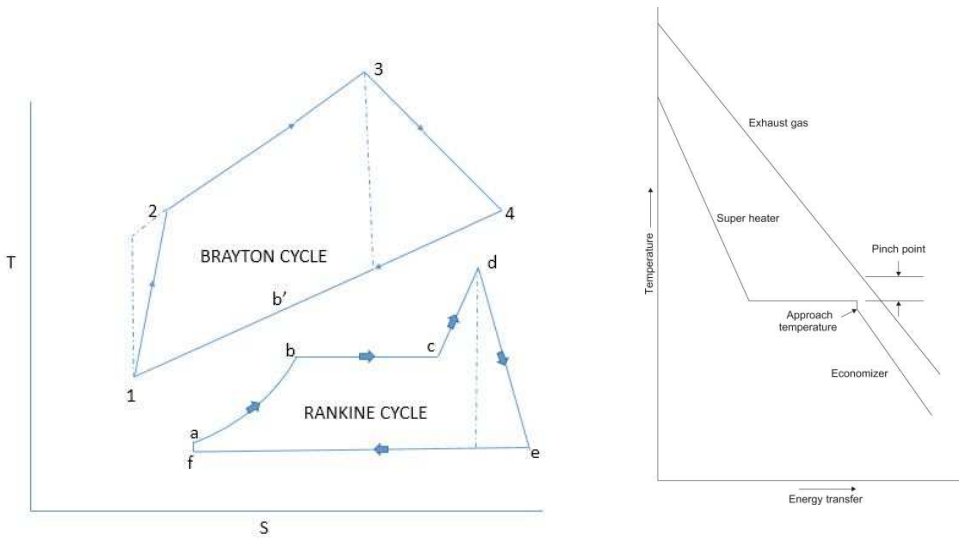


**Figure 5.5:** The T-s-Diagram of a topping Brayton and bottoming Rankine cycle[85].

**Figure 5.6:** Energy transfer between the topping and bottoming cycles[39].

superheated state after expansion. Isentropic and dry fluids generally give better thermal efficiencies in the cycle, as they do not condense in the expansion turbine[87].

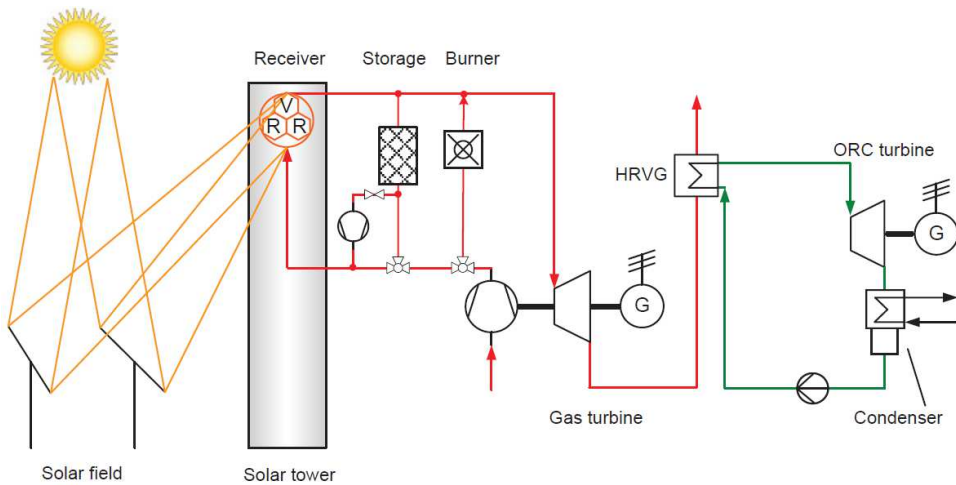


**Figure 5.7:** The integration of an organic Rankine cycle in a SHGT power plant[61].

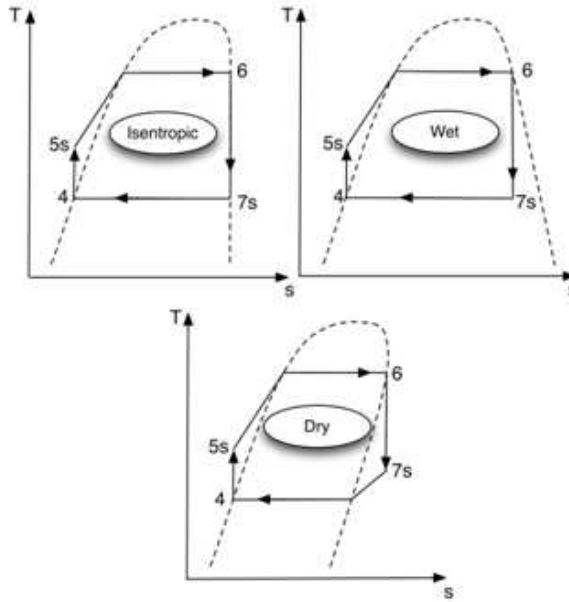


**Figure 5.8:** T-s-diagrams of different working fluids for the ORC[87].

The ORC working fluid should have low toxicity, corrosiveness, flammability and fouling characteristics, and good fluid stability performance. Some common organic working fluids are isobutane, toluene, and R11 refrigerant. It is common to use refrigerants, as working fluids, especially due to their low corrosiveness[87]. Because the exhaust gas temperature of a SHGT is commonly higher than the ORC range[61, 53], this cycle will not be studied in further detail in this thesis.

### 5.3 Air-Cooled Dual-Pressure Rankine Cycle

While maximizing performance is always relevant in utility scale power plants, water usage is of additional interest in solar thermal power plants. Because these plants must be located in sunny, hot, and therefore arid and water-scarce regions, water usage is of vital relevance in their operation for environmental and cost reasons. The air-cooled dual-pressure Rankine cycle proposed by Spelling et. al. [58], shown in Figure 5.9, is designed specifically for the SHGT topping cycle in order to both maximize heat recovery with a dual-pressure steam Rankine cycle and to lower water usage by integrating an indirect dry cooling system rather than conventional water cooling. Figure 5.10 shows the temperature-entropy diagram of the proposed cycle.

The addition of a vacuum deaerator, in order to remove oxygen and other dissolved gases from the feedwater, increases the heat recovery efficiency of the cycle. The

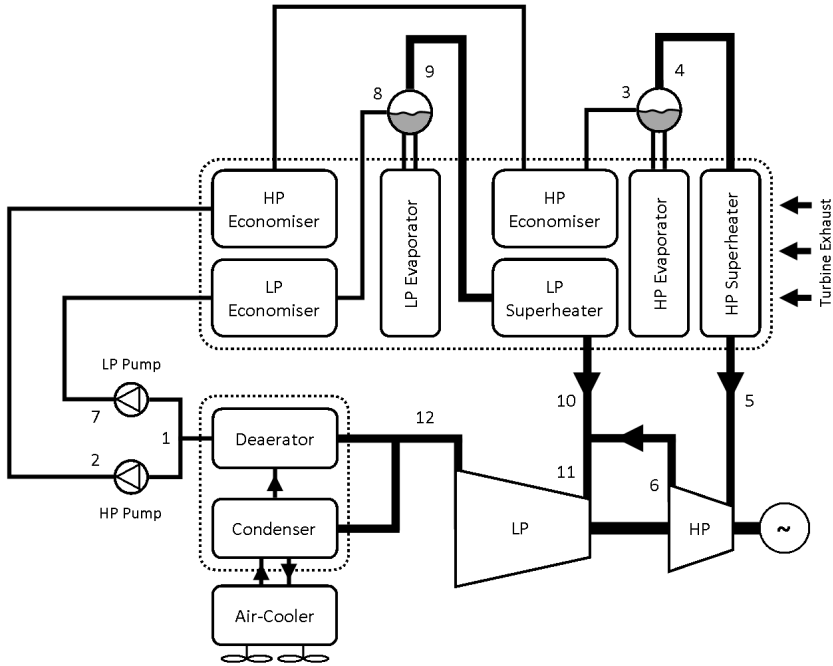


Figure 5.9: An air-cooled dual pressure steam Rankine bottoming cycle[58].

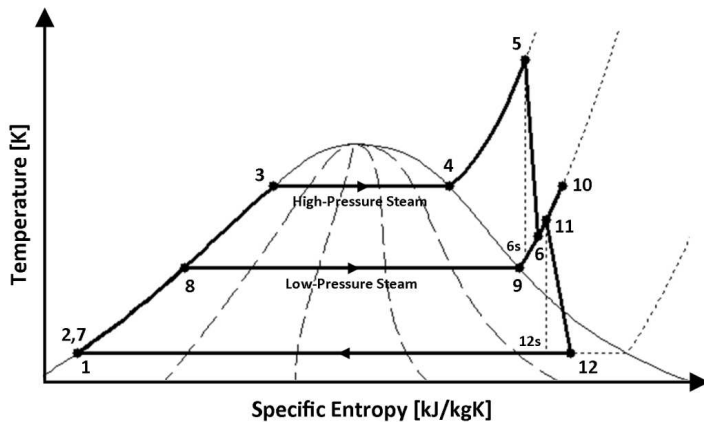
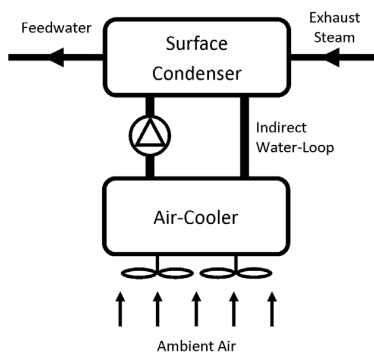


Figure 5.10: The T-s diagram of the dual pressure bottoming cycle[17].

dry cooling system is integrated as shown in the figure, and represents a loss in efficiency compared to a conventional evaporative cooling heat exchanger. However, cooling water usage is practically eliminated from the system, resulting in significant overall water usage reductions at the power plant. An indirect system, as shown in



Figure 5.11 is selected in the proposed design in order to minimize the back-pressure on the steam turbine. While a parasitic loss is involved in the pumping work of the water loop, the overall effect is to minimize the efficiency loss caused by higher condenser temperatures in this system[88].



**Figure 5.11:** The indirect air cooler needed to avoid cooling water[17].

#### 5.4 Air-Based Bottoming Cycle

One alternative to the Rankine cycle is the air bottoming cycle (ABC). Here, the Brayton cycle based on air is also used as a bottoming cycle through the use of a gas-gas heat exchanger rather. One or more intercoolers are integrated between compressor stages in order to make use of the relatively lower temperature of the exhaust gas from the topping cycle. Other working fluids may also be used in a closed Brayton cycle. Benefits of this cycle are the elimination of bulky equipment, leading to land use reduction, as well as the option of unmanned operation[86]. For CSP applications, ABCs are of additional relevance due to their potential for water-free operation. Sandoz et. al. [88] have proposed a ABC solution for SHGT power plants integrating three gas-gas heat exchangers as shown in Figure 5.12, as a way to eliminate water usage at a SHGT plant. A temperature-entropy diagram of such an air-bottoming solar hybrid gas turbine (AB-SHGT) is shown in Figure 5.13.

In the proposed layout, the bottoming cycle working fluid is compressed in two stages, with an air-cooled intercooler. Essentially, the functioning of the ABC is analogous to the conventional open air Brayton cycle, and operates based on the same principles described in chapter 3, with the addition of another compression stage and an intercooler[88]. The gas-gas intercooler used is of critical importance for the performance of the plant. The intercooler selected in this configuration is composed of finned tubes connected to a header manifold, as proposed for the LMS-100 intercooled gas turbine integrating[89].

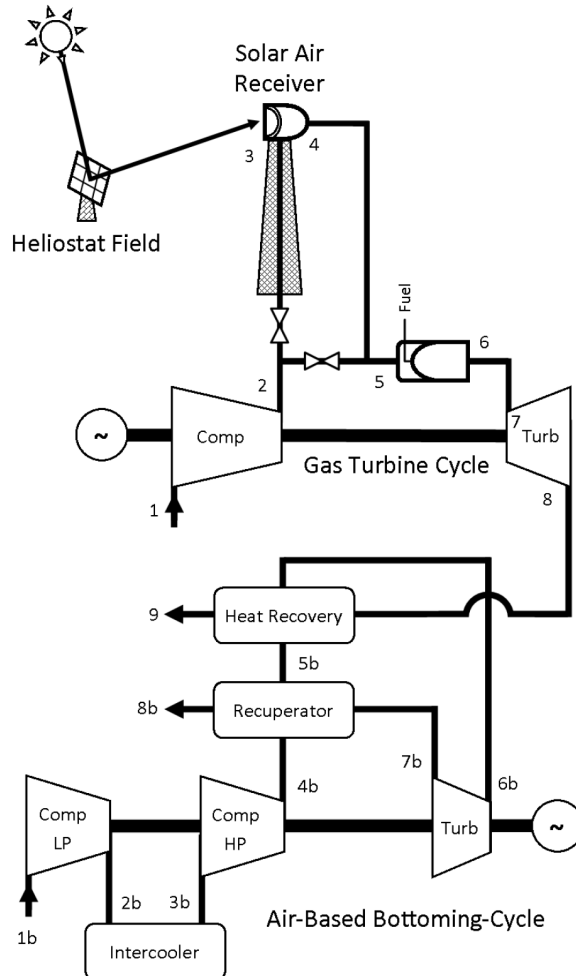


**Figure 5.12:** The integration of an air-based bottoming cycle in a SHGT power plant[88].

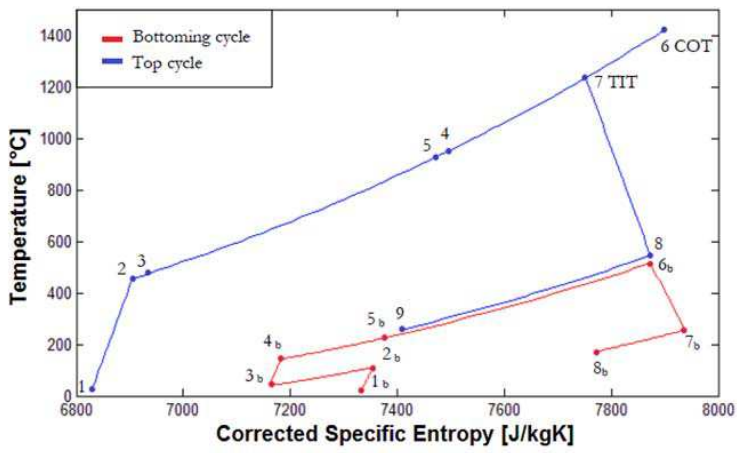


Figure 5.13: A T-s-diagram of the air-bottoming SHGT plant proposed[88].

# Chapter 6

## Simulation Background and Assumptions

The solar engineer Soteris Kalogirou [20] summarizes the benefits of simulating power plants as such: The cost of simulating is very low when compared to prototyping, and the simulation may organize complex systems and information. This leads to a chance to gain deep understanding of the parts, operation and interactions in a system, and to find decent estimates both for the cost of and energy delivered by a power plant. Further, a simulation may be subjected to a wide variety of different types of weather, operating situations and conditions.

The simulations in this thesis have been carried out using the energy and power plant process simulation program EBSILON® Professional[90], developed by STEAG Energy Services GmbH and hereafter referred to as Ebsilon. This program is developed especially for the thermodynamic cycles in power plants, and has recently added functionality for plants integrating solar thermal power.

Ebsilon uses a graphical user interface (GUI) to allow users to create simulation models of various systems. Simulations are carried out at steady state as follows: First, each component in the simulation is called, collecting the user input data and arraying this in a matrix containing the relevant formulae for all components in the model, such as mass and energy balances. This system of equations is then solved in repeated iterations, until they reach convergence, and results for all components are available to the user in the GUI or may be exported in a spreadsheet[90].

Steady state simulations are appropriate for the simulation of conventional utility scale power plants, especially those operating at relatively stable conditions, such as many coal or natural gas turbine power plants. While it is useful to also simulate solar thermal power plants in such a manner, they are always subjected to rapidly changing irradiance throughout the day, and their operating conditions therefore change rapidly and repeatedly. Due to these changes, there are often transient dynamic situations in the plant, and the response of a CSP plant to changes in DNI is generally non-linear[18]. To compensate for this, one solution could be to simulate

the rapidly changing situations dynamically. This would add a lot of complexity to the problem, and would require an additional program, as Ebsilon's calculations are in any case only valid for steady state situations. To remedy this situation, we may compensate by making our system quasi-dynamic, or quasi-steady state, by re-calculating frequently.

Ebsilon does accommodate for quasi-dynamic simulations for dynamic situations through the use of time series. By providing data for each time step, a series of steady-state calculations can be carried out at a time scale of the user's choosing. Best results would be gained with data on a one-minute time scale[18], but this would make for very time consuming calculations, and access to reliable data on such a fine time scale is limited. As a compromise, the calculations of the power plant in this thesis have been performed for every 15 minutes of the simulated period.

The program also helpfully distinguishes between the design and off-design performance of its components. By setting parameters for the design performance of components at nominal conditions and by providing equations or characteristic curves of different component performance, the user may simulate response to a wide variety of situations for the components in a simulation. This is especially relevant for the solar thermal power plants, as highly variable irradiance rates mean that the plant is rarely, if ever, operating at its design condition.

## 6.1 Localization

Before design and simulation of a CSP plant can take place, one or more potential locations must be selected, and relevant environmental data collected. For this thesis, potential sites have been limited to Europe. Seen as a whole, there are fairly limited potential locations for CSP in Europe. With current technology, a typical minimum irradiation requirement for DNI at a potential site is at least 1,900-2,100 kWh/m<sup>2</sup> per year. While CSP plants are theoretically feasible below this level, PV systems, which can make use of both direct and diffuse irradiance, are considered more advantageous in such conditions[3, 92]. As Figure 6.1 shows, the majority of continental Europe already does not fulfil this minimum requirement for DNI, and can be immediately ruled out as potential sites for a CSP plant. The countries in Europe that do show promise based on available DNI are primarily in Spain, Portugal, France, Italy and Greece.

It is also clear that the building of a power plant is most reasonable in proximity to a power grid which has sufficient demand for electricity. Because of this, the smaller islands in the Mediterranean are ruled out as candidate locations despite potentially favourable solar conditions. Furthermore, building of large-scale CSP plants generally require large surface areas in locations with stable cloud-free weather year-round,

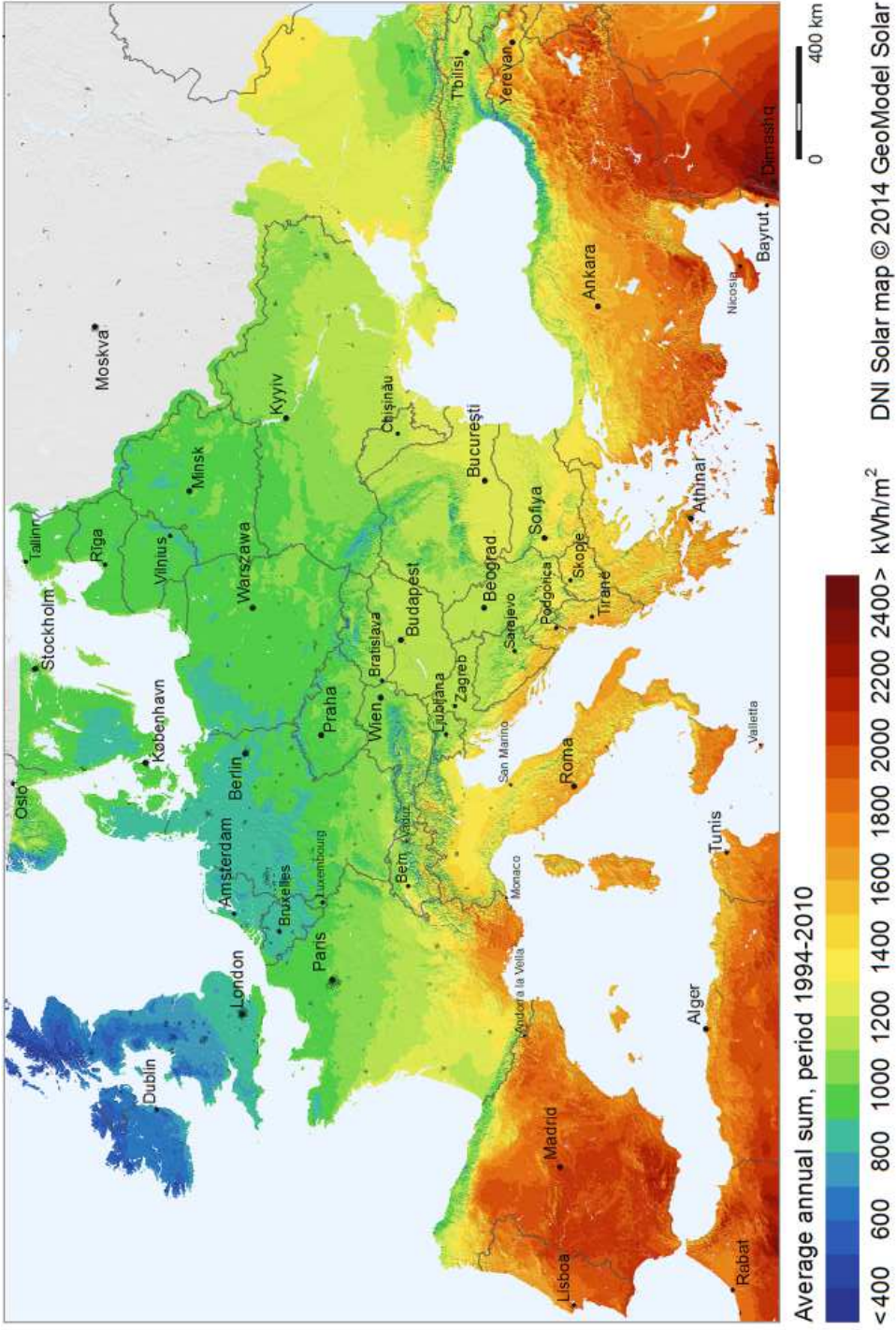
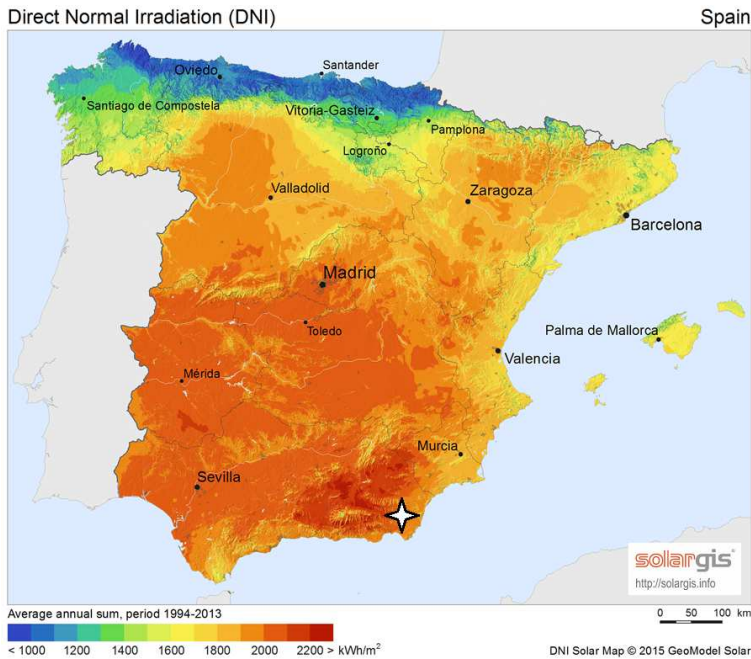


Figure 6.1: A map of average annual DNI in Europe, Courtesy of SolarGIS[91], ©2015 GeoModel Solar

little to no atmospheric haze or smog, and to be located in a relatively flat region, with few nearby hills or mountains to block sunlight. Based on the above criteria, a number of sites can be considered suitable. These sites are chiefly in Spain, Italy and Greece, which all have deserts or desert-like regions, where DNI conditions are stable throughout the day, with little weather or atmospheric interference. Because the goal of this thesis is to make a detailed process model of a power plant, there is a need for reliable data on both solar radiation and other weather conditions. Based on this need, a site has been selected in the Tabernas Desert in the Spanish province of Almería. This location fulfils all the criteria mentioned above, and it is also the location of the Plataforma Solar de Almería (PSA), a solar energy research facility run by the public research organization Centro de Investigaciones Energéticas, Medioambientales y Tecnológicas (CIEMAT)[93]. For this reason, sub-hourly DNI and weather data is available for the site dating back many years. The location of the power plant simulated in this report is marked with a star in Figure 6.2.



**Figure 6.2:** DNI map of Spain with plant location. Map courtesy of SolarGIS[91], ©2015 GeoModel Solar

The DNI values at this location are very briefly summarized in Appendix D.

## 6.2 Ambient Conditions

The ambient conditions of the power plant are decided by its now decided location:

- Latitude: 37.094400
- Longitude: -2.358200
- Elevation: 499.0 m a.s.l.

The boundary conditions in common for all simulations in this thesis are given in Table 6.1. The variable data is taken from the data set[94].

	Value	Unit
Direct normal irradiance (DNI)	Variable	[W/m <sup>2</sup> ]
Ambient temperature	Variable	[°C]
Sun azimuth relative to North	Variable	[°]
Sun elevation relative to horizon	Variable	[°]
Atmospheric pressure	1,013	[bar]
Air humidity	60	[%]
Cooling water temperature	15	[°C]
Cooling water pressure	2	[bar]
Electrical power grid frequency	50	[Hz]
Co-firing fuel	CH <sub>4</sub>	[ - ]
Fuel lower heating value (LHV)	50015	[ kJ/kg ]
Fuel temperature	5	[°C]

**Table 6.1:** Boundary conditions used in the process models

The dataset contains measured or calculated values every 15 minutes from January 01st, 1994 until June 30th, 2012 for these values. The values are based on measurements taken by satellite, observations on the ground, weather forecasts and calculations by a Geographical Information System (GIS). Because simulation of a full year of plant operation at 15 minute intervals would take a very large amount of time, only a single year’s worth of data has been imported into the simulation. Based on a study on inter-annual variability in solar irradiance values at Plataforma Solar de Almería (PSA)[95], the year with the lowest deviation from average DNI values in recent years was found to be 2007, and this was therefore selected for simulation.

It is common to consider the design point of a CSP plant at solar noon on the spring or fall equinox, as the sun is at its absolute highest in the sky at any



point in the year at this time. A direct normal irradiance value of  $850 \text{ W/m}^2$  is commonly used[17]. Sun angles at the design condition are taken from [96]. ISO conditions[97] are normally used in gas turbine simulations, and these are taken as ambient conditions with the exception of temperature. While the ISO standard temperature for gas turbines is  $15 \text{ }^\circ\text{C}$ , this is not a realistic temperature for a plant exposed to  $850 \text{ W/m}^2$  of DNI. Instead, a temperature of  $25 \text{ }^\circ\text{C}$  has been selected as the design point ambient temperature, to more accurately represent the plant's desert conditions. The design point boundary conditions are given in Table 6.2.

	Value	Unit
Direct normal irradiance (DNI)	850	$[\text{W/m}^2]$
Ambient temperature	25	$[\text{ }^\circ\text{C}]$
Sun azimuth relative to North	180	$[\text{ }^\circ]$
Sun elevation relative to horizon	52.9	$[\text{ }^\circ]$

**Table 6.2:** Ambient conditions of the design point in the process models

### 6.3 Power Plant Design Decisions

As stated in the problem description for this thesis, the primary motivation for the integration of a co-fired gas turbine in a solar thermal power plant is to achieve higher efficiency by raising the turbine inlet temperature. Higher efficiency is also achieved by inclusion of a bottoming cycle, which requires relatively stable conditions. For this reason, the plant will be designed as a base load power plant. Based on current developments, it is likely that most CRS power plants emerging in the near future will be in the output range of at least 50-100  $\text{MW}_e$ [14]. Therefore, the electric power output of the topping cycle for this plant is set to  $100 \text{ MW}_e$ , with the goal of evaluating it for baseload power production in a combined cycle configuration. Further, in order to minimize water usage, an air-cooled air-bottoming cycle has been chosen as the bottoming cycle.

The design methodology can be summarized as follows:

- A high firing temperature has been selected with the goal of improved thermodynamic efficiency.
- In order to minimize emissions, a high solar share has been used as a motivation for further design decisions.
- Due to arid conditions at the plant location, processes utilizing water have been minimized.

- Excess thermal energy is utilized in a bottoming cycle in order to improve efficiency.

## 6.4 General and Component Assumptions

A large number of further assumptions have been made in the making of the process models in this chapter, and will be presented in this section. General limiting background assumptions are as follows:

- Transient effects of start-up and shut down are neglected, as all simulations are carried out at steady-state.
- The effects of wear and tear and maintenance requirements, such as the need for heliostat cleaning and plant maintenance downtime, are not considered.
- Individual component nominal pressure drops are estimated based on literature rather than calculated.
- Combustion is assumed to be fully stoichiometric and flame stability and gas turbine turndown performance are not studied.
- Instead of considering the exact blocking by geography near the plant, incoming solar irradiance is neglected for solar elevation angles of below  $5^\circ$  above the theoretical horizon.

A summary of component assumptions at nominal plant performance is presented in Table 6.3. The reasoning and relevant sources for these is given in the following subsections.

### 6.4.1 Conventional Gas Turbine Components

As detailed in subsection 3.3.1 very few gas turbines are immediately suited for use in SHGT due to the need for air extraction and burner design[52, 17]. A theoretical gas turbine based on individual components will therefore be considered in simulations. The first design decision is the combustion chamber exhaust temperature. This is set to  $1400^\circ\text{C}$ , based on material limitations of cooled turbines[46, 45, 98]. The compression ratio of the gas turbine is limited by the solar receiver, as will be described in subsection 6.4.3. Based on the firing temperature and compression ratio, the compressor, combustion chamber and turbine efficiencies are decided based on a state-of-the-art review by Bhargava et. al. [47]. Electric generator efficiency is

---

<sup>1</sup>The accuracy of the heliostat field efficiency is limited, as discussed in subsection 6.4.2

	Value	Unit
Heliostat field total efficiency <sup>1</sup>	46.9	[%]
Solar receiver optical efficiency	93	[%]
Solar receiver total thermal efficiency	70	[%]
Thermal energy storage round-trip efficiency	90	[%]
Compressor polytropic efficiency	90	[%]
Combustion chamber thermal efficiency	99	[%]
Turbine isentropic efficiency	89	[%]
Rotating machinery mechanical efficiency	99	[%]
Generator efficiency	98.6	[%]
Gas inlet and exhaust pressure drops[46]	10	[mbar]
Central tower piping pressure drop	100	[mbar]
Solar receiver pressure drop	50	[mbar]
Combustion chamber pressure drop	500	[mbar]
Air-air gas exchanger pressure drop	2	[%]

**Table 6.3:** Assumptions used in the process simulation

assumed to be 98.5%. As the plant will be designed for base load operation, its turndown limits will not be examined.

An external silo-type combustion chamber will be assumed. Combustion is assumed to be stoichiometric and the fuel used is pure methane natural gas,  $\text{CH}_4$ , using the default LHV provided by Ebsilon. The nominal combustion chamber pressure loss is assumed to be 0.5 bar at the design point, based on [17, 99]. Because a significant amount of fuel will be burned in all operating states of the plant, the effects of the fuel-air ratio on flame stability in the combustion chamber, as detailed in subsection 3.2.2, will be neglected.

Ebsilon does not allow polytropic efficiency in the individual gas turbine component, and isentropic gas turbine efficiency is therefore used, along with a default performance characteristic included in Ebsilon. A fraction of the compressor outlet mass flow is extracted for turbine blade cooling according to formula Equation 3.7, as described in subsection 3.2.3. The maximum blade temperature is assumed to be 880 °C, based on [17].

### 6.4.2 Heliostat Field

The layout of the heliostat field component cannot be calculated in Epsilon, and must be provided by the user. The calculation of such a field is nontrivial and generally requires special software. Epsilon's programmers recommend the program HFLCAL, developed by the Deutsches Zentrum for Luft- und Raumfahrt (DLR). The layout is generalized in a field efficiency matrix taking into account the different heliostat efficiencies explained in section 2.3.

Because the calculation of such field efficiency is complex, and no suitable program was immediately available, one of the example heliostat fields provided in Epsilon was used, which is sized for an appropriate thermal power level. In order to ensure a high annual solar share, a solar multiple of 2.5 was chosen at the design point, in order to fill the thermal energy storage to capacity on typical days. Coincidentally, this is equivalent to a total heliostat field area of  $1.0 \text{ km}^2$ , for example spread across 5000 heliostats with an individual area of  $200 \text{ m}^2$ . At the site simulated, a mean daily reduction of around 0,7% of reflector performance has been found due to dust accumulation[100]. Because cleaning of heliostats can take place continuously, this is accounted for in the constant reflectivity efficiency of the plant.

It must be noted that this heliostat field, the layout of which is shown in Figure 6.3, is not optimized for the location of interest, and the total heliostat field efficiency can not be considered valid in this simulation. The efficiency of the provided heliostat field at the design condition is found to be 46.9%, although for an optimized field efficiencies in excess of 60% should be expected[90]. Because the field is not optimized for this location and system, the performance of the heliostat field will not be studied further. While this represents a limitation for this component, it does not significantly effect the performance of the remaining power plant simulation.

The individual heliostats are assumed to be self-powered by individual PV panels, and so do not consume electricity from the grid. In situations of excess solar thermal energy, some heliostats are automatically defocused in order to avoid system damage.

### 6.4.3 Solar Tower and Receiver

The solar receiver is located at the top of a tower, as detailed in subsection 3.3.1. A SOLGATE type pressurized volumetric receiver[49] has been chosen, as it has proved a 70% thermal efficiency in sustained operation. Because a higher TIT is more efficient in a natural gas turbine power plant, solar receiver air temperature should be selected as high as possible. Based on material limitations, a solar receiver temperature of  $1000 \text{ }^\circ\text{C}$  has been proven possible in sustained operation, with a maximum pressure of 15 bar[6, 49]. The pressure drop trough the CRS was set to 0.5 bar based on literature on current technology[40, 101]

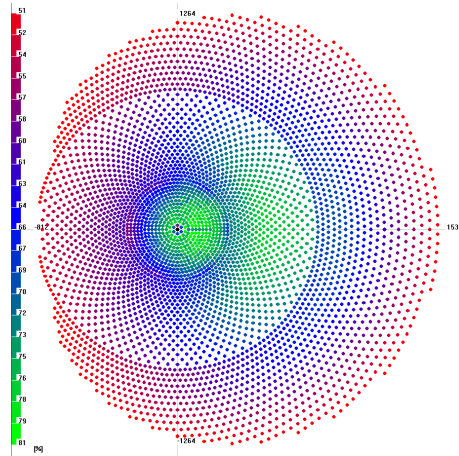


**Figure 6.3:** The heliostat field layout used in the process simulation[90].

Material limitations in uncooled piping and volumetric receivers limit the receiver outlet air temperature to 950 °C however. While some heat exchange will take place in the tower piping, the piping is assumed to be well-insulated, and the effects of tower heat exchange is neglected. Thermal losses from the piping is neglected, and instead included in the solar receiver thermal efficiency. The pressure drop in the tower piping is assumed to be 50 mbar in both directions, based on [17]. Although detailed solar data is available, the solar tower component in Ebsilon automatically neglects any irradiance when the sun is lower than 5 degrees above the horizon, and this represents a small induced inaccuracy in the simulation.

#### 6.4.4 Thermal Energy Storage

A regenerative pressurized indirect thermal energy storage unit, as described in subsection 4.1.2, is included in the power plant. Based on a goal of increased solar share in the plant operation, a maximum storage capacity was chosen so that total discharge time from fully charged at nominal conditions and rated power is 10 hours. With the already selected solar multiple of 2.5 hours, the storage is designed to be filled to capacity on typical days. Packed magnesia fire brick was chosen as the storage material, as it is the material with the most experience as a storage medium[22], and a suitable packing factor can be used in this case with a void fraction of 0.4 [73].

Ebsilon provides a specific component for indirect storage, which simulates the non-steady state nature of thermal storage. The component is primarily intended for simulation of thermal latency in for example piping, and while in theory it is possible to correctly simulate a large-scale thermal storage component, the time steps of 15 minutes prove too long for accurate results. Instead of using this component, a

custom solution for the simulation thus had to be created. It is possible to create user defined components using kernel scripting with the embedded scripting language EbsScript, which is an expanded variation of the PASCAL programming language. Instead of creating a fully custom component for the storage, it was found to be far more convenient to create an approximation, based on a fixed thermal efficiency.

Round trip efficiencies of between 90% and 95% have been found experimentally and numerically for such a pressurized regenerative storage [102, 103], and Pitchumani, et. al. (2014)[104] found that numerical models of packed bed heat transfer are in reasonable agreement with experimental results. Because larger tanks than those studied give a better ratio of storage volume to external heat transfer (and loss) area, and because the thermal stratification remains the same in a larger tank with the same packing factor and density, a 90% round-trip thermal efficiency value can be assumed as a conservative estimate for this simulation. A further parasitic loss is incurred from the recompression necessary during charging of the thermal storage.

In section 4.1, it was shown that because heat transfer only occurs by convection in such a storage vessel, the thermocline is small. For this reason, a large heat vessel can be assumed to be fully stratified. This then means that the output temperature of the storage can be expected to be fairly constant, as the thermal losses from the insulated tank are relatively small. A instantaneous energy loss based on the round-trip efficiency of the tank is therefore applied while charging the storage, leading to a constant storage temperature lower than the charging temperature. While this means that the discharge temperature from storage will be too low immediately after charging, and too high towards the end of discharging, the stratification of the storage and low thermal losses mean that these effects are assumed to cancel each other out, and so a near-constant temperature is assumed during storage discharge.

The simulation setup to allow this simplification is shown in principle in Figure 6.4. In practice, this simplified storage is simulated by using a direct storage component without heat loss, which is given a maximum storage capacity equal to 10 hours of discharge at nominal conditions. As discussed in subsection 4.1.2, when filling the storage, the deposited energy is dependent on the difference between the sensible enthalpies of the incoming air and the compressor outlet air. Therefore, the sensible enthalpy of the charging stream is compared to that of the compressor outlet air, and 10% of the difference is subtracted from the storage charging air. The mass flow of the charging stream is then reintroduced to the cycle with the compressor outlet enthalpy through a recompression blower. This accounts for the varying compressor outlet temperatures depending on ambient temperature, which limit the capacity of the storage. This does not model the transient effects of start-up on storage - it must be heated from ambient, and there is some energy loss in the night - but these

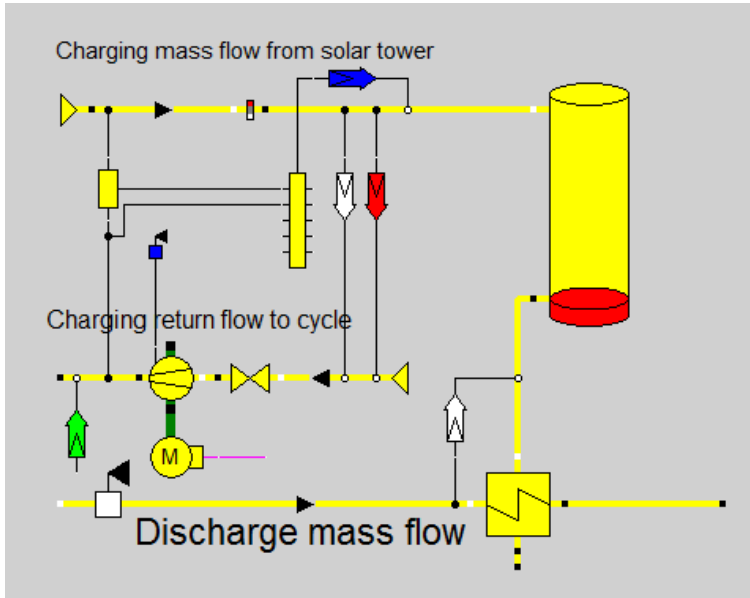


**Figure 6.4:** The simplified simulation of the indirect thermal energy storage.

losses are included in the fixed efficiency.

In essence, a dummy mass flow is introduced into a dummy storage component in the simulation in this way. In the storage solution chosen, the air would flow in reverse through the storage tank when discharging, but Epsilon does not allow for reverse flow streams. Instead, in order to discharge the storage, a dummy mass flow passes through a simplified heat exchanger with 100% efficiency and no pressure loss, transferring enthalpy to the mass stream from the compressor to the combustion chamber. A simple user defined component is used for this, as a normal heat exchanger component sees this is a pinch point violation. The code for the user defined component was provided in Epsilon, and can be found in Appendix B. In the simulation, a controller is used to enable and disable this component.

Based on [103], a 100 mbar pressure drop across the storage has been assumed at nominal charging flow rate. The nominal flow rate is 60% of the total solar tower flow rate at the design condition.

#### 6.4.5 Bottoming Cycle

In order to increase the efficiency of the power plant, a bottoming cycle is included in the simulation. Various bottoming cycles have considered, as described in chapter 5. To select a bottoming cycle, the reduction or elimination of water usage in the plant

has been prioritized, and the air-bottoming cycle proposed by Sandoz et. al. [88] and detailed in section 5.4 has therefore been selected for simulation. The layout of such a cycle integrated in a SHGT power plant is previously shown in Figure 5.12. The air-bottoming cycle relies on three counterflow gas-gas heat exchangers; an intercooler (IC), a recuperator (RC), and the waste heat recovery unit (WHR). The simulation layout of the bottoming cycle is shown in Figure 6.5.

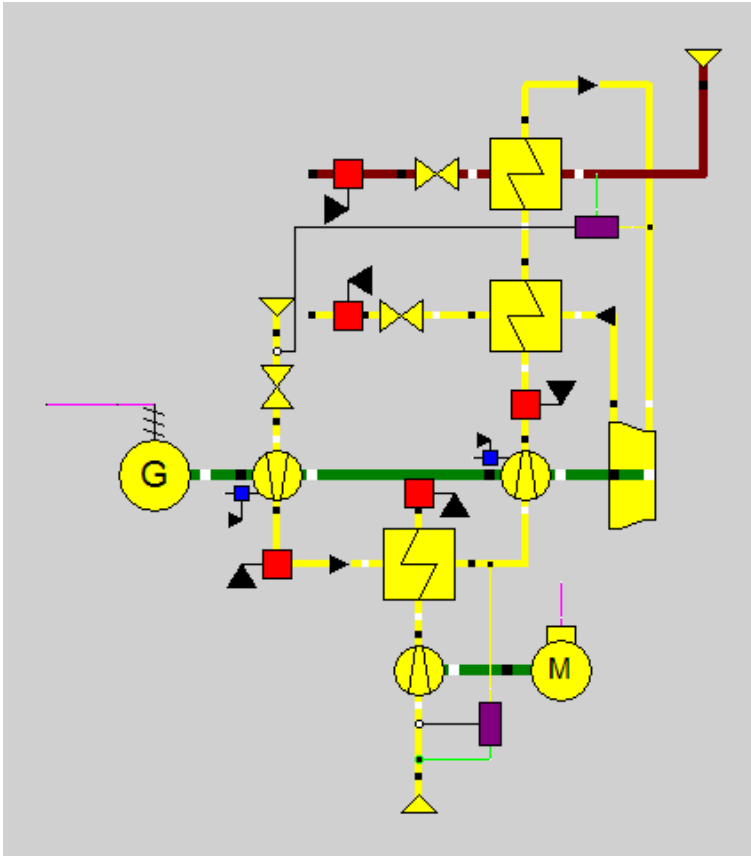


**Figure 6.5:** The simulation model of the bottoming cycle.

Based on [88], a nominal pressure loss of 2% has been assumed for all streams through the heat exchangers; a compression ratio of the bottom cycle compressors of 3.2 is selected; and approach temperatures of 20 °C, 6.5 °C and 24 °C are chosen for the WHR, IC and RC exchangers, respectively, denoting the lower terminal temperature differences of the exchangers.





# Chapter 7

## Process Simulations

### 7.1 The Air-Bottoming Solar Hybrid Gas Turbine Power Plant

An air-bottoming solar hybrid gas turbine (AB SHGT) power plant has been selected for simulation. The layout of the topping cycle, integrating thermal storage, is shown in Figure 7.1. Based on the information in the previous sections, the final power plant process simulation model, shown in Figure 7.2, yields the design point performance characteristics shown in Table 7.1.

The chosen parameters of the power plant are integrated directly in the components, as well as through a number of controller units. In order to handle charging and discharging the thermal energy storage, an EbsScript has been written to handle diversion of the mass flow through the different parts of the power plant. The script is included in Appendix A. The script controls flow splitters throughout the plant that allow for the necessary mass flow paths. A controller ensures that the TES is only charged if there is an excess of solar thermal power. In cases where there is clearly not enough thermal energy available, the controller is always disabled, and the charging flow to storage is set to 0. Likewise, if the storage is filled to capacity, a fraction of the heliostats will be defocused.

Two operating scenarios are considered for simulation. The first is around-the-clock base load power generation, and the second is generating power only when solar heat is available directly or from storage, in order to maximize solar share. One steady-state calculation for every 15 minutes for the year chosen are carried out. In order to consider operation of the power plant only when the solar resource is available, the simulation results are simply truncated to only include situations where thermal energy is added to the working fluid in the solar receiver or from the thermal energy storage.

To briefly illustrate the inter-day effect of varying conditions of the plant, summary

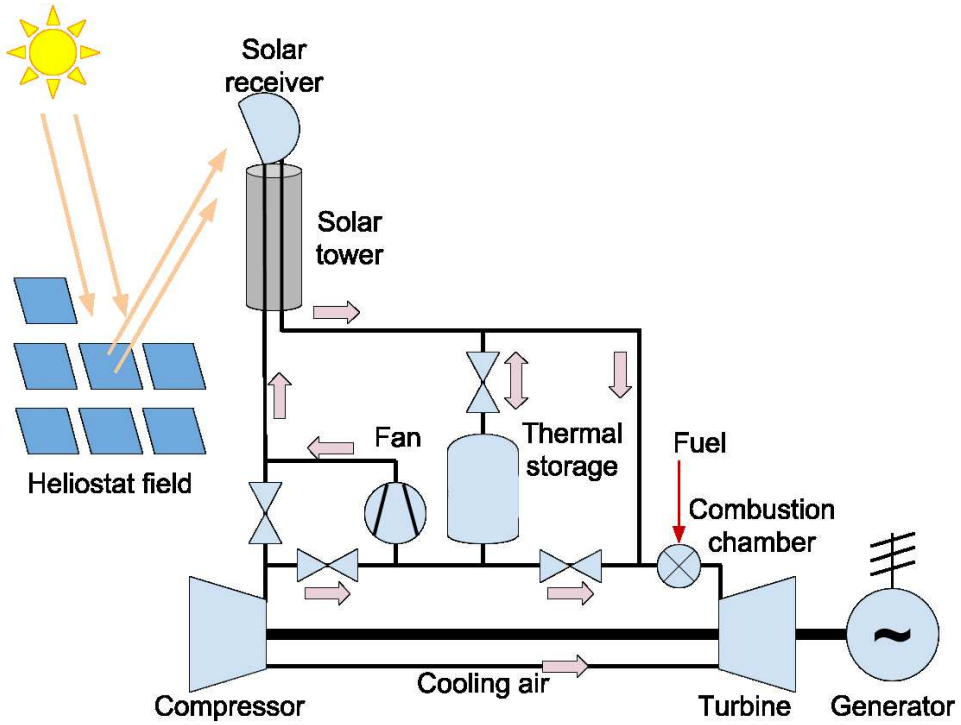


**Figure 7.1:** An illustration of the layout of a hybrid solar gas turbine power plant with a tower central receiver system and the power block and thermal energy storage located at ground level.

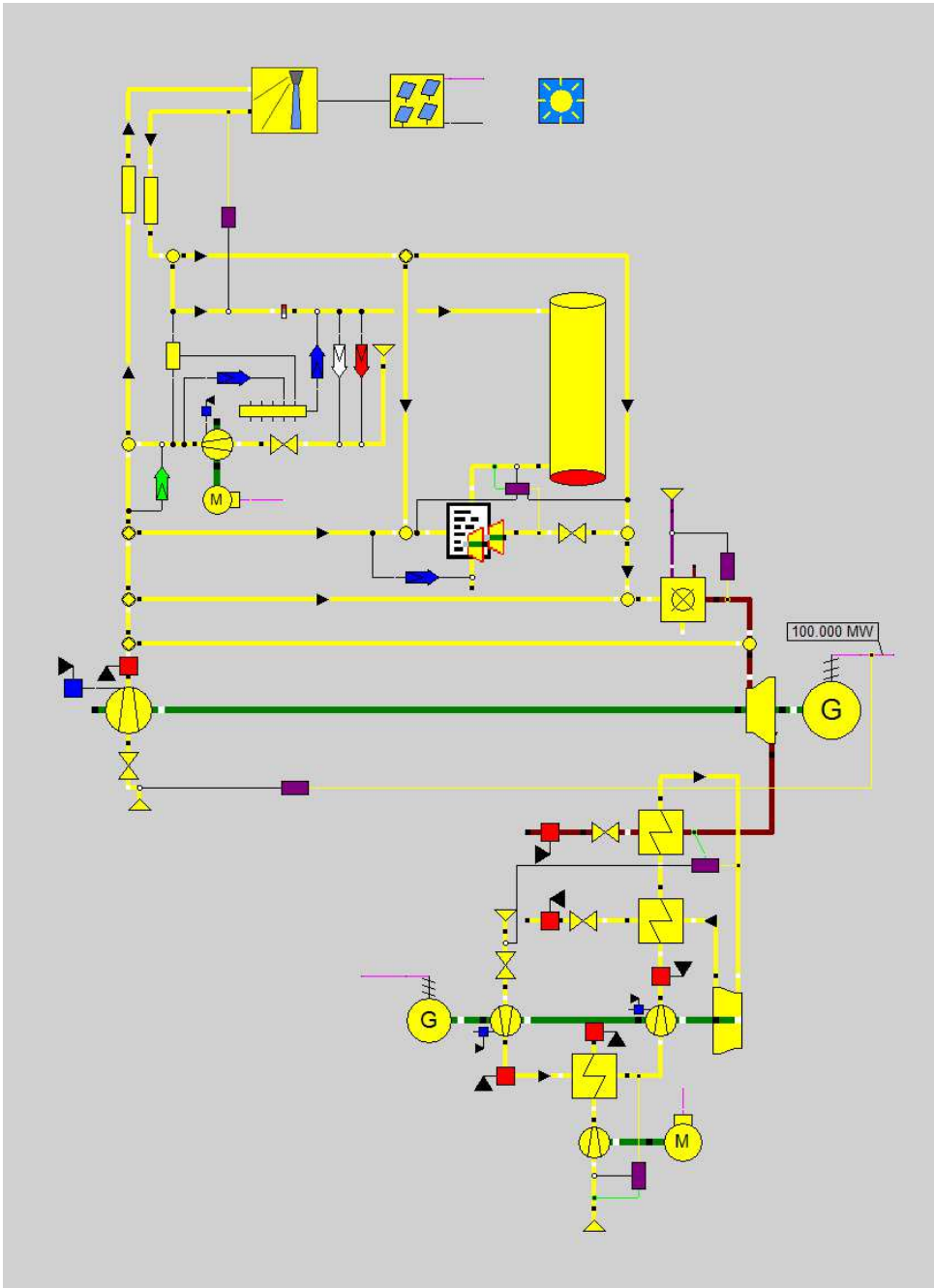
illustrations of the thermal energy storage system performance are given in Figure 7.3 and Figure 7.4.

Figure 7.3 shows the performance of the TES system for three days of high and three days of low irradiance. The energy storage level is drawn in blue, and the DNI values are drawn in black.

Figure 7.4 shows the performance of the storage over three days of variable irradiance, and the fuel mass flow rate, drawn in red, over the same period.

	Value	Unit
Topping cycle nominal power output	100	[MW <sub>e</sub> ]
Bottoming cycle power output at design point	28.2	[MW <sub>e</sub> ]
Compressor pressure ratio	15	[-]
Nominal solar share	50.6	[%]
Thermal energy storage time	10	[h]
Solar multiple	2.5	[-]
Total heliostat reflective area	1.0	[km <sup>2</sup> ]
Solar receiver outlet temperature	950	[°C]
Combustion chamber outlet temperature	1400	[°C]
Maximum turbine blade temperature	880	[°C]
Topping cycle gas exhaust temperature	593	[°C]
Topping cycle exhaust gas mass flow rate	292.3	[kg/s]
Bottoming cycle compressors pressure ratio	3.2	[-]
Bottoming cycle WHR heat exch. approach temperature	20	[°C]
Bottoming cycle IC heat exch. approach temperature	6.5	[°C]
Bottoming cycle RC heat exch. approach temperature	24	[°C]

**Table 7.1:** Performance characteristics of the AB SHGT power plant at design point.



**Figure 7.2:** The process simulation model of the AB SHGT.

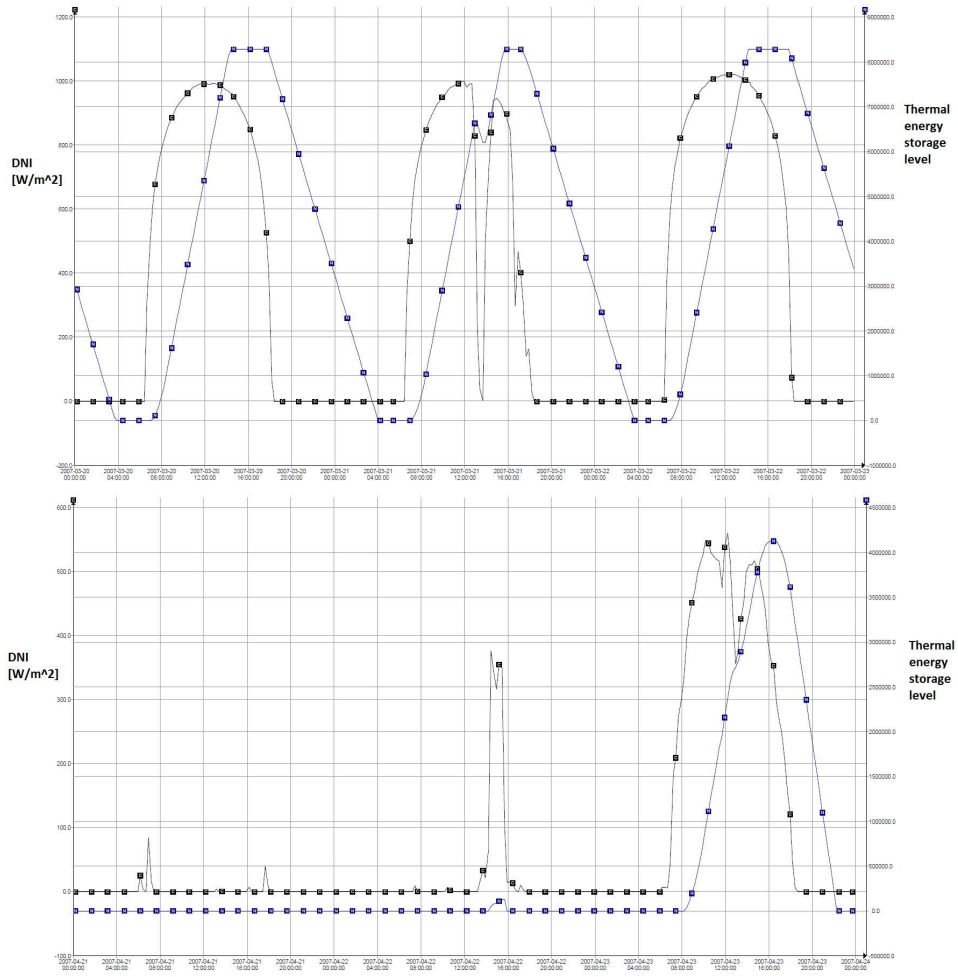


**Figure 7.3:** TES storage level on days of high irradiance (top) and low irradiance (bottom).

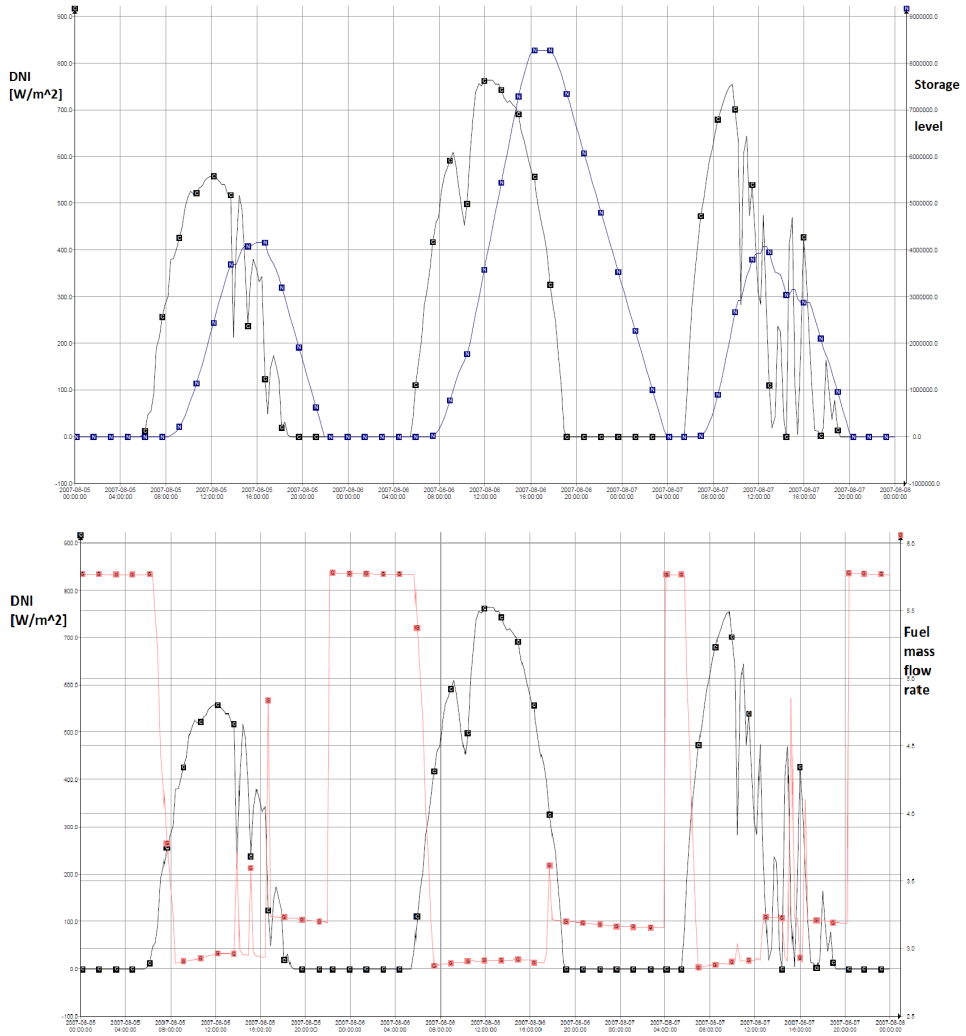


**Figure 7.4:** TES storage level (top) and fuel mass flow rate (bottom) for days of variable irradiance.

## 7.2 Reference Cycles

In order to compare and better evaluate the performance of the plant, two reference cycles have been simulated: a conventional combined cycle gas turbine power plant, and a solar-only SHGT power plant. These reference plants are simulated in the same operating conditions as the proposed plant.

### 7.2.1 Natural Gas Power Plant

For comparison with a currently existing natural gas power plant, a conventional combined cycle gas turbine (CCGT) power plant has been modelled. Such a plant is based on readily available and tested technology, and represent an easily available alternative to the modelled plant. A Siemens SGT6-2000E gas turbine has been chosen, as a common and readily available turbine suitable for both simple- and combined cycle operation, with similar power output to the gas turbine simulated in this thesis. Importantly, data is also available for this turbine in the gas turbine library included in Epsilon[105], which will be useful for validation.

While the natural gas power plant will be subjected to the same ambient temperature as the thesis process model, water usage is assumed not to be of as significant importance as for the CSP case, as such a plant does not have to be located in a comparable location. Therefore, a conventional combined cycle layout, as detailed in section 5.1, is chosen, utilizing a SHRG in a steam Rankine cycle. The additional assumptions related to the natural gas reference power plant are given in Table 7.2, and the process simulation layout is shown in Figure 7.5. The operating strategy of this plant is straightforward and does not require any scripting. The plant is simply subjected to a time-series of simulations of the same ambient conditions as the previously modelled plant.

### 7.2.2 Solar Only Power Plant

In order to examine the effect of co-firing of a solar gas turbine, a solar-only SHGT power plant is examined. Puppe et.al. [61] have proposed a SHGT configuration where the nominal operating temperature of the gas turbine has been reduced to 950 °C. This configuration is selected as a solar reference cycle, as it is well-suited to quantitatively compare the benefit of co-firing. The cycle is also modified to include a similar air-bottoming cycle as the previously modelled plant. The plant layout thus remains the same as that in the previous model, with the exception of a simplified bottoming cycle without recuperation. Re-using the AB SHGT layout already designed also has the benefit of saving time spent modelling. This configuration does include an auxiliary burner to ensure a constant turbine inlet temperature of 950 °C for stable base load power generation. This burner is operated



	Value	Unit
Topping cycle nominal power output	106.35	[MW <sub>e</sub> ]
Topping cycle ISO electrical efficiency	33.0	[%]
Bottoming cycle power output at design point	54.74	[MW <sub>e</sub> ]
CCGT total electrical efficiency	49.3	[%]
Compressor pressure ratio	12.1	[ - ]
Combustion chamber outlet temperature	1330	[°C]
Maximum turbine blade temperature	880	[°C]
Topping cycle gas exhaust temperature	538	[°C]
Topping cycle exhaust gas mass flow rate	365	[kg/s]
Bottoming cycle live steam pressure	48	[bar]
Economizer approach temperature	20	[°C]
HRSG pinch point	10	[°C]
Superheater approach temperature	10	[°C]
Rotating machinery mechanical efficiency	99	[%]
Generator efficiency	98.6	[%]

**Table 7.2:** Performance characteristics of the reference CCGT power plant at design point.

only during transient drops in solar irradiance during the day and to offset the heat losses in the thermal storage.

As previously mentioned, the heliostat field performance is not calculated by Epsilon. In order to generate 100 MW<sub>e</sub> of power in the solar-only SHGT one of the provided solar field models would require drastically scaling one up, leading to very high inaccuracies. Therefore, 50 MW<sub>e</sub> has instead been selected as the nominal power output of the topping cycle in the solar reference case, as this corresponds well to the already modified solar field used for the AB SHGT, and as such provides the same amount of solar energy, which is considered useful for referencing.

The lower gas turbine temperature leads to lower efficiencies in this layout. From [47], the new compressor polytropic efficiency is set to 82% and the turbine isentropic efficiency is set to 87%. The remaining efficiencies, limitations and losses remain as with the AB SHGT. The design point performance parameters of the reference plant are given in Table 7.3, and the process simulation layout is shown in Figure 7.6. The operating strategy of this plant is a modification of that of the AB SHGT power plant, previously discussed in subsection 3.3.3, and the script is updated with adjusted values and modified to shut down the power plant when no solar resource is available.

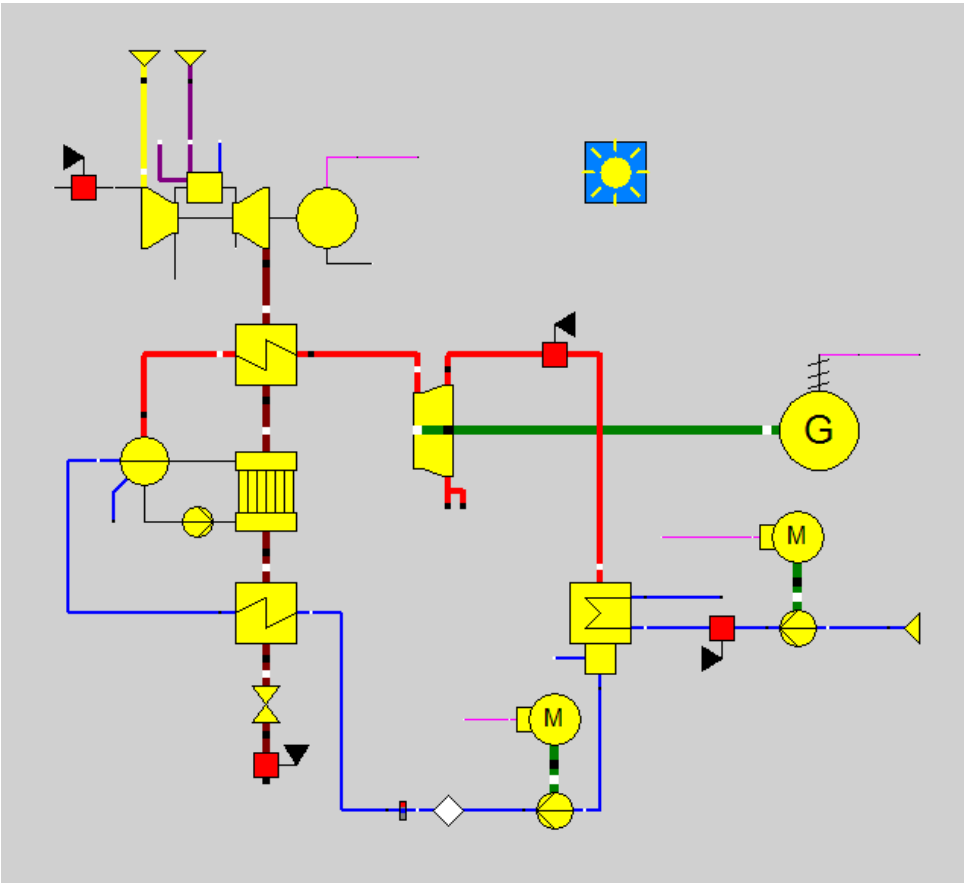


**Figure 7.5:** The process simulation model of the CCGT power plant.

It should be noted that while the solar reference plant is as a consequence of the auxiliary burner not strictly solar-only, it is unrealistic that such a gas turbine plant would be operated without a burner. An alternative of using a molten salt CSP power plant as a solar reference cycle was also considered, but modern molten salt plants in any case generally integrate an auxiliary fossil fuel burner to ensure continuous operation and to prevent freezing of the molten salt. In fact 12-15% of annual electricity production from each CSP plant in Spain, the world leader in CSP capacity, is generated from natural gas[92], and a reference cycle based on existing plants would therefore generally also not be strictly solar-only[18].

	Value	Unit
Topping cycle nominal power output	50	[MW <sub>e</sub> ]
Bottoming cycle power output at design point	9.42	[MW <sub>e</sub> ]
Compressor pressure ratio	15	[-]
Nominal solar share	100	[%]
Thermal energy storage time	10	[h]
Solar multiple	2.5	[-]
Total heliostat reflective area	1.0	[km <sup>2</sup> ]
Solar receiver outlet temperature	950	[°C]
Combustion chamber outlet temperature	950	[°C]
Topping cycle gas exhaust temperature	402	[°C]
Topping cycle exhaust gas mass flow rate	265	[kg/s]
Bottoming cycle compressors pressure ratio	2	[-]
Bottoming cycle WHR heat exch. approach temperature	20	[°C]
Bottoming cycle IC heat exch. approach temperature	6.5	[°C]

**Table 7.3:** Performance characteristics of the solar reference power plant at design point.

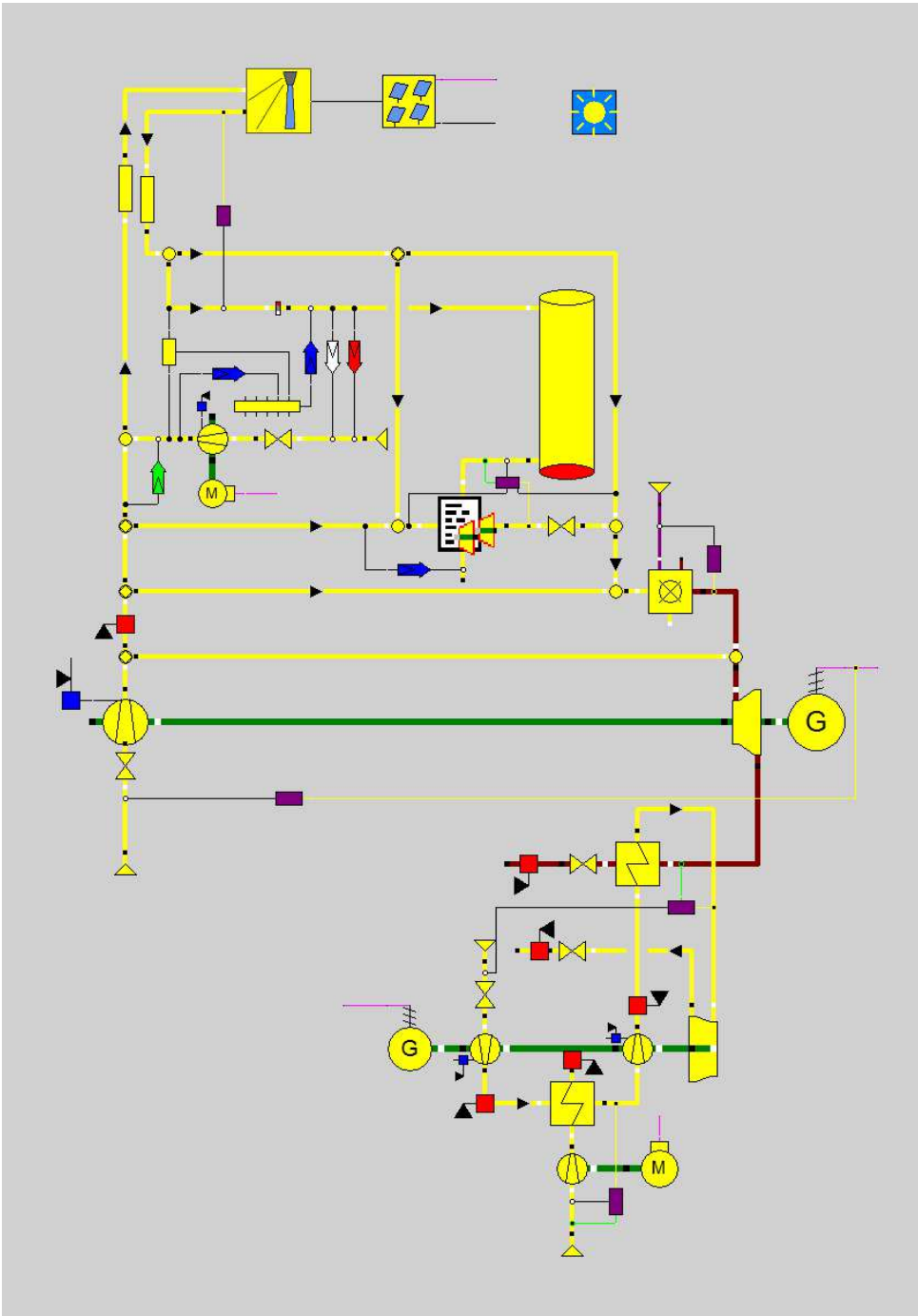


**Figure 7.6:** The process simulation model of the solar reference SHGT power plant.

### 7.3 Steady State Design Point Results

Before further results are presented, a definition for efficiency must be chosen. As discussed in subsection 3.3.2, the thermodynamic efficiency of the SHGT power plant takes into account both thermal power contained in sunlight and thermal power from burning natural gas. In terms of total system losses, the solar part of the plant will appear far less efficient than the natural gas-burning part. This is especially true in this thesis, considering the inaccuracies described in subsection 6.4.2, which will lead to exaggerated thermodynamic inefficiencies for the plant due to larger than necessary losses in the heliostat field. For this reason, the equation previously derived for efficiency, Equation 3.14, which considers thermal energy added to the fluid in the solar receiver and thermal energy added to the fluid in the combustion chamber, will be used in this chapter. Unless otherwise noted, results for efficiency in this chapter will be referring to this definition. For comparative purposes, the fuel-electric efficiency and heat rate, as defined by Equation 3.12 and Equation 3.13, which only account for the energy from the natural gas fuel, will also be given.

The simulated temperature-entropy diagrams of the topping and bottoming cycles of the AB SHGT, the reference solar plant and the bottoming cycle of the reference combined cycle gas turbine plant are shown in the following figures.

In Figure 7.7, the paths represent the following:

- A-B: Compression
- B-C: Heating in the solar receiver
- C-D: Combustion chamber heating
- D-E: Mixing with cooling air
- E-F: Expansion
- F-G: Heat release in the waste heat recovery unit

In Figure 7.8, the paths represent the following:

- A-B-C-D: Compression, intercooling and compression
- D-E: Heating by recuperator
- E-F: Heating in the waste heat recovery unit
- F-G: Expansion

- G-H: Heating in the recuperator

The paths in the remaining T-s-diagrams are analogue, with the exception of the steam Rankine bottoming cycle, which matches the one described in chapter 5.

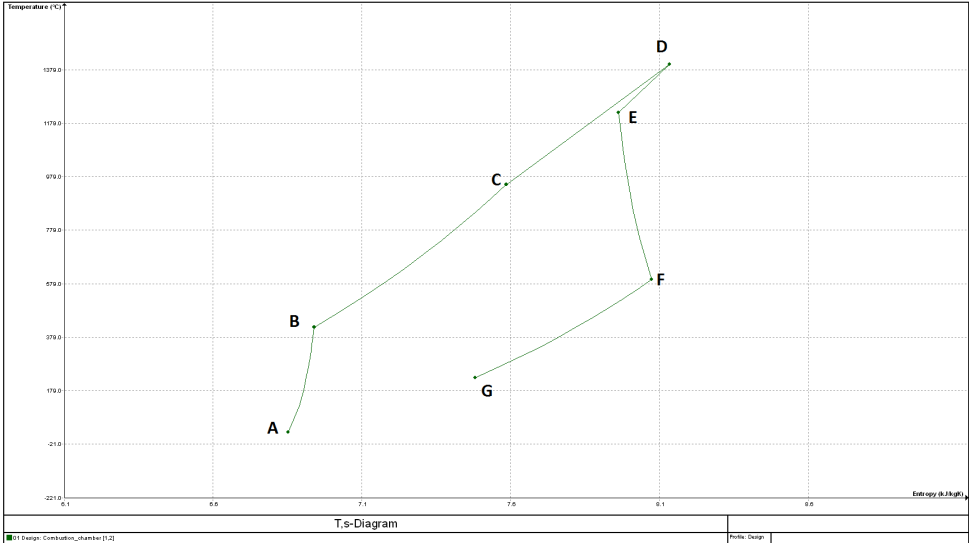


**Figure 7.7:** The T-s-diagram of the AB SHGT topping cycle

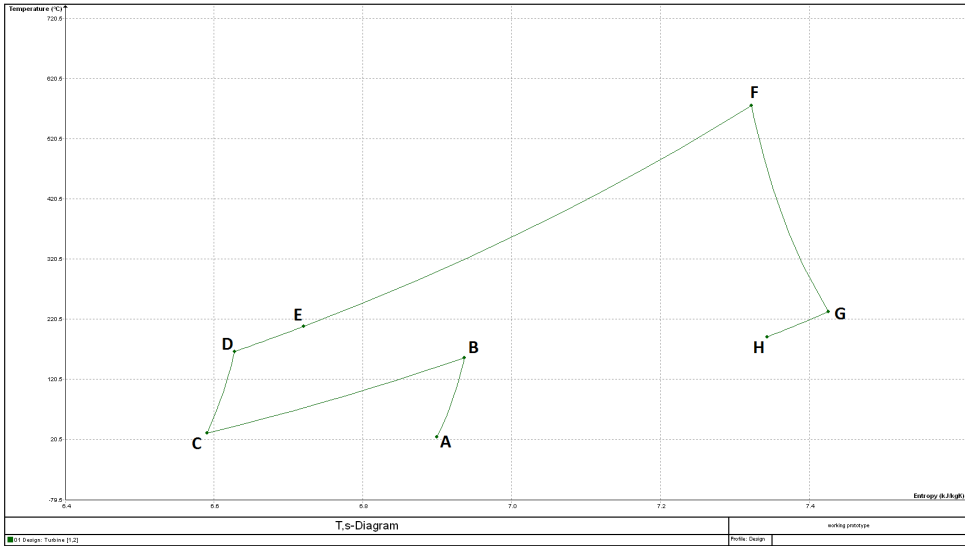


Figure 7.8: The T-s-diagram of the AB SHGT bottoming cycle

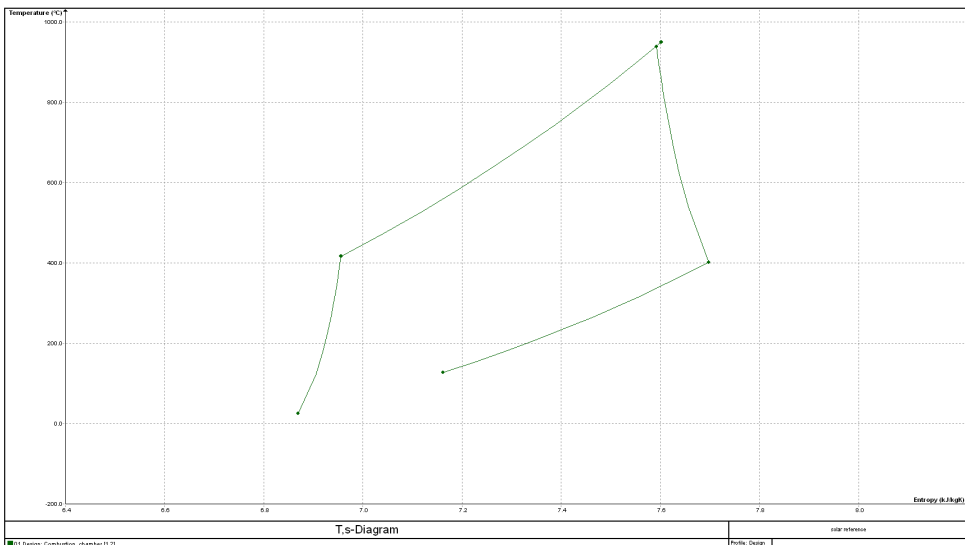
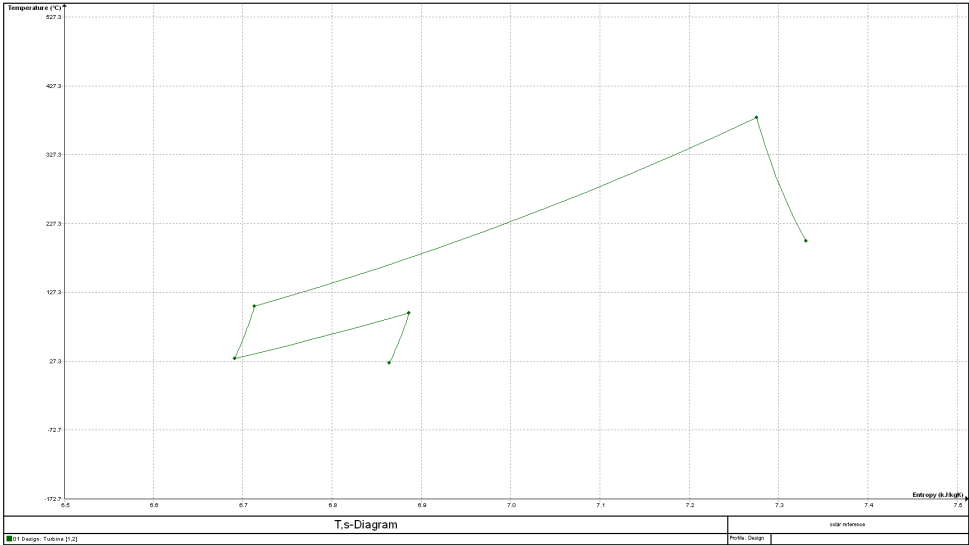
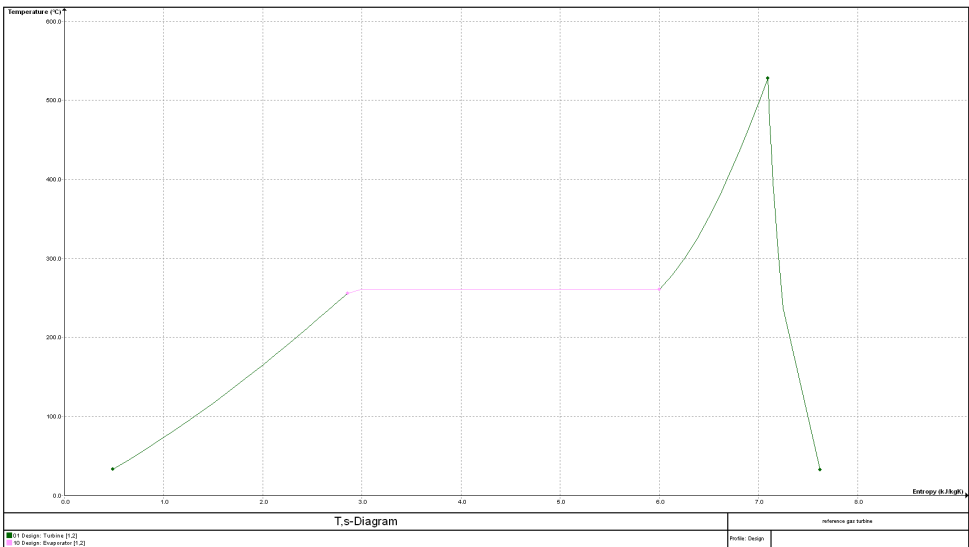


Figure 7.9: The T-s-diagram of the solar reference topping cycle



**Figure 7.10:** The T-s-diagram of the solar reference bottoming cycle



**Figure 7.11:** The T-s-diagram of the combined cycle gas turbine reference bottoming cycle



The SHGT power plant has been modelled for two different operating scenarios: 24-hour base load operation, and operation only when solar thermal power is available. To ease distinction, these two scenarios will be referred to in the following simply as "24-hour SHGT" and "solar-limited SHGT". The results of the design point process simulations are presented in Table 7.4. As mentioned previously, concentrated solar power plants rarely operate at their design point conditions, due to the high variability in irradiance through the day. Most days in suitable locations do reach the design irradiance value for some hours in the middle of the day, and so the design point results are nevertheless of interest, but dynamic or quasi-dynamic modelling is essential.

	Unit	AB SHGT	Reference gas turbine	Solar reference
Total plant power output	[MW <sub>e</sub> ]	128.2	158.6	70.52
Bottom cycle power fraction	[%]	22	33.2	29.1
Nominal solar share	[%]	50.6	0	100
Efficiency	[%]	40.6	49.3	23.5
Fuel mass flow rate	[kg/s]	2.92	6.44	0
Fuel-electric efficiency	[%]	85.9	49.3	-
Heat rate	[kJ <sub>th</sub> /kWh <sub>e</sub> ]	1164	7302	-
Specific carbon emissions	[g CO <sub>2</sub> /kWh <sub>e</sub> ]	229.4	403.8	-

**Table 7.4:** A comparison of the steady state simulation results for the process models at design point.

## 7.4 Annual Performance Results

Somewhat more than 35,000 steady state simulations were carried out for each of the models, which allows an acceptable resolution to see intra-hour variation in performance based on both gradual and sudden variations in solar resources in the course of a day. The simulation performance results of the annual performance of the four cycle scenarios are given in Table 7.5. A graphical comparison of performance parameters of the cycle scenarios is given in Figure 7.12. Note that the annual fuel-electric efficiency of the solar reference cycle has been truncated in the figure in order to increase readability of the remaining bars. This clearly illustrates the weakness of different efficiency calculations, as the solar reference cycle uses so little natural gas as to reach in excess of 400% fuel-electric efficiency. For the SHGT plant designed however, where the natural gas fuel must be expected to make up a sizeable portion of operating expenses, the fuel-electric efficiency shows that there is a significant potential for fuel savings with the SHGT, especially if the plant is not operated after the storage is fully discharged.

The base load SHGT power plant yields a modest 20% reduction in specific carbon emissions along with a 25.5% increase in fuel-electric efficiency compared the the CCGT reference. This efficiency increase must be treated with caution however,

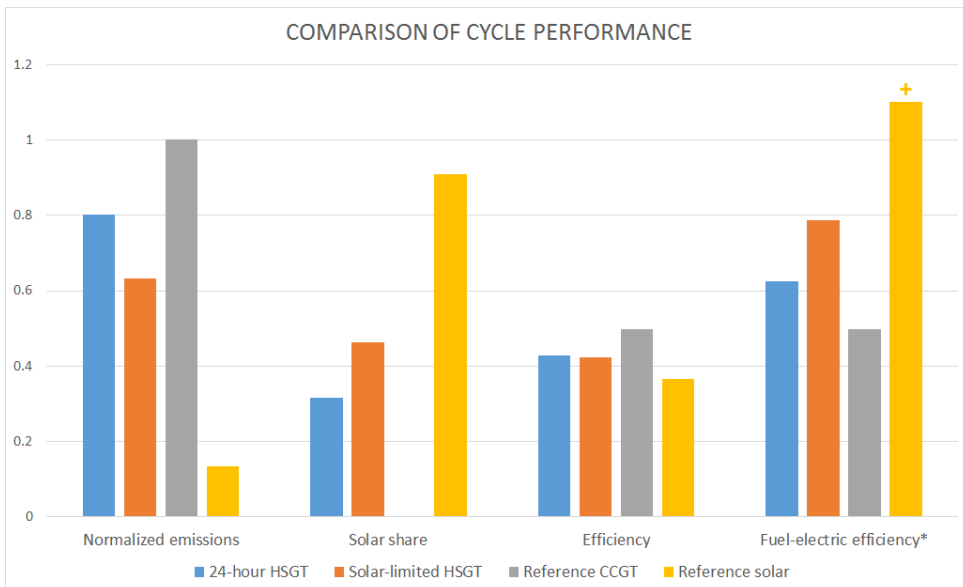


**Figure 7.12:** A graphical comparison of performance aspects of the simulated cycles.

	Unit	24-hour SHGT	Solar-limited SHGT	Reference gas turbine	Solar reference
Average uptime power output	[MW <sub>e</sub> ]	123.6	122.7	160.1	58.94
Capacity factor	[ - ]	1	0.680	1	0.680
Total plant power output	[GWh <sub>e</sub> ]	1082	731.4	1402	3513
Bottom cycle power fraction	[%]	19.7	19.3	34.1	16.9
Annual solar share	[%]	31.7	46.4	0	90.9
Efficiency	[%]	42.7	42.2	49.7	36.7
Fuel-electric efficiency	[%]	62.4	78.8	49.7	405
Heat rate	[kJ <sub>th</sub> /kWh <sub>e</sub> ]	5762	4570	7243	888
Specific carbon emissions	[g CO <sub>2</sub> /kWh <sub>e</sub> ]	322.1	253.8	401.3	54.2

**Table 7.5:** A comparison of the performance results of the four scenarios simulated over a year.

as it does not take into account the additional investments in solar components and the maintenance work especially related to the solar heliostat field.

The solar-limited SHGT, with a solar share of 46.4 %, shows more pronounced fuel cost savings and emissions reductions, with specific carbon emission reduction of 35.6% along with an increase in fuel-efficiency of more than 58.5%, although with a slight thermal efficiency reduction. Compared to the solar reference, the additional efficiency gained by raising the firing temperature in the gas turbine is modest, at 16.3 % and 15.0 % for the base load and solar-limited SHGT respectively. This must be compared to a significant reduction in the solar share of the power generated.

The solar-limited SHGT seems to represent a clear compromise between emissions and efficiency, and it is not immediately clear if this compromise is worthwhile.

The SHGT shows relatively low bottom cycle power fraction, which likely represents a potential for increased efficiency through optimization. The exhaust temperature of the SHGT after bottoming remains close to 229 °C, and shows that the bottoming cycle has significant potential for further optimization. Further

study of the air-cooled steam Rankine cycle as described in chapter 5 should also be considered.

There is also potential for improvement in the efficiency of the topping Bratyon cycle, which is currently limited by a 15 bar pressure maximum in the solar receiver. This limitation is based on current technology, and it is therefore reasonable to expect that higher pressures are possible in future receiver technology. While a higher compression ratio in the cycle will lead to lower turbine exhaust temperatures, it may still be worthwhile to also integrate a recuperator in the SHGT, especially considering the need for total air extraction from the gas turbine casing. This need means that commercially available recuperated gas turbines can be easier to integrate in a SHGT system than those with a fully closed casing, as discussed in subsection 3.3.1. Another option could be to integrate another compressor-intercooler stage in the bottoming cycle, with the drawbacks of increased complexity and expense.

## 7.5 Sensitivity Analysis

A sensitivity analysis has been carried out for ranges of up to +/- 10% change in the absolute value of the following model parameters:

- Combustion chamber outlet temperature
- Solar receiver outlet temperature
- Topping cycle compression ratio
- Bottoming cycle compression ratio
- Ambient temperature
- Compressor efficiency
- Turbine efficiency

The results of the sensitivity analysis are presented in Figure 7.13. A significant positive correlation was identified for changes in combustion chamber outlet temperature, and compressor and turbine, and likewise a significant negative correlation was found for changes in ambient temperature.

Less than 2% relative change in efficiency was found across the range of parameter variations for both the topping cycle and bottoming cycle compression ratios and the solar receiver outlet temperature. It is worth noting that there was a small negative correlation for changes in the solar receiver outlet temperature. While a

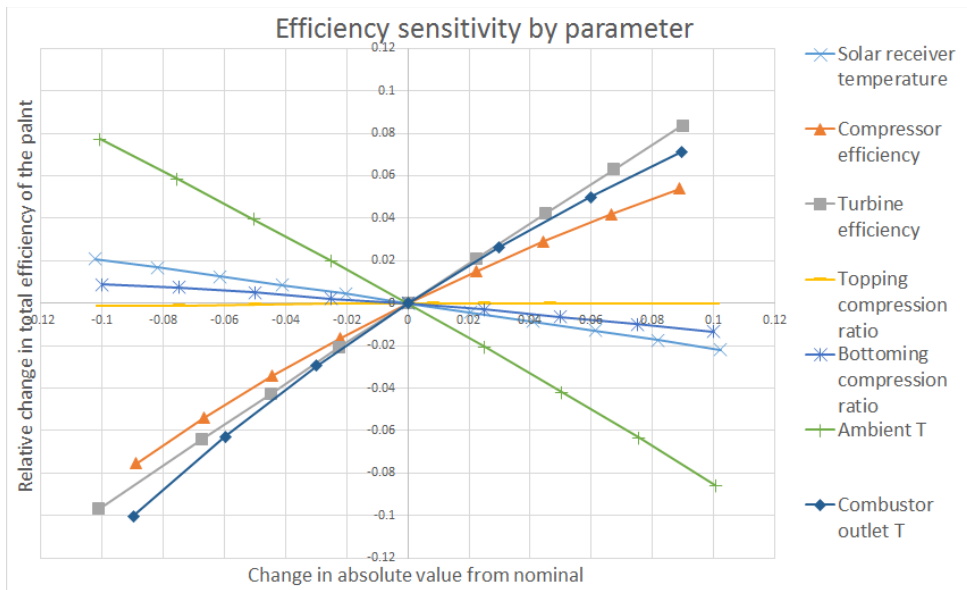


**Figure 7.13:** Relative change in total power plant efficiency compared to deviations from design parameters.

higher temperature is generally wanted in the receiver, this reduction in efficiency stems from the associated pressure and temperature losses in the solar receiver tower, which are more significant than the losses in the combustion chamber. It is therefore still worthwhile to maximize the solar receiver temperature at a small efficiency loss if it desirable to raise the solar share.

## 7.6 Validation

In order to validate the model, the simulation results should be compared to results from other simulations or, preferably, to real-world performance data. The SHGT simulation models built in this thesis are based on a large number of assumptions, as little experimental data exists for a plant with similar parameters. Due to a lack of data for comparison, a full validation of the SHGT simulation was not carried out.

Instead, in order to provide a cursory evaluation of the performance of the process simulation, the reference cycle gas turbine, Siemens SGT6-2000, was modelled using individual components in Epsilon, and set to generate the same electric power in the same boundary conditions. This is done by the same methodology as for the previous simulations, as shown in Figure 7.14. The same general model assumptions as before are assumed, and the performance assumptions of the modelled turbine are given in

Table 7.6, with ISO conditions: 1.013 bar pressure, 60% relative air humidity and an ambient temperature of 15 °C. This modelled turbine is then compared to the performance of the gas turbine component in Epsilon, which uses data provided by the manufacturer to simulate performance.

The benefit of this approach is that it is a simple way to evaluate the performance of a collection of simulation components as compared to validable data from the gas turbine manufacturer. The reference turbine performance data in the library is collected from the manufacturer software SIPEP (Siemens Plant Performance Estimation Program) by VTU Energy GmbH.[105]. Notably, the power output performance of the reference turbine according to this manufacturer data differs significantly from that advertised by Siemens[106]. Because the library performance data is collected from the manufacturer’s own estimates of performance, the library data is considered valid rather than that advertised. The results of the simulation are presented in Table 7.7.

This does not validate the previous simulation, especially considering the significant number of assumptions and uncertainty related to the solar part of the plant. It does however provide a cursory overview of the performance of the simulations under the assumptions used, and in terms of efficiency accuracy, the validation simulation shows good performance. Notably, moderate deviations were found in both the exhaust mass flow rate and temperature. This indicates some additional uncertainty in the SHGT modelled based on the same principles.

---

<sup>1</sup>In comparison to the simulation data provided by the manufacturer.

	Value	Unit
Combustion chamber outlet temperature	1330	[°C]
Compression ratio	12.1	[ - ]
Maximum turbine blade temperature	880	[°C]
Compressor polytropic efficiency	90	[%]
Combustion chamber thermal efficiency	99	[%]
Turbine isentropic efficiency	89	[%]
Rotating machinery mechanical efficiency	99	[%]
Generator efficiency	98.6	[%]

**Table 7.6:** Assumptions used in the process simulation

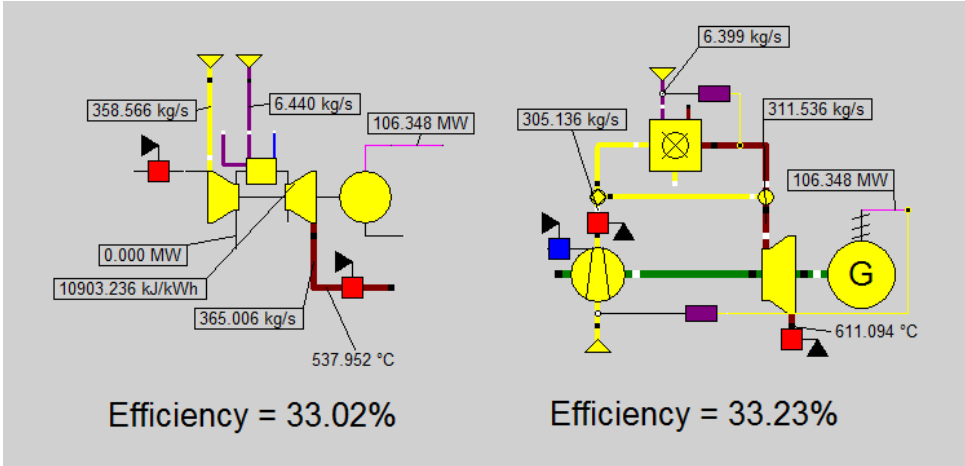


**Figure 7.14:** A graphical comparison of performance aspects of the simulated cycles.

	Unit	Advertised performance data	Manufacturer performance data	Modelled turbine	Error <sup>1</sup> [%]
Nominal power output	[MW <sub>e</sub> ]	112	106.348	106.348	-
Efficiency	[%]	33.9	33.02	33.23	0.64
Exhaust temperature	[°C]	540	538.0	611.1	13.6
Exhaust mass flow rate	[kg/s]	365	365	311.5	- 14.7

**Table 7.7:** The results of the validation simulation

# Chapter 8

## Conclusions and Further Work

### 8.1 Conclusions

This thesis builds on a literature study of solar gas turbine hybrid systems, including thermal storage and bottoming cycles. Based on this, a suitable candidate location and boundary conditions have been selected for simulation of a power plant. An air-bottoming solar hybrid gas turbine power plant was chosen for further study and designed. Based on steady-state simulations of this plant, quasi-dynamic simulations were made possible to simulate the different operating conditions a plant will experience. Annual simulations of such conditions have been carried out for two different operating scenarios and for two reference cycles. A sensitivity analysis and limited model validation have also been carried out.

The simulations carried out in this thesis were all in a steady state or quasi-steady state in 15 minute time steps. Therefore, transient operation of the plant in question is not detailed fully. A large number of the values used for design of the simulation plant were collected from theoretical literature, as currently little experimental data exists. Due to the high number of assumptions not based on experimental results, the process simulations and results are associated with a high degree of uncertainty, which is further exacerbated by limited model validation. This is especially true of the solar thermal parts of the plant, such as the heliostat field and the thermal energy storage.

Of the two considered plant scenarios, the solar-limited SHGT is viewed as the most promising, yielding a 58.5% increase in fuel-electric efficiency, and a 35.6% reduction in specific CO<sub>2</sub> emissions. In this configuration, a capacity factor of 68.0 % is still achieved, and the plant is online during all peak hours, as well as being available during downtime to run as a conventional gas turbine plant if necessary. The solar-limited SHGT thus seems to represent a clear compromise between emissions and efficiency, and seems worthy of further study. Meanwhile, based on the modest emissions reductions and fuel saving of the base load SHGT, it seems unlikely that



the configuration chosen has potential as a 24-hour base load power plant.

The impact of the power plant on the nearby environment or animal life due to space usage and other concerns have not been studied. Conversely, effects from the environment that may disrupt the plant, such as dust, storms, high winds or other effects have not been considered in detail. The maintenance requirements of the plant, such as cleaning of its reflective mirrors on a regular basis, have not been considered. Similarly, the costs of the technologies described in this thesis have not been considered, and the results are therefore primarily of use for comparative purposes and performance estimation.

In the end, investment and operations costs must be considered to be the deciding factor in choosing between the technologies, as the reduction in fuel usage is at the expense of very significant investment in relatively novel technologies.

## 8.2 Further Work

While the candidate SHGT power plant is not promising for base load power generation, its solar-limited configuration - operating only when thermal energy is available from sunlight or thermal storage - is interesting for further study. Such study could consider different operating conditions for the plant, such as load shifting and more variable power output in a dispatchable power generation configuration.

The SHGT also shows promise as a spinning reserve by operating at little or no load using solar power only. By integrating thermal storage, a simple cycle SHGT power plant can be available as a spinning reserve around the clock with only minor emissions.

Before investing in power generation, considering the levelized cost of electricity (LCOE) is of vital importance. The SHGT represents substantial increased investment as well as an additional need for maintenance, and the overall cost of the plant should be accounted for in order to properly optimize its parameters depending on the plant operational goals. The study of the costs related to construction and maintenance of a SHGT is therefore of central importance for any further study.

Theoretically a silicon carbide pressurized receiver could provide temperatures high enough to power the gas turbine nearly without heat input from the fuel at design point. It may be of interest to investigate a theoretical plant with cooled ducting between the central receiver and the turbine inlet or with a small enough power block that it can be co-located with the receiver.

The integration of thermal storage relies heavily on accurate modelling of the fully transient components involved in direct and indirect energy storage[107], and

this may also be a gainful area for investigation.

The impact of the power plant on its surroundings and vice versa, such as through water usage and weather effects, are likely to be important to plant performance and interesting for further study. The PSA research center, where the solar data for this thesis has been collected, is extensively studied[94, 95]. Based on the available data, a multi-year simulation can be carried out to observe the effects of changing inter-annual insolation on a CSP plant, possibly considering the effects of a changing climate in terms of weather and atmospheric conditions.

Apart from these suggestions, a number of smaller improvements could be made to improve the accuracy of the simulation, or investigate other situations, such as:

- Considering costs, when including carbon emissions taxes, such as levelized electricity costs, and strategies to reduce these, as well as investment costs in general.
- Considering other pollutants from combustion than  $CO_2$ , and strategies to minimize these
- Carrying out simulations on shorter time scales to investigate other quasi-transient or fully dynamic behaviour.
- Simulation of other modes of operation, such as the effects of inclement weather or grid fluctuations.
- Optimization of technology used in the current simulations, especially the bottoming cycle
- Integrating solar fuel production or  $CO_2$  capture in a CSP plant with a large solar multiple.



# References

- [1] European Commission and Directorate-General for Climate Action, *Climate change*. Luxembourg: Publications Office, 2015.
- [2] Intergovernmental Panel on Climate Change, *Climate Change 2013 - The Physical Science Basis : Working Group I Contribution to the Fifth Assessment Report of the Intergovernmental Panel on Climate Change*. Cambridge: Cambridge University Press, 2014.
- [3] R. Guerrero-Lemus and J. M. Martínez-Duart, “Concentrated Solar Power,” in *Renewable Energies and CO<sub>2</sub>*, no. 3 in Lecture Notes in Energy, pp. 135–151, Springer London, 2013.
- [4] A. J. Sangster, “Energy from Ancient and Modern Sunshine,” in *Electromagnetic Foundations of Solar Radiation Collection*, Green Energy and Technology, pp. 1–25, Springer International Publishing, 2014. DOI: 10.1007/978-3-319-08512-8\_1.
- [5] R. Margolis, C. Coggeshall, and J. Zuboy, “SunShot vision study,” *US Dept. of Energy*, 2012.
- [6] R. Pitz-Paal, “How the Sun gets into the Power Plant,” in *Renewable Energy* (R. Wengenmayr and T. Bürke, eds.), pp. 28–35, Wiley-VCH Verlag GmbH & Co. KGaA, 2012.
- [7] G. W. Team, *Global Energy Assessment: Toward a Sustainable Future*. Cambridge University Press, Aug. 2012.
- [8] SeeNews, “S Arabia to generate 110 TWh of electricity from CSP by 2032 - SeeNews Renewables,” 2012.
- [9] C. Philibert, *Technology roadmap: concentrating solar power*. OECD/IEA, 2010.
- [10] REN21, *Renewables 2016 Global Status Report*. Paris: Renewable Energy Policy Network for the 21st Century, 2016.
- [11] A. Neslen, “Morocco poised to become a solar superpower with launch of desert mega-project,” *The Guardian*, Oct. 2015.

- [12] A. D. B. Group, “Morocco: Works on World’s Largest Solar Plant Financed by AfDB Go Underway,” 2013.
- [13] REN21, *Renewables 2015 Global Status Report*. Paris: Renewable Energy Policy Network for the 21st Century, 2015.
- [14] O. Behar, A. Khellaf, and K. Mohammedi, “A review of studies on central receiver solar thermal power plants,” *Renewable and Sustainable Energy Reviews*, vol. 23, pp. 12–39, July 2013.
- [15] A. DiPaola, “Saudi Arabia Delays \$109 Billion Solar Plant by 8 Years,” 2015.
- [16] I. E. Agency, *Publication: Technology Roadmap: Solar Thermal Electricity - 2014 edition*. 2014.
- [17] J. Spelling, *Hybrid Solar Gas-Turbine Power Plants: A Thermo-economic Analysis*. PhD thesis, KTH Royal Institute of Technology, 2013.
- [18] W. Vogel, *Large-scale solar thermal power : technologies, costs and development*. Wiley-VCH, 2010.
- [19] K. Lovegrove and W. Stein, *Concentrating Solar Power Technology: Principles, Developments and Applications*. Elsevier, Oct. 2012.
- [20] S. A. Kalogirou, *Solar Energy Engineering, 2nd Edition*. Academic Press, 2 ed., Oct. 2013.
- [21] D. R. W. Mueller, “Solar Irradiance solar irradiance/irradiation , Global Distribution solar irradiance/irradiation global distribution,” in *Solar Energy* (C. Richter, D. Lincot, and C. A. Gueymard, eds.), pp. 553–583, Springer New York, 2013. DOI: 10.1007/978-1-4614-5806-7\_447.
- [22] D. Y. Goswami, *Principles of solar engineering*. Taylor & Francis, 2nd ed. ed., 2000.
- [23] SolarGIS, “World Direct Normal Irradiation (DNI) Map,” 2016.
- [24] M. Romero-Alvarez and E. Zarza, “Concentrating solar thermal power,” in *Handbook of energy efficiency and renewable energy*, Taylor & Francis, 2007.
- [25] J. Spelling, R. Guédez, and B. Laumert, “A Thermo-Economic Study of Storage Integration in Hybrid Solar Gas-Turbine Power Plants,” *Journal of Solar Energy Engineering*, vol. 137, pp. 011008–011008, Aug. 2014.
- [26] A. J. Sangster, “Concentrated Solar Power,” in *Electromagnetic Foundations of Solar Radiation Collection*, Green Energy and Technology, pp. 173–206, Springer International Publishing, Jan. 2014.
- [27] R. Guerrero-Lemus and J. M. Martínez-Duart, *Renewable Energies and CO<sub>2</sub>: Cost Analysis, Environmental Impacts and Technological Trends- 2012 Edition*. Springer Science & Business Media, Sept. 2012.

- [28] S. Kuravi, J. Trahan, D. Y. Goswami, M. M. Rahman, and E. K. Stefanakos, “Thermal energy storage technologies and systems for concentrating solar power plants,” *Progress in Energy and Combustion Science*, vol. 39, pp. 285–319, Aug. 2013.
- [29] K. M. Powell and T. F. Edgar, “Modeling and control of a solar thermal power plant with thermal energy storage,” *Chemical Engineering Science*, vol. 71, pp. 138–145, Mar. 2012.
- [30] S. M. CSIRO, “Heliostat mirror field at the National Solar Energy Centre in Newcastle NSW,” June 2007.
- [31] W. B. Stine and R. W. Harrigan, *Solar Energy Systems Design: A Computer Based Approach*. Wiley, 1985.
- [32] A. Pfahl, M. Randt, F. Meier, M. Zschke, C. P. W. Geurts, and M. Buselmeier, “A Holistic Approach for Low Cost Heliostat Fields - International Conference on Concentrating Solar Power and Chemical Energy Systems, SolarPACES 2014,” *Energy Procedia*, vol. 69, pp. 178–187, May 2015.
- [33] P. K. Falcone, “A Handbook for Solar Central Receiver Design,” Tech. Rep. SAND-86-8009, Sandia National Labs., Livermore, CA (USA), Dec. 1986.
- [34] S. Corporation, “Sandia, Stirling Energy Systems set new world record for solar-to-grid conversion efficiency,” 2008.
- [35] ABB, “Press Release: ABB investment sharpens solar focus,” Mar. 2011.
- [36] A. T. Kearney, “Solar thermal electricity 2025,” *Clean Electricity on Demand: Attractive STE Cost Stabilize Energy Production*, 2010.
- [37] F. J. Collado, “Quick evaluation of the annual heliostat field efficiency,” *Solar Energy*, vol. 82, pp. 379–384, Apr. 2008.
- [38] I. R. E. A. (IRENA), “IRENA-ETSAP Tech Brief E10 Concentrating Solar Power.pdf,” tech. rep., International Renewable Energy Agency (IRENA), 2013.
- [39] M. P. Boyce, *Gas Turbine Engineering Handbook (Fourth Edition)*. Oxford: Butterworth-Heinemann, 2012.
- [40] A. L. Ávila Marín, “Volumetric receivers in Solar Thermal Power Plants with Central Receiver System technology: A review,” *Solar Energy*, vol. 85, no. 5, pp. 891–910, 2011.
- [41] V. Siva Reddy, S. C. Kaushik, K. R. Ranjan, and S. K. Tyagi, “State-of-the-art of solar thermal power plants—A review,” *Renewable and Sustainable Energy Reviews*, vol. 27, pp. 258–273, Nov. 2013.
- [42] P. Breeze, *Power Generation Technologies*. Elsevier Science, 2nd ed. ed., 2014.

- [43] Michael J. Moran, *Fundamentals of engineering thermodynamics*. Wiley, 6th ed., si version. ed., 2010.
- [44] H. I. H. Saravanamuttoo, H. Cohen, G. F. C. Rogers, and P. V. Straznicky, *Gas turbine theory*. Prentice Hall, 6th ed. ed., 2009.
- [45] H. I. H. Saravanamuttoo, G. F. C. Rogers, and H. Cohen, *Gas Turbine Theory*. Pearson Education, Jan. 2001.
- [46] O. Bolland, *Thermal Power Generation*. Trondheim: NTNU, 2014.
- [47] R. K. Bhargava, M. Bianchi, A. D. Pascale, G. N. d. Montenegro, and A. Peretto, “Gas Turbine Based Power Cycles - A State-of-the-Art Review,” in *Challenges of Power Engineering and Environment* (P. K. Cen, P. Y. Chi, and D. F. Wang, eds.), pp. 309–319, Springer Berlin Heidelberg, 2007. DOI: 10.1007/978-3-540-76694-0\_56.
- [48] J. Spelling, B. Laumert, and T. Fransson, “Optimal Gas-Turbine Design for Hybrid Solar Power Plant Operation,” *Journal of Engineering for Gas Turbines and Power*, vol. 134, pp. 092301–092301, July 2012.
- [49] P. Heller, M. Pfänder, T. Denk, F. Tellez, A. Valverde, J. Fernandez, and A. Ring, “Test and evaluation of a solar powered gas turbine system,” *Solar Energy*, vol. 80, no. 10, pp. 1225–1230, 2006.
- [50] B. Grange, C. Dalet, Q. Falcoz, F. Siros, and A. Ferrière, “Simulation of a Hybrid Solar Gas-turbine Cycle with Storage Integration,” *Energy Procedia*, vol. 49, pp. 1147–1156, Jan. 2014.
- [51] F. J. Brooks, “GE gas turbine performance characteristics,” *GE Power Systems, Schenectady, NY*, 2000.
- [52] C. Felsmann, U. Gampe, S. Heide, and M. Freimark, “Modeling and Simulation of the Dynamic Operating Behavior of a High Solar Share Gas Turbine System,” *Journal of Engineering for Gas Turbines and Power*, vol. 137, pp. 031601–031601, Oct. 2014.
- [53] G. Barigozzi, G. Bonetti, G. Franchini, A. Perdichizzi, and S. Ravelli, “Solar Hybrid Combined Cycle Performance Prediction Influence of Gas Turbine Model and Spool Arrangements,” *Journal of Engineering for Gas Turbines and Power*, vol. 134, pp. 121701–121701, Oct. 2012.
- [54] S. T. Inc., “Mercury 50,” 2013.
- [55] A. Rao, “Advanced industrial gas turbines for power generation,” in *Combined Cycle Systems for Near-Zero Emission Power Generation*, Woodhead Publishing, Apr. 2012.
- [56] P. Schwarzbözl, R. Buck, C. Sugarmen, A. Ring, M. J. Marcos Crespo, P. Altwegg, and J. Enrile, “Solar gas turbine systems: Design, cost and perspectives,” *Solar Energy*, vol. 80, pp. 1231–1240, Oct. 2006.

- [57] U. Fisher, C. Sugarmen, A. Ring, and J. Sinai, “Gas Turbine “Solarization”-Modifications for Solar/Fuel Hybrid Operation,” *Journal of Solar Energy Engineering*, vol. 126, pp. 872–878, July 2004.
- [58] J. Spelling, B. Laumert, and T. Fransson, “Advanced Hybrid Solar Tower Combined-cycle Power Plants - Proceedings of the SolarPACES 2013 International Conference,” *Energy Procedia*, vol. 49, pp. 1207–1217, Jan. 2014.
- [59] A. Rao, *Combined Cycle Systems for Near-Zero Emission Power Generation*. Woodhead Publishing, Apr. 2012.
- [60] D. Olivenza-León, A. Medina, and A. Calvo Hernández, “Thermodynamic modeling of a hybrid solar gas-turbine power plant,” *Energy Conversion and Management*, vol. 93, pp. 435–447, Mar. 2015.
- [61] M. Puppe, S. Giuliano, M. Krüger, O. Lammel, R. Buck, S. Boje, K. Saidi, U. Gampe, C. Felsmann, M. Freimark, and U. Langnickel, “Hybrid High Solar Share Gas Turbine Systems with Innovative Gas Turbine Cycles - International Conference on Concentrating Solar Power and Chemical Energy Systems, SolarPACES 2014,” *Energy Procedia*, vol. 69, pp. 1393–1403, May 2015.
- [62] K. Guodong Liu and K. Tomsovic, “Quantifying Spinning Reserve in Systems With Significant Wind Power Penetration,” *Power Systems, IEEE Transactions on*, vol. 27, no. 4, pp. 2385–2393, 2012.
- [63] S. Kalaiselvam and R. Parameshwaran, eds., *Thermal Energy Storage Technologies for Sustainability*. Boston: Academic Press, 2014.
- [64] A. Sharma, V. V. Tyagi, C. R. Chen, and D. Buddhi, “Review on thermal energy storage with phase change materials and applications,” *Renewable and Sustainable Energy Reviews*, vol. 13, pp. 318–345, Feb. 2009.
- [65] M. Medrano, A. Gil, I. Martorell, X. Potau, and L. F. Cabeza, “State of the art on high-temperature thermal energy storage for power generation. Part 2—Case studies,” *Renewable and Sustainable Energy Reviews*, vol. 14, pp. 56–72, Jan. 2010.
- [66] A. Gil, M. Medrano, I. Martorell, A. Lázaro, P. Dolado, B. Zalba, and L. F. Cabeza, “State of the art on high temperature thermal energy storage for power generation. Part 1—Concepts, materials and modellization,” *Renewable and Sustainable Energy Reviews*, vol. 14, pp. 31–55, Jan. 2010.
- [67] OECD, *Harnessing Variable Renewables: A Guide to the Balancing Challenge*. Organisation for Economic Co-operation and Development, 2011.
- [68] U. Herrmann and D. W. Kearney, “Survey of Thermal Energy Storage for Parabolic Trough Power Plants,” *Journal of Solar Energy Engineering*, vol. 124, pp. 145–152, Apr. 2002.



- [69] L. Moens, D. M. Blake, D. L. Rudnicki, and M. J. Hale, "Advanced thermal storage fluids for solar parabolic trough systems," *Journal of solar energy engineering*, vol. 125, no. 1, pp. 112–116, 2003.
- [70] C. today, "Diagram illustrating the use of molten salt as a heat transfer fluid and storage medium," 2015.
- [71] W. Phillips, "Effects of stratification on the performance of solar air heating systems," *Solar Energy*, vol. 26, no. 2, pp. 175–180, 1981.
- [72] P. Klein, T. H. Roos, and T. J. Sheer, "Parametric analysis of a high temperature packed bed thermal storage design for a solar gas turbine," *Solar Energy*, vol. 118, pp. 59–73, Aug. 2015.
- [73] G. Zanganeh, A. Pedretti, A. Haselbacher, and A. Steinfeld, "Design of packed bed thermal energy storage systems for high-temperature industrial process heat," *Applied Energy*, vol. 137, pp. 812–822, Jan. 2015.
- [74] D. M. Crandall and E. F. Thacher, "Segmented thermal storage," *Solar Energy*, vol. 77, pp. 435–440, Oct. 2004.
- [75] A. A. Jalalzadeh-Azar, W. G. Steele, and G. A. Adebisi, "Heat Transfer in a High-Temperature Packed Bed Thermal Energy Storage System—Roles of Radiation and Intraparticle Conduction," *Journal of Energy Resources Technology*, vol. 118, pp. 50–57, Mar. 1996.
- [76] J. T. Van Lew, P. Li, C. L. Chan, W. Karaki, and J. Stephens, "Analysis of Heat Storage and Delivery of a Thermocline Tank Having Solid Filler Material," *Journal of Solar Energy Engineering*, vol. 133, pp. 021003–021003, Mar. 2011.
- [77] H. Singh, R. P. Saini, and J. S. Saini, "A review on packed bed solar energy storage systems," *Renewable and Sustainable Energy Reviews*, vol. 14, pp. 1059–1069, Apr. 2010.
- [78] K. Y. Wang, R. E. West, F. Kreith, and P. Lynn, "High-temperature sensible-heat storage options," *Energy*, vol. 10, pp. 1165–1175, Oct. 1985.
- [79] Z. Wang, B. Sakadjian, S. Hu, M. Maryamchik, T. Flynn, K. Santelmann, and Z. Ma, "Fluidized-bed Technology Enabling the Integration of High Temperature Solar Receiver CSP Systems with Steam and Advanced Power Cycles - International Conference on Concentrating Solar Power and Chemical Energy Systems, SolarPACES 2014," *Energy Procedia*, vol. 69, pp. 1404–1411, May 2015.
- [80] S. M. Hasnain, "Review on sustainable thermal energy storage technologies, Part II: cool thermal storage," *Energy Conversion and Management*, vol. 39, pp. 1139–1153, Aug. 1998.
- [81] G. Glatzmaier, "Summary Report for Concentrating Solar Power Thermal Storage Workshop," *National Renewable Energy Laboratory, Golden, CO, Report No. NREL/TP-5500-52134*, 2011.

- [82] D. R. Brown, J. L. La Marche, and G. E. Spanner, “Chemical Energy Storage System for Solar Electric Generating System (SEGS) Solar Thermal Power Plant,” *Journal of Solar Energy Engineering*, vol. 114, pp. 212–218, Nov. 1992.
- [83] M. Korobitsyn, University of Twente (Enschede), and Department of Mechanical Engineering, *New and advanced energy conversion technologies: analysis of cogeneration, combined and integrated cycles*. Enschede; Enschede: Department of Mechanical Engineering, University of Twente ; University of Twente [Host, 1998. OCLC: 67984977.
- [84] A. Rao, “Integrated gasification combined cycle (IGCC) systems,” in *Combined Cycle Systems for Near-Zero Emission Power Generation*, Woodhead Publishing, Apr. 2012.
- [85] Moiz-shashwat, “topping and bottoming cycles,” 2013.
- [86] T. Paanu, S. Niemi, and P. Rantanen, “Waste Heat Recovery – Bottoming Cycle Alternatives,” in *PROCEEDINGS OF THE UNIVERSITY OF VAASA*, 2012.
- [87] P. J. Mago and K. K. Srinivasan, “Exhaust Waste Heat Recovery From Stationary Engines Using Organic Rankine Cycles,” 2010.
- [88] R. Sandoz, J. Spelling, B. Laumert, and T. Fransson, “Air-Based Bottoming-Cycles for Water-Free Hybrid Solar Gas-Turbine Power Plants,” *Journal of Engineering for Gas Turbines and Power*, vol. 135, p. 101701, Sept. 2013.
- [89] M. Reale, “New High Efficiency Simple Cycle Gas Turbine—GE’s LMS100™,” *GE Energy*, 2004.
- [90] S. E. S. Gmbh, “EBSILON®Professional 11.04,” 2015.
- [91] GeoModel Solar, “Maps of Direct normal irradiation (DNI) in Europe and Spain,” 2015.
- [92] International Energy Agency, *Technology Roadmap: Concentrating Solar Power*. IEA Technology Roadmaps, OECD Publishing, May 2010.
- [93] M. y. T. C. Centro de Investigaciones Energéticas, “La Plataforma Solar de Almería (PSA).”
- [94] GeoModel Solar, “Data - Full Time Series - Plataforma Solar de Almería (PSA), Spain,” 2012.
- [95] D. Pozo-Vázquez, S. Wilbert, C. Gueymard, L. Alados-Arboledas, F. Santos-Alamillos, and M. Granados-Munoz, “Interannual variability of long time series of DNI and GHI at PSA, Spain,” in *Proc. SolarPACES Conf., Granada, Spain*, 2011.
- [96] N. US Department of Commerce, “ESRL Global Monitoring Division - Global Radiation Group.”

- [97] I. O. for Standardization, *Gas Turbines - Acceptance Tests, ISO 2314:2009*. 2009.
- [98] C. Soares, *Gas Turbines, 2nd Edition*. Butterworth-Heinemann, 2 ed., Nov. 2014.
- [99] P. Kiamah, *Power Generation Handbook : Selection, Applications, Operation, Maintenance: Selection, Applications, Operation, Maintenance*. McGraw Hill Professional, Aug. 2002.
- [100] N. Geuder, "Solar Resource Measurements and Satellite Data," 2013.
- [101] Z. Wu, C. Caliot, F. Bai, G. Flamant, Z. Wang, J. Zhang, and C. Tian, "Experimental and numerical studies of the pressure drop in ceramic foams for volumetric solar receiver applications," *Applied Energy*, vol. 87, pp. 504–513, Feb. 2010.
- [102] M. Hänchen, S. Brückner, and A. Steinfeld, "High-temperature thermal storage using a packed bed of rocks – Heat transfer analysis and experimental validation," *Applied Thermal Engineering*, vol. 31, pp. 1798–1806, July 2011.
- [103] G. Zanganeh, A. Pedretti, S. Zavattoni, M. Barbato, and A. Steinfeld, "Packed-bed thermal storage for concentrated solar power – Pilot-scale demonstration and industrial-scale design," *Solar Energy*, vol. 86, pp. 3084–3098, Oct. 2012.
- [104] R. Pitchumani, P. Klein, T. H. Roos, and T. J. Sheer, "Experimental Investigation into a Packed Bed Thermal Storage Solution for Solar Gas Turbine Systems - Proceedings of the SolarPACES 2013 International Conference," *Energy Procedia*, vol. 49, pp. 840–849, Jan. 2014.
- [105] V. E. GmbH, "Gas Turbine Performance Information Library for Epsilon Professional," tech. rep., 2014.
- [106] "Siemens - Gas Turbine SGT6-2000e."
- [107] P. H. Wagner, *Thermodynamic simulation of solar thermal power stations with liquid salt as heat transfer fluid*. diploma, Technische Universität München, 2012.
- [108] L. E. Bakken, "Thermodynamics - Compression and Expansion Processes," 2014.
- [109] E. M. Helsing, "Adiabatic compressed air energy storage," *132*, 2015.
- [110] M. D. Joesten, J. L. Hogg, and M. E. Castellion, *The World of Chemistry: Essentials: Essentials*. Cengage Learning, 2006.

# Appendix

## Process Simulation Control

### EbsScript

The following page contains the kernel script code controlling the behaviour of the power plant simulation under different operating conditions.

```

1  uses @KernelScripting;
2
3  begin
4
5  // The following controller enables and disables charging of the TES. The splitters
6  // divert the mass flow directly to the combustor, to the TES storage path and to the TES
7  // discharge path in series with the solar receiver, respectively.
8
9  Controller_TES_charge.FFU:=1;
10 Splitter_bypass.M3M1:=0;
11 Splitter_TES_discharge.M3M1:=0;
12 Splitter_CRS_and_TES.M3M1:=0;
13
14 // All simulations are carried out in off-design mode:
15 setCalcProfileByName("OD");
16
17 if (Sun.DNI < 50 OR Sun.SHEIGHT < 5) then // If no sun, the CRS part of the plant
18 is idle
19 begin
20 if (TES.LEVACT > TES.LEVMIN+1) then // For no sun, use TES heat if available
21 begin
22 Controller_TES_charge.FFU:=0;
23 Splitter_TES_discharge.M3M1:=1;
24 simulate;
25 state.M:=1; // state.M simply indicates which mode
26 the plant is in for information
27 end
28 else // Otherwise plant is in GT only
29 operation
30 begin
31 Controller_TES_charge.FFU:=0;
32 Splitter_bypass.M3M1:=1;
33 simulate;
34 state.M:=2;
35 end
36 end
37 else // Else there's enough sun to operate
38 the CRS
39 begin
40 if (Solar_tower.RQEFF < 130000) then // For heat input below 130MW_th,
41 operating the controller for charging the TES is not enabled, as there will
42 not be enough heat to reach nominal temperature in the receiver
43 begin
44 if (TES.LEVACT > TES.LEVMIN+1) then // If there's TES heat
45 available, it is used to heat the mass flow after the CRS
46 begin
47 Controller_TES_charge.FFU:=0;
48 Splitter_CRS_and_TES.M3M1:=1;
49 simulate;
50 state.M:=3;
51 end
52 else // If no TES heat, the mass flow is
53 directed from the CRS directly to the combustion
54 chamber
55 begin
56 simulate;
57 state.M:=4;
58 end;
59 end
60 else // If the available Q is greater
61 than the turbine minimum, we can also charge the TES
62 begin
63 if (TES.LEVACT < TES.LEVMAX-1) then // If the TES is not full, it
64 may be charged
65 begin
66 simulate;
67 state.M:=5;
68 end
69 else // If the TES is already full, the

```

```
57         mass flow through the CRS is reduced by disabling the controller,  
58         and the heliostat field is automatically partially defocused  
59         begin  
60         Controller_TES_charge.FFU:=0;  
61         simulate;  
62         state.M:=6;  
63         end  
64     end; end  
65 end.  
66
```



# Appendix **B**

## **Kernel Scripted Heat Exchange Component**

The following page contains the kernel scripting code for a simple heat exchanger component, included in Epsilon by [90] and used in the modelling of the thermal energy storage.



```

1  uses @KernelScripting;
2
3  var
4  i,iIndex,iLZ:integer;
5  strEquation:string;
6  bOk:boolean;
7  var m1,m3:real;
8  begin
9  iLZ:=ksGetItNo;
10
11  if ksGetMode = Initializing then
12  // Mass and pressure equations need to be set only in the 1st iteration step,
13  // because they remain unchanged
14  begin
15  ksRemoveAllEquations;
16  strEquation:="M9-M2=0";
17  ksSetEquation (1,strEquation);
18  strEquation:="M14-M5=0";
19  ksSetEquation (2,strEquation);
20  strEquation:="P9-P2=0";
21  ksSetEquation (3,strEquation);
22  strEquation:="P14-P5=0";
23  ksSetEquation (4,strEquation);
24  strEquation:="H9-H2=0";
25  ksSetEquation (5,strEquation);
26  end
27  else
28  // Energy balance equations change in every iteration step, because
29  // the mass flows could have changed
30  begin
31  m1:=ksGetPipeValue (2,PhysValueM);
32  m3:=ksGetPipeValue (5,PhysValueM);
33  if (iLZ<5 and m1 < 1) then m1:=1;
34  if (iLZ<5 and m3 < 0.1) then m3:=0.1;
35  strEquation:=printToString (m1,"*H2-",m1,"*H9+",m3,"*H5-",m3,"*H14=0");
36  ksSetEquation (5,strEquation);
37  end;
38
39  // Output of the equations in Log-output (optional)
40  iIndex:=ksGetMaxEquationIndex;
41  for i:=1 to iIndex do
42  begin
43  strEquation:=ksGetEquation(i);
44  print (strEquation,"\n");
45  end;
46  end;
47

```

# Appendix

## Basic Thermodynamic Background

In relation to the computer simulations, it is helpful to perform a cursory review of the some fundamental thermodynamic principles and definitions related to this thesis. The definitions used in this chapter are collected from “Fundamentals of Engineering Thermodynamic” by Michael J. Moran[43], "Gas Turbine Theory" by H. I. H. Saravanamuttoo[45] and "Thermodynamics - Compression and Expansion Processes" by Lars Erik Bakken[108].

### C.1 The First Law of Thermodynamics

The first law of thermodynamics states that, for a closed system, the only way energy change can occur in the system is through transfer by work or heat. In other words, energy is conserved, so that the change in system energy,  $\Delta E_{system}$ , can be described as[43]:

$$\Delta E_{system} = \Delta E_{kinetic} + \Delta E_{potential} + \Delta U = Q - W. \quad (C.1)$$

Meanwhile, for an open system, mass may cross the system boundaries. In the same way that energy is preserved, mass is preserved, so that

$$\frac{dm_{cv}}{dt} = \dot{m}_1 - \dot{m}_0. \quad (C.2)$$

By combining Equation C.1 and Equation C.2, and expanding the energy terms, we have the equation for the energy balance of an open system[43]:

$$\Delta E_{cv}/dt = \dot{Q} - \dot{W} + \dot{m}_1(u_1 + C_1^2/2 + gz_1) - \dot{m}_0(u_1 + C_0^2/2 + gz_0). \quad (C.3)$$

We now introduce the expression for enthalpy,

$$h = u + pv, \quad (\text{C.4})$$

and expand the work term from Equation C.3:

$$\dot{W} = \dot{W}_{cv} + \dot{m}_0(p_0v_0) - \dot{m}_1(p_1v_1). \quad (\text{C.5})$$

Combining Equation C.4 and Equation C.5, we end up with the following general form for the energy rate balance[43, 109]:

$$\Delta E_{cv}/dt = \dot{Q}_{cv} - \dot{W}_{CV} + \sum_i \dot{m}_i(h_i + C_i^2/2 + gz_i) - \sum_o \dot{m}_o(h_o + C_o^2/2 + gz_o). \quad (\text{C.6})$$

This energy balance holds that the change in system energy is equal the change in energy over time in the control volume is equal to the change in energy because of heat, work and energy carried by mass flow across the boundary. At steady state this change is equal to zero. This is an important result, because we will see in chapter 6, that our system is potentially frequently not at steady state.

## C.2 The Second Law of Thermodynamics

Simply put, the second law states that the total quantity of energy in the universe is constant. Alternatively, as a slightly easier rule: "you can never get something for nothing"[110]. More rigidly, the Clausius statement asserts "It is impossible for any system to operate in such a way that the sole result would be an energy transfer be heat from a cooler to a hotter body."[43]. The implication of this law in the universe is that there can never be any perfect heat engines or any 100% reversible processes[43].

## C.3 Reversibility and Entropy

While there are no truly perfect heat engines, it can often be practical to imagine, and calculate based on, the opposite. The Carnot Cycle[43],

$$\eta_{max} = 1 - \frac{T_C}{T_H}, \quad (\text{C.7})$$

describes the efficiency of a reversible process between a hot and a cold reservoir. We see that the Carnot efficiency can only become large if  $T_H \gg T_C$ . From this we learn that in order for a heat engine to be efficient,  $T_H$  should be maximized, since we usually have little control of the cold reservoir around any heat engine. This is also the reason why the CSP systems examined in chapter 2 with higher concentration ratios and therefore higher operating temperatures show the most promise for large-scale production.

Because there are always some manner of friction losses and the like in a real-life heat engine, the real efficiency of one must necessarily be lower than the Carnot efficiency. In order to understand how far any process is from ideal, we introduce entropy, defined as[43]:

$$S_2 - S_1 = \left( \int_1^2 \frac{\delta Q}{T} \right)_{int, rev}. \quad (C.8)$$

Entropy is the loss of energy in a process due to irreversibilities, and so if the entropy generated is equal to zero, the process in question is lossless and reversible. We denote such a reversible process as isentropic. If we introduce the term  $\dot{\sigma}_{cv}$  as the rate of entropy production in a system per time, we can write the entropy balance in a control volume as[43]:

$$\frac{S_{cv}}{dt} = \sum_j \frac{\dot{Q}_j}{T_j} + \sum_i \dot{m}_i s_i - \sum_o \dot{m}_o s_o + \dot{\sigma}_{cv}. \quad (C.9)$$

Like with the energy balance for a control volume, the sum of this equation is zero for a system at steady state.



# Appendix **D**

## **Annual Irradiance Values**

The values of direct normal irradiance (DNI) used in this thesis are provided by GeoModel Solar[94] with a 15-minute resolution. A summary overview of the daily DNI values is given in the following pages. The complete data is available at <http://geomodelsolar.eu/data/full-time-series>.

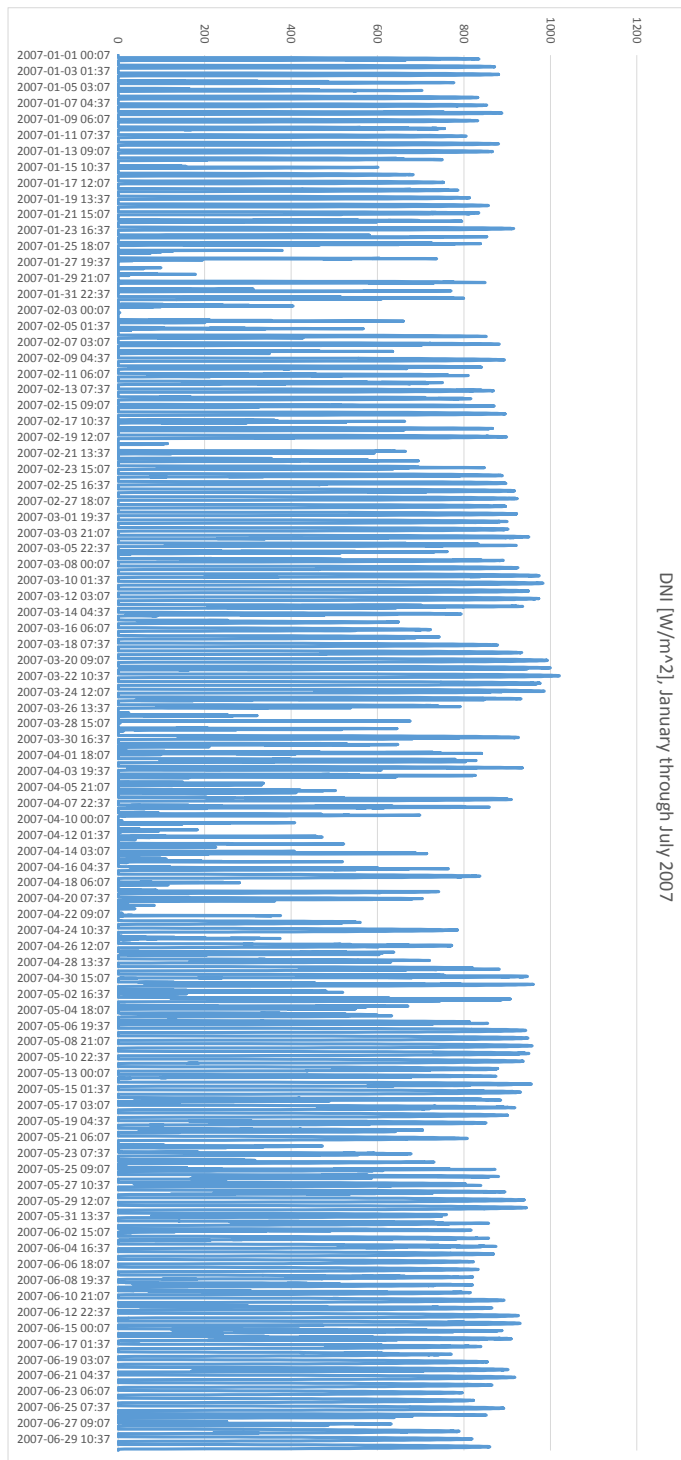


**Figure D.1:** An overview of the daily DNI values for the first half year of the simulation

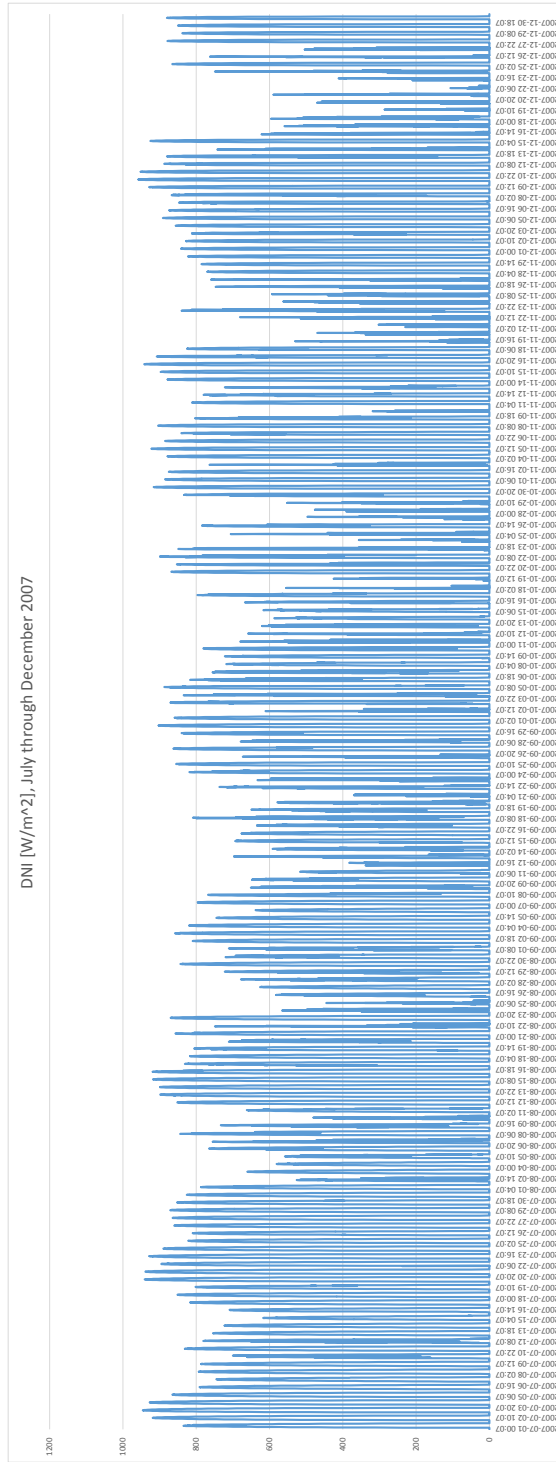


**Figure D.2:** An overview of the daily DNI values for the second half year of the simulation